

Development of Supramolecular Thermocell and Polysulfide Based Thermocell

梁, 益民

<https://doi.org/10.15017/2534411>

出版情報 : Kyushu University, 2019, 博士 (工学) , 課程博士
バージョン :
権利関係 :

Development of Supramolecular Thermocell and Polysulfide Based Thermocell

Yimin Liang

Department of Chemistry and Biochemistry

Graduate School of Engineering

KYUSHU UNIVERSITY

2019

Index

Chapter 1	General introduction	1
1.1.	Harvesting of waste heat and thermoelectric conversion	1
1.2.	Thermoelectric devices and thermocell.....	2
1.3.	Thermoelectric Properties of a thermocell	4
1.4.	Redox couples	7
1.5.	Electrolyte	9
1.6.	Electrodes.....	11
1.7.	Insertion of membrane	13
1.8.	Supramolecular thermocells.....	15
1.9.	Motivation and Outline	17
	Reference	19
Chapter 2	Hexakis(2,3,6-tri-O-methyl)- α -cyclodextrin- I_5^- Complex in Aqueous I^-/I_3^- Thermocells and Enhancement in the Seebeck Coefficient	21
2.1.	Introduction	21
2.2.	Results and discussion.....	24
2.3.	Conclusion.....	43
2.4.	Experimental	45
	Reference	52
Chapter 3	A theoretical basis for the enhancement of Seebeck Coefficients in Supramolecular Thermocells	55
3.1.	Introduction	55
3.2.	Results and Discussion.....	57
3.3.	Conclusion.....	65
3.4.	Experimental	66
	Reference	70
Chapter 4	Electrochemical Thermo-Electric Conversion Using Polysulfide as Redox Species	72
4.1.	Introduction	72
4.2.	Results and discussion.....	73
4.3.	Conclusion.....	82
4.4.	Experimental	82
	Reference	87
Chapter 5	Conclusion and future remark.....	89

Chapter 1 General introduction

1.1. Harvesting of waste heat and thermoelectric conversion

With the continuous increase of the global population and industrialization in developing countries, the demand for primary energy has reached unprecedented levels. Global primary energy demand is forecast to increase by 96 thousands barrels of oil equivalent per each day (mboe/d) between 2015 and 2040, rising from 276 mboe/d in 2015 to 372 mboe/d by 2040.¹ At the current consumption rate of primary energy, petroleum reserves will last about 40 more years, natural gas will last around 60 years, and coal will last approximately one and a half century.² The combustion of fossil fuels generates enormous amounts of atmospheric carbon dioxide, which results in the greenhouse effect and global warming. Among the consumed fossil energy, some studies estimated that about 20% to 50% of the industrial energy consumption is discharged as waste heat.^{3,4} Therefore, the conversion of thermal energy to useful energy is thus a feasible way to improve the efficiency of consumption of fossil fuel and reduce our dependence.

Based upon the temperature level, waste heat is usually classified as high-grade (above 1200 F / 649 °C), medium-grade (450 F / 232 °C to 1200 F / 649 °C) and low-grade (below 450 F / 232 °C).⁴ While high and medium-grade heat is easy to be recovered, low-grade heat dominates the most of waste heat(60%), and not practical or economical to recover with current technology.

Thermoelectric conversion is a kind of method to harvest waste heat, which can directly convert temperature difference to electric power. Thermoelectric conversion devices generate electric power without any moving parts such as fans and motors, and can work for a long period with maintenance-free, and pollution-free. Thus, the research on the conversion of thermal energy to electricity by Seebeck effect is very promising and always in ascendant. In addition to semiconductor-based thermoelectric devices, electrochemical reaction-based devices, called as thermocell, thermogalvanic cell or thermo-electrochemical cell, attracts much interest recently.

1.2. Thermoelectric devices and thermocell

Semiconductor-based thermoelectric devices have been studied as the main approach to transfer thermal energy to electricity. Electric potential emerges by the addition of temperature difference between both sides of the semiconductors. The induced potential (ΔV) is directly proportional to the temperature difference (ΔT). Thus the ratio is described as the Seebeck coefficient (S_e).^{5,6}

$$S_e = \frac{\Delta V}{\Delta T} \quad (\text{Equation 1-1})$$

Although the semiconductor-based thermoelectric devices already reach the practical level, the conventional S_e of the semiconductor-based materials is not high and remains in the range between 100 and 1000 $\mu\text{V/K}$. To obtain the working voltage, p- and n-type semiconductors are usually aligned in serial connection (Fig. 1-1).

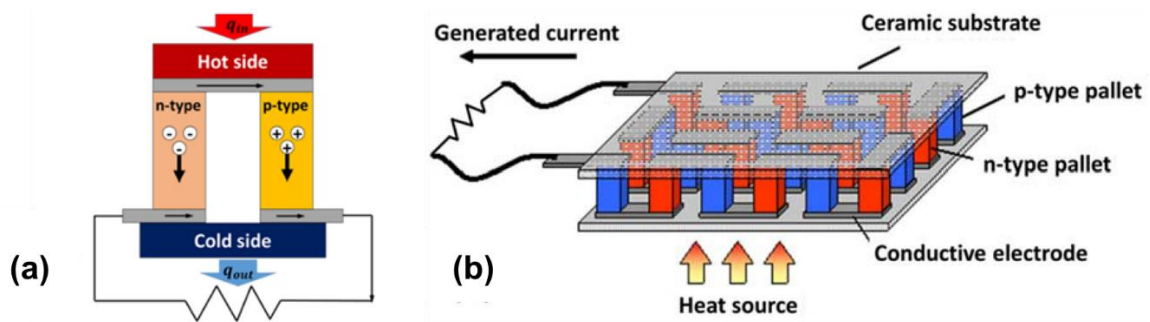


Figure 1-1. (a) A thermocouple consisting of a p-type and an n-type semiconductor, positive charge flow from the p-type to n-type leg in the external circuit resulting in electrical current. (b) Key components of a thermoelectric generator module.⁷

It is also difficult to overcome the interplay between electrical and thermal conductivity in these devices. Besides, the performance of those devices are usually limited in low-grade thermal energy recovery and containing very toxic elements.⁸ Therefore, thermocells attracts much interest recently as an alternative thermoelectric device.

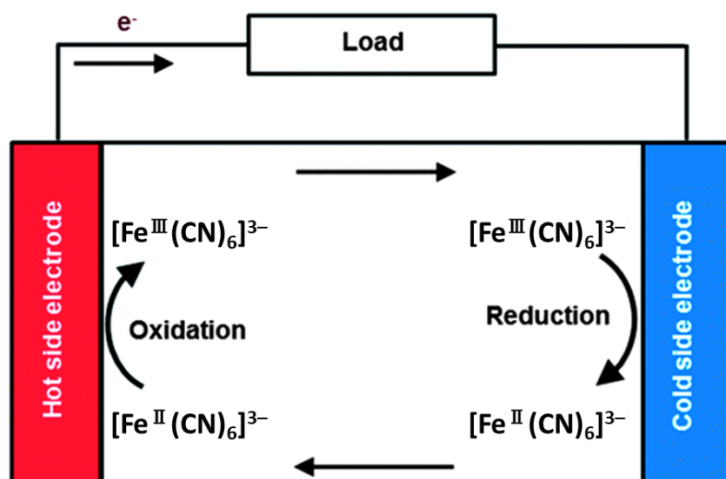


Figure 1-2. Schematic illustration of a thermos-electrochemical cell using the $[\text{Fe}^{\text{III}}(\text{CN})_6]^{3-}/[\text{Fe}^{\text{II}}(\text{CN})_6]^{3-}$ redox couple in aqueous electrolyte. The reduction reaction and oxidation reaction at the cold and hot side respectively generate the induced potential.⁹

A thermocell (also called thermogalvanic cell or thermo-electrochemical cell) is usually composed of redox couples and two electrodes immersed in an electrolyte (Fig. 1-2). The relatively low cost and high S_e (in the order of mV/K, which is higher than that of thermoelectric devices) of thermocells provides a potential solution for the low-grade thermal energy harvesting. However, due to the low carrier conductivity, the thermoelectric conversion efficiency of thermocells is still low, and much improvement has been required. This thesis provides detailed strategies for the enhancement of S_e in thermocells by taking advantage of supramolecular science.

As discussed below, the performance of thermocell is closely related to the thermodynamics of the redox species, and the detailed analysis of the thermoelectric performance could reveal the thermodynamic property of the redox species. In Chapter 4, I focused on the fabrication of sulfide thermocells, which could be the cheapest redox species, and executed the detailed analysis of redox species, which has not been clear.

1.3. Thermoelectric Properties of a thermocell

1.3.1. Seebeck Coefficient (S_e)

For a practical thermocell, a reasonable approximation of S_e is determined by the difference between the standard molar entropies of reactants and products.¹⁰ In the reduction-oxidation (redox) reaction in Eq. 1-2, the steady-state S_e is described as Eq. 1-3.



$$S_e = \frac{\partial E}{\partial T} = \frac{(S_B + S_B^*) - (S_A + S_A^*) - nS}{nF} \quad (\text{Equation 1-3})$$

where E is the steady-state potential difference, S_A and S_B are the partial molar entropies of species A and B, S_A^* and S_B^* are the respective Eastman entropies of the designated ions, S is the total transported entropy of the electrons in the electrodes, n is the number of electrons involved in the redox reaction above and F is the Faraday constant. The transported entropy is usually negligible, because it usually contributes only 1% of S_e .^{10,11} The contributions of S_A^* and S_B^* are also relatively small. Consequently, a simpler approximation of S_e can be derived by neglecting those three parameters. The sign of S_e is positive when the entropy is increasing in the reduction reaction, and *vice versa*. It is common to use the initial Seebeck coefficient S_e^0 , which can be simply expressed as Eq. 1-4.¹²

$$S_e^0 \cong \frac{S_B - S_A}{nF} \quad (\text{Equation 1-4})$$

1.3.2. Thermocell Performance

The power-generating ability of thermocells is evaluated by the current output of the loaded circuit. The current was obtained by simply placing a variable external load resistance (R_{ext}) in series with the cell and measuring the cell potential (E). Power output (P) was calculated by using the following equations in the basis of Ohm's law:

$$I = \frac{E}{R_{ext}} \quad (\text{Equation 1-6})$$

$$P = E \cdot I = \frac{E^2}{R_{ext}} \quad (\text{Equation 1-7})$$

The figure of merit (ZT) is dimension-less, which is quite commonly used to express the

performance of thermocells¹²

$$ZT = \frac{S_e^2 \sigma}{\kappa} T \quad (\text{Equation 1-8})$$

Where σ is the electrical conductivity, and κ is the thermal conductivity of the electrolyte. It should be noted that in the case of thermocell systems, σ is neither necessarily constant nor necessarily ohmic, and ZT is not suitable for evaluating the power conversion efficiency of a thermocell.¹⁰ Instead, the maximum power (P_{\max}) is simply given by the maximum rectangular area under the E-I curve and sometimes used for evaluating the performance of thermocells. Current density (j) was used as the X-axis, instead of the corresponding current (I). Usually, the E- j curve shows an approximately linear relationship, and the greatest area occurred at $E = 1/2 E_{oc}$, where the internal resistance (R_{int}) of the cell was equal to the external resistance, $R_{int} = R_{ext}$. Consequently, P_{\max} can be calculated as¹²

$$P_{max} = \left(\frac{E_{oc}}{2} \right) \left(\frac{I_{sc}}{2} \right) = \frac{E_{oc}^2}{4R_{int}} \quad (\text{Equation 1-9})$$

where I_{sc} is the short-circuit current delivered by the cell. P_{\max} can be determined from the maximum peak of the power output (P) plot, calculated using Eq. 6, even when the E-I characteristic curves are nonlinear.

The power conversion efficiency, η , of a thermocell is defined as Eq. 1-10.¹²

$$\eta = \frac{\text{electrical output power}}{\text{thermal power folowing through cell}} = \frac{P_{max}}{\left[KA \left(\frac{\partial T}{\partial x} \right) + \frac{IT\Delta S}{nF} \right]} \quad (\text{Equation 1-10})$$

The electrical power output is usually expressed as the maximum power output. The thermal power flowing through the cell generally consists of two parts: the first term is the rate of heat transfer due to simple thermal conduction, and which is dominating. A is the cross-sectional area of the thermocell, and $\partial T / \partial X$ is the temperature gradient between the cold and hot sides. The second term $IT\Delta S/nF$ is the transfer rate of the heat through the cell due to the reversible heat of the cell reaction. Quickenden et al. noted that the inclusion of this reversible heat of reaction is appropriate only in a cell that involves net consumption of electrolyte. Because there was no net consumption of electrolyte in the cell being tested, Eq. (9) can be simplified as Eq. 1-11.

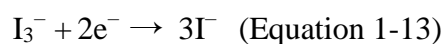
$$\eta = \frac{P_{max}}{KA\left(\frac{\partial T}{\partial x}\right)} \quad (\text{Equation 1-11})$$

Finally, η_r was defined as the power conversion efficiency relative to that of the Carnot cycle as Eq. 1-23, which provides a more comprehensive parameter to describe the efficiency of a power conversion device.

$$\eta_r = \frac{\eta}{1 - \frac{T_{cold}}{T_{hot}}} \quad (\text{Equation 1-12})$$

1.4. Redox couples

As discussed above, the thermoelectric potential of thermocells is determined by the entropy change during the redox equilibrium of redox couples. High stability and versatility are required for redox couples of thermocells. The aqueous electrolyte is widely used because of its versatility and high ionic conductivity of solute. $\text{Fe}(\text{CN})_6^{3-}/\text{Fe}(\text{CN})_6^{4-}$ shows a S_e of -1.4 mV/K, which depends slightly on concentration. Γ/I_3^- exhibits considerable concentration dependence than $\text{Fe}(\text{CN})_6^{3-}/\text{Fe}(\text{CN})_6^{4-}$. The S_e of Γ/I_3^- in ethylammonium nitrate ionic liquid changes in three-fold between concentration of 0.01 M and 2 M, and the maximum value of 0.97 mV/K is obtained when the concentration is 0.01 M.¹¹ The S_e of Γ/I_3^- in thermocell is positive due to the positive entropy change associated with the increase in the number of molecules upon reduction



However, Γ/I_3^- cause corrosion depending on the absolute redox potential. Recently, $\text{Co}^{2+/3+}$ or thiolate/disulfide redox couples in organic solvent have drawn attention in the development of as replacements for corrosive Γ/I_3^- redox couple in DSC.^{13,14} Pringle et al. investigated the $\text{Co}^{2+/3+}$ (bpy)₃ (NTf₂)^{2/3} redox couple (bpy = 2,2'-bipyridyl), NTf₂ = bis(trifluoromethanesulfonyl)amide and a maximum S_e of 2.19 mV K⁻¹ for an 0.01 M solution in 3-methoxypropionitrile iodide (MPN) was observed.¹⁵ Roger et al. reported thiolate/disulfide (McMT⁻/BMT) redox couple based thermocell, which gives a S_e of -0.6 mV/K.¹⁶

There were also some reports of thermocells that generated a potential *via* the redox reaction between redox reactive aqueous ion and solid electrodes, such as the Cu^+/Cu .^{17,18} In these cases the electrodes are solid copper, which is oxidized at the anode to Cu^{2+} . This is then transported through the electrolyte to be reduced at the cathode as Cu. As a result, a S_e of 0.84 mV/K (0.7 M CuSO_4) is observed. However, the gradual consumption of anode in such thermocells make it is impossible to generate energy continuously, which thus limits the practical application of such kinds of thermocells.

From the above, recent studies have mainly focused on the Cu, I, Fe and Co centered redox couples as well as thiolate/disulfide. Additionally, the use of acetone/isopropanol and $[\text{Cr}(\text{bpy})_3]^{3+/2+}$ were

attempted as well.^{19,20} On the other hand, the redox reaction of polysulfide species in the lithium-sulfur battery is attracting great interest,²¹⁻²⁴ but this kind of low-cost redox species never be tried in a thermocell. Thus, the feasibility of the using polysulfide as redox species in a thermocell will be described in Chapter 4.

1.5. Electrolyte

Most of the previous studies of thermocells use aqueous electrolytes, which generally gives higher power output due to the relatively fast ion diffusion. The highest power output of thermocells has been achieved with the aqueous $\text{Fe}(\text{CN})_6^{3-}/\text{Fe}(\text{CN})_6^{4-}$ electrolyte.^{25,26} Recently, Y. H. Kim et al. report the enhancement of S_e in the $\text{Fe}(\text{CN})_6^{3-}/\text{Fe}(\text{CN})_6^{4-}$ thermocell from -1.4 to -2.9 mV/K by adding organic solvent to the aqueous electrolyte (Fig. 1-3). The addition of organic solvent induced the rearrangement of solvated molecules surrounding $\text{Fe}(\text{CN})_6^{4-}$, which caused an increase in the entropy change of the overall redox system that yielded the high S_e .²⁷

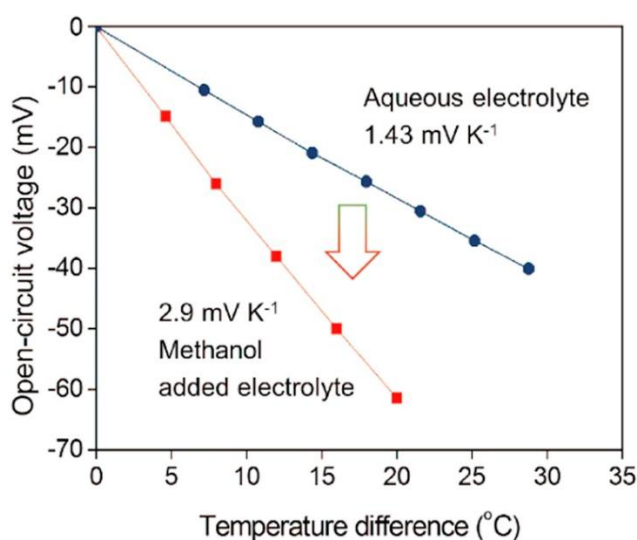


Figure 1-3. The S_e of the $\text{Fe}(\text{CN})_6^{3-}/\text{Fe}(\text{CN})_6^{4-}$ in aqueous electrolyte (blue scatters) and the mixed electrolyte of methanol and water.

J. Zhou et al. then significantly boost the S_e in aqueous $\text{Fe}(\text{CN})_6^{3-}/\text{Fe}(\text{CN})_6^{4-}$ electrolytes fabricated thermocell from -1.4 to -4.2 mV/K by the introduction of strong chaotropic cations (guanidinium) and highly soluble amide derivatives (urea) (Fig. 1-4). The mechanism of the enhancement of the S_e is that the significant increase in the entropy difference of the redox couple due to the synergistic interactions

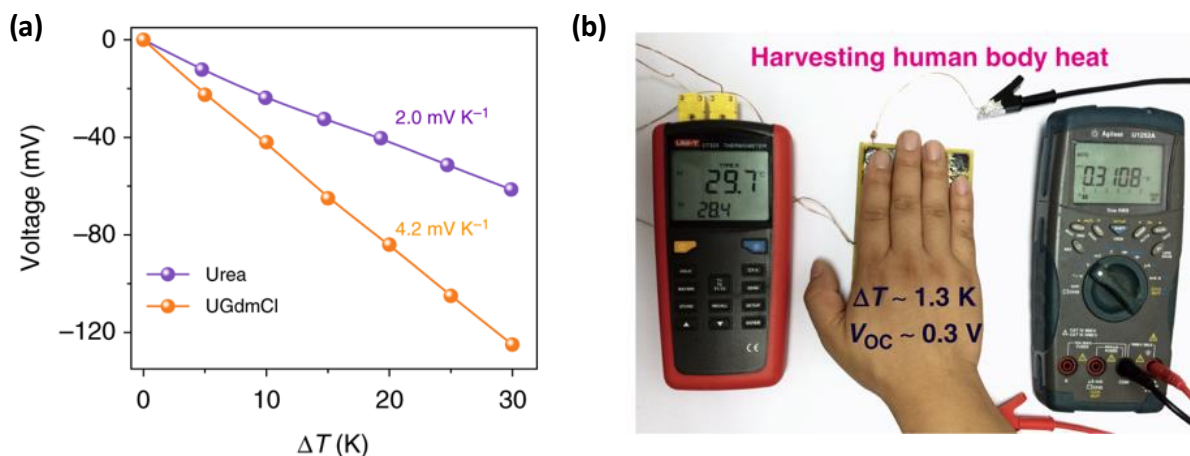


Figure 1-4. (a) The S_e of the $\text{Fe}(\text{CN})_6^{3-}/\text{Fe}(\text{CN})_6^{4-}$ electrolyte containing only urea or urea/GdmCl composite (UGdmCl). (b) Harvesting heat energy from the human body. When the module is closely touched by one hand. After several minutes, a stable temperature difference of 1.3 K is generated, which induced an approximately 0.3 V of open circuit potential.²⁸

between urea/guanidium and the redox couple. Guanidinium is prone to bond with $\text{Fe}(\text{CN})_6^{4-}$ rather than $\text{Fe}(\text{CN})_6^{3-}$ based on the ion specificity, whereas urea has a stronger affinity for $\text{Fe}(\text{CN})_6^{3-}$ than for $\text{Fe}(\text{CN})_6^{4-}$. These differences in affinity synergistically enlarge the entropy difference of the redox couple, thereby significantly increasing the S_e .²⁸

The boiling point of solvents limits the operating temperature, and water-based thermocell can work below 100 °C. Pringle et al. reported that the thermocells utilizing the $\text{Co}(\text{bpy})^{2+/3+}(\text{NTf}_2)_{2/3}$ redox couple in high boiling organic solvent MPN (methoxypropionitrile) or a series of ionic liquid show high S_e of 1.5 to 2.2 mV/K (Fig. 1-5).¹⁵ The outstanding thermal stability, negligible volatility and low thermal conductivity of ionic liquid make them ideal electrolytes for such higher-temperature energy harvesting.

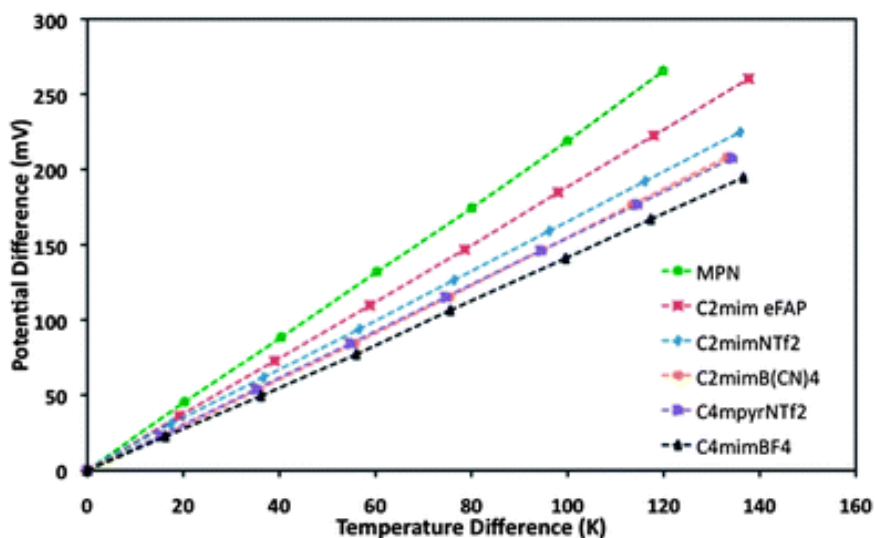


Figure 1-5. Se measurements of 0.01 M $\text{Co}^{2+/3+}$ $(\text{bpy})_3(\text{NTf}_2)_{2/3}$ in methoxypropionitrile (organic solvent) and ionic liquid.¹⁵

Additionally, the flexibility and leakage-prevention are crucial to thermocells, thus quasi-solid-state electrolytes have been prepared by the using of cellulose,²⁹ polyvinyl alcohol (PVA),³⁰ agar,³¹ or poly(sodium acrylate) beads.³¹

1.6. Electrodes

Platinum electrodes are widely used in various kinds of thermocells, due to its high electrochemical catalytic activity that minimizes the charge transfer overpotential. However, the high cost prohibits the commercialization, and cheaper materials is imperative. Recently, carbon electrodes are gaining much attention as a promising, low-cost alternative to platinum. Nano-structured carbon materials, such as nanotubes and graphene, have a high surface area which increases the number of reaction sites. They can also increase the current density in the thermocells.^{32,33}

In the first report that utilized carbon nanotubes as electrode materials,³⁴ electrodes consisting of multi-walled carbon (MWCNT) buckypaper and vertically aligned MWCNTs were fabricated (Fig. 1-6). These electrodes provide high electrochemical surface areas and fast redox-mediated electron transfer, which greatly enhances thermocell current capacity and overall efficiency. Thermocell

efficiency then is further improved by directly synthesizing MWNTs as vertical forests that reduce the electrical and thermal resistance at electrode/substrate junctions. As a result, the efficiency of thermocells with MWNT electrodes is as high as 1.4 % of Carnot efficiency, which is three-fold higher than those of previously reported thermocells .

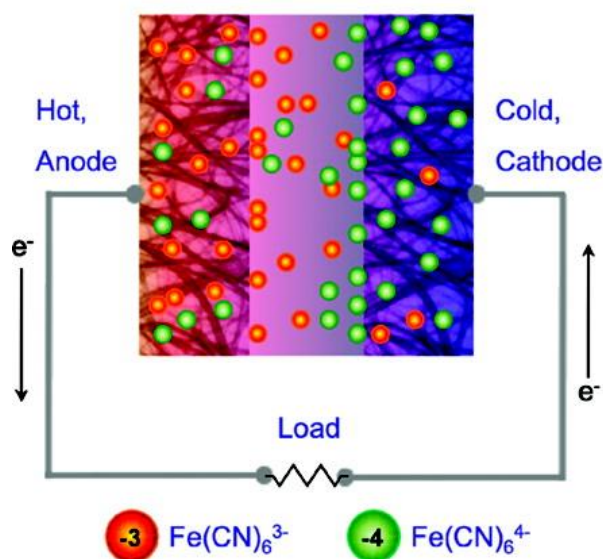


Figure 1-6. Scheme of a thermocell with carbon nanostructured electrodes showing concentration gradients of the ferri–ferrocyanide redox ions during power generation.³⁴

The highest thermoelectric conversion efficiency of thermocell was achieved by the use of a carbon-nanotube aerogel-based electrode in aqueous $\text{Fe(CN)}_6^{3-}/\text{Fe(CN)}_6^{4-}$ electrolyte, with a conversion efficiency of 3.95% (Fig. 1-7).²⁶ This study exploited planar and cylindrical wound carbon nanotube (CNT) aerogel sheets as the thermocell electrodes around a tungsten wire, which acts as the current collector, the high power performance was attributed to fast ion diffusion to the electrode surface, arising from the wound nanotubes with aligned pores and low tortuosity, combined with the high surface area, and high catalytic activity contributed to by the Pt nanoparticles. Although these kinds of electrodes using less platinum than pure platinum electrodes, the relatively complicated fabrication is unpleasant for commercialization

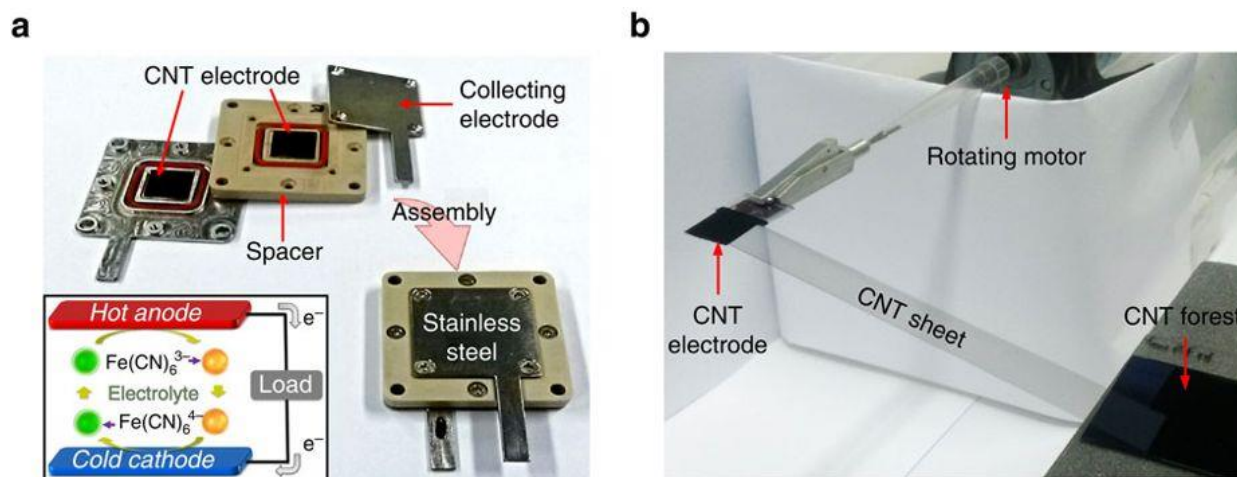


Figure 1-7. A schematic figure of cell components and their assembly into a planar thermocell. (b) An apparatus for continuously drawing a carbon nanotube (CNT) aerogel sheet from a CNT forest, and wrapping it around a metal frame to form an electrode for a planar thermocell.²⁶

1.7. Insertion of membrane

Conduction and convection of heat are one of the crucial issues for the inefficiency of thermoelectric conversion, and the insertion of a membrane is thus an effective way to increase the temperature gradient between cold and hot sides. The first attempt was

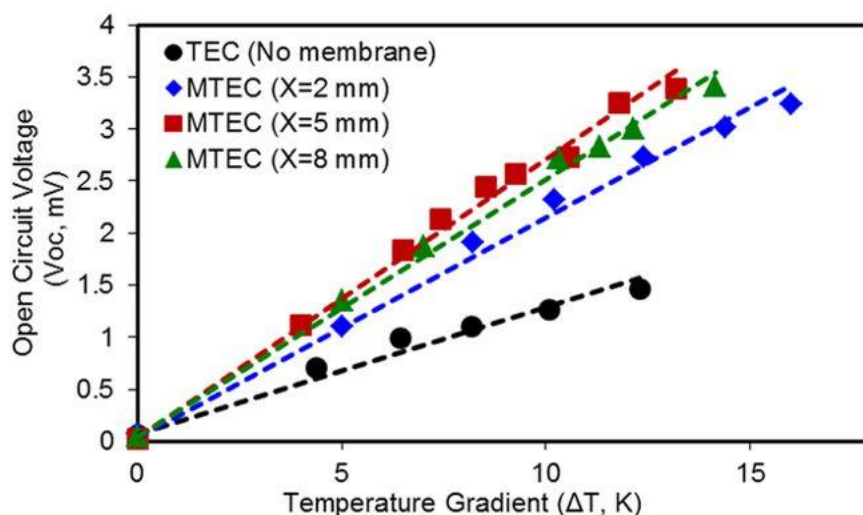


Figure 1-8. The linear change of open circuit potential with the change of external temperature difference. The color represents the various distance between the membrane and cold electrode. The distance of 5 mm gives the best performance.³⁵

the insertion of Poly(Vinylidene Fluoride) (PVDF) membrane into thermocells to hinder the heat conductivity (Fig. 1-8).³⁵ At a temperature difference (external source) of 12 K, an enhancement in the open circuit voltage (V_{oc}) from 1.3 to 2.8 mV is observed. Meanwhile, the study revealed that the distance between the membrane and electrode has an influence to the internal temperature difference.

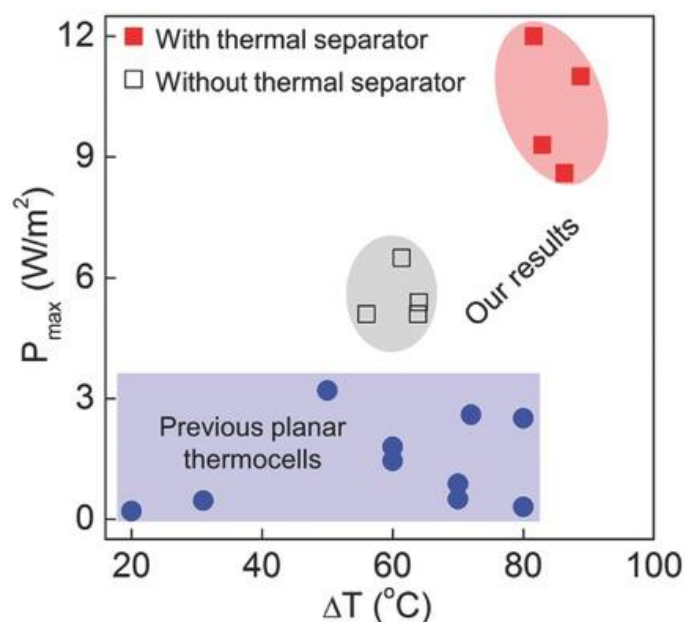


Figure 1-9. The comparison of power densities for different ΔT in previous studies (without separator) and present study (with separator).³⁶

Another recent study introduced a separator into a $Fe(CN)_6^{3-}/Fe(CN)_6^{4-}$ based thermocell with activated carbon electrodes (Fig. 1-9).³⁶ Not only the separator position but also the thickness and composition were discussed. The record-breaking power output of $11 W m^{-2}$ ($1.5 mW m^{-2} K^{-2}$, $\Delta T = 86 K$) was obtained by the using a cotton membrane with less than 8% thickness of the inter-electrode spacing (0.2 mm in a 2.6 mm cell) located to the cold electrode. The result is significant compared with the thermocell without any membrane ($5.4 W m^{-2}$; $1.3 mW m^{-2} K^{-2}$, $\Delta T = 64 K$) or the thermocell consist of a cellulose sponge separator ($10.6 W m^{-2}$, $1.4 mW m^{-2} K^{-2}$, $\Delta T = 86 K$).

1.8. Supramolecular thermocells

Along with the innovation of redox species, electrolyte, and electrode in the performance improvement, our group demonstrated a fascinating way by the host-guest interaction to enhance the S_e in thermocell (Fig. 1-10).³⁷ Since the association and dissociation of α -CD and I_3^- is exothermic and endothermic reactions,

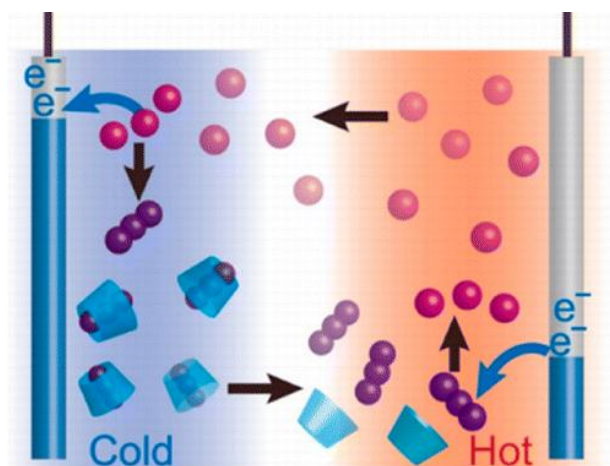


Figure 1-10. A schematic illustration of supramolecular thermocell in the combination of α -CD and I^-/I_3^- .

respectively, the I_3^- at the cold side is captured by α -CD, which shifts the redox equilibrium to oxidizing of more I^- to I_3^- . Meanwhile, the dissociation of α -CD- I_3^- complex promotes the reduction of I_3^- at the hot side. Based on Nernst equation³⁸

$$S_e = \frac{\Delta E_f}{\Delta T} + \frac{R}{2F\Delta T} \left(T_H \ln \frac{[I_3^-]_H}{[I^-]_0^3} - T_C \ln \frac{[I_3^-]_C}{[I^-]_0^3} \right)$$

where the subscripts “H”, “C” and zero represent the corresponding variables for hot and cold sides of cells in equilibrium, and an initial state, respectively, and ΔE_f is the difference of formal potential, which relates to activity coefficients of redox species.

The shift of equilibrium of the redox species by encapsulation enhances the S_e from 0.86 to 1.43 mV/K. Furthermore, water-soluble starch and polyvinylpyrrolidone (PVP), was demonstrated as polymeric hosts to selectively encapsulated I_3^- in I^-/I_3^- composed thermocell, the significant enhancement of S_e to 1.5 mV/K by starch is observed (Fig. 1-11).³⁹ The use of inexpensive polymers

in this work to pave the way to improve the S_e by using polymers as host materials for redox species,

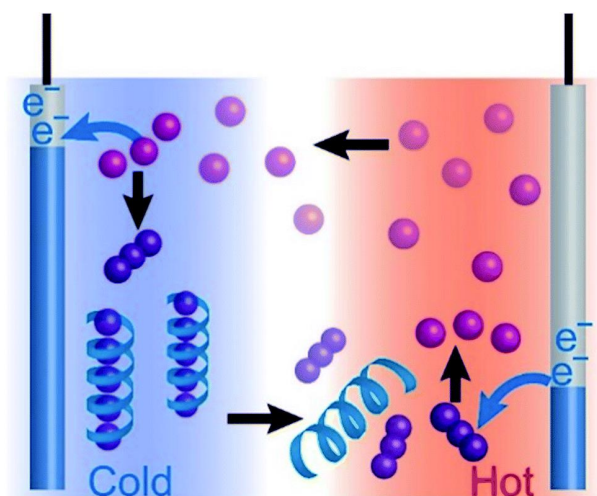


Figure 1-11. Schematic of a thermocell consists of a polymer as host, which binds triiodide (I_3^- , purple sphere) at the cold side and releases it at the hot side.

which also indicates the possibility of using host-guest inclusion to further increase the S_e .

In addition to the I^-/I_3^- based supramolecular thermocells, S_e enhancement in the thermocell consists of ferrocenecarboxylate/ferroceniumcarboxylate also realized by the association of ferrocenecarboxylate and β -cyclodextrin.⁴⁰ This study gives the first example of the fabrication of p-type (negative S_e) supramolecular thermocell. However, the S_e in thermocells consist of α -CD (1.43 mV/K), polymers (1.5 mV/K) or β -CD (-1.20 mV/K) are still low value, and further enhancement of S_e is imperative.

1.9. Motivation and Outline

The thermoelectric conversion efficiency of thermocells is still lower than that of semiconductor devices; however, the performance of thermocells is quickly improved in these five years. Thus, the further improvement of the performance of thermocells could achieve the real application of thermocells. The main focus of this thesis is to fabricate high performance or low-cost thermocells on the basis of host-guest supramolecular science or polysulfide redox species respectively. This thesis consists of five chapters. The outline of chapter 2 and later are described below.

Chapter 2 describes the further enhancement of the Seebeck coefficient from 0.8 to 1.9 mV K⁻¹ by the using of Hexakis(2,3,6-tri-*O*-methyl)- α -cyclodextrin (Me₁₈- α -CD), which is a derivative of α -cyclodextrin (α -CD). The previous work in our group demonstrated that α -CD enhances the Seebeck coefficient from 0.8 to 1.4 mV/K. Isothermal titration calorimetry (ITC) measurement and fitting analysis suggest that the binding constant of Me₁₈- α -CD and I₃⁻ is much higher than that of α -CD and I₃⁻, which further enlarges the concentration difference of I₃⁻ and gives the larger Seebeck coefficient. Furthermore, the encapsulation of I₅⁻ in Me₁₈- α -CD is observed. Generally, I₅⁻ only exists in coordination compounds, the formation of I₅⁻ thus is observed in the solution for the first time, which gives a way to study the property of I₅⁻ in solution.

Chapter 3. describes a theoretical basis of the enhancement of the Seebeck coefficient in thermocells. In this study, the Seebeck coefficient change for the addition of four kinds of cyclodextrins (Me₁₂- α -CD, α -CD, β -CD and γ -CD) were investigated. The theoretical analysis revealed that association enthalpy between the hosts and triiodide has a major influence on the Seebeck coefficients of the thermocells. Thermodynamic parameters of host-guest associations were evaluated by isothermal titration calorimetry, which is in good agreement with the theoretically estimated values from thermocell measurements. This result provides a guideline to estimate the Seebeck coefficient of supramolecular thermocells and to determine the thermodynamic parameters.

Chapter 4 describes a new demonstration of low-cost thermocell consists of polysulfide redox species. In this method, 1-Butyl-1-methylpyrrolidinium polysulfide (P₁₄S₃) is synthesized and the

redox species are prepared by the addition of sulfur to the $P_{14}S_3$ solution in DMSO. In thermoelectric measurement, the sign of the Seebeck coefficient changes from -0.68 to $+0.5$ mV/K by the addition of elemental sulfur in the cell. Operando UV-vis spectroscopy, as well as open circuit voltage analysis, revealed that the change in the sign is attributed to the change in the dominating redox reactions by the addition of sulfur. This result also provides a thermodynamic aspect of polysulfides electrochemistry, which is of high importance in lithium–sulfur battery.

Chapter 5. gives a summary of the whole thesis work

Reference

- 1 Organization of the Petroleum Exporting Countries, World Oil Outlook 2040, 2018. Available online: https://www.opec.org/opec_web/en/publications/340.htm (accessed on 12 June 2019).
- 2 BP Statistical Review of World Energy, 2018. Available online: <https://www.bp.com/en/global/corporate/energy-economics/statistical-review-of-world-energy.html> (accessed on 13 June 2019)
- 3 I. Johnson, W.T. Choate, A. Davidson, *Waste Heat Recovery*. Technology and Opportunities in Us Industry, BCS, Inc.: Laurel, MD, USA, 2008.
- 4 Heat is Power. Available online: <https://www.heatispower.org> (accessed on 12 June 2019)
- 5 H.J. Goldsmid, Introduction to Thermoelectricity; Springer: Berlin, Germany, 2010; Volume 121.
- 6 C. T. Hsu, G. Y. Huang, H. S. Chu, B. Yu and D. J. Yao, *Appl. Energy*, 2011, **88**, 5173–5179.
- 7 Key Components of a Thermoelectric Generator (TEG) Module. Available online: <https://www.Digikey.Co.Nz/en/articles/techzone/2014/apr/thermoelectric-energy-generation-takes-flight-for-aircraft-and-spacecraft-monitoring> (accessed on 12 June 2019).
- 8 G. J. Snyder and E. S. Toberer, *Nat. Mater.*, 2008, **7**, 105.
- 9 D. R. MacFarlane, N. Tachikawa, M. Forsyth, J. M. Pringle, P. C. Howlett, G. D. Elliott, J. H. Davis, M. Watanabe, P. Simon and C. a Angell, *Energy Environ. Sci.*, 2014, **7**, 232–250.
- 10 T. I. Quickenden and C. F. Vernon, *Sol. Energy*, 1986, **36**, 63–72.
- 11 a J. deBethune, T. S. Licht and N. Swendeman, *J. Electrochem. Soc.*, 1959, **106**, 616–625.
- 12 T. I. Quickenden; Y. Mua, *J. Electrochem. Soc.*, 1995, **142**, 3985.
- 13 Z. Ning, H. Tian, C. Yuan, Y. Fu, L. Sun and H. Ågren, *Chem. Eur. J.*, 2011, **17**, 6330–6333.
- 14 H. N. Tsao, C. Yi, T. Moehl, J. H. Yum, S. M. Zakeeruddin, M. K. Nazeeruddin and M. Grätzel, *ChemSusChem*, 2011, **4**, 591–594.
- 15 T. J. Abraham, D. R. MacFarlane and J. M. Pringle, *Energy Environ. Sci.*, 2013, **6**, 2639–2645.
- 16 V. Zinovyeva, S. Nakamae, M. Bonetti and M. Roger, *ChemElectroChem*, 2014, **1**, 426–430.
- 17 A. Gunawan, C. H. Lin, D. A. Buttry, V. Mujica, R. A. Taylor, R. S. Prasher and P. E. Phelan, *Nanoscale Microscale Thermophys. Eng.*, 2013, **17**, 304–323.
- 18 A. Gunawan, H. Li, C. H. Lin, D. A. Buttry, V. Mujica, R. A. Taylor, R. S. Prasher and P. E. Phelan, *Int. J. Heat Mass Transf.*, 2014, **78**, 423–434.
- 19 T. Migita, N. Tachikawa, Y. Katayama, T. Miura, *Electrochemistry* 2009, **77**, 639-641.
- 20 H. Zhou and P. Liu, *ACS Appl. Energy Mater.*, 2018, **1**, 1424–1428.
- 21 A. Manthiram, Y. Fu and Y. S. Su, *Acc. Chem. Res.*, 2013, **46**, 1125–1134.
- 22 M. Wild, L. O’Neill, T. Zhang, R. Purkayastha, G. Minton, M. Marinescu and G. J. Offer, *Energy Environ. Sci.*, 2015, **8**, 3477–3494.
- 23 Y. X. Yin, S. Xin, Y. G. Guo and L. J. Wan, *Angew. Chemie - Int. Ed.*, 2013, **52**, 13186–13200.
- 24 S. S. Zhang, *J. Power Sources*, 2013, **231**, 153–162.
- 25 R. Hu, B. A. Cola, N. Haram, J. N. Barisci, S. Lee, S. Stoughton, G. Wallace, C. Too, M. Thomas, A. Gestos, M. E. Dela Cruz, J. P. Ferraris, A. A. Zakhidov and R. H. Baughman, *Nano Lett.*, 2010, **10**,

838–846.

- 26 H. Im, T. Kim, H. Song, J. Choi, J. S. Park, R. Ovalle-Robles, H. D. Yang, K. D. Kihm, R. H. Baughman, H. H. Lee, T. J. Kang and Y. H. Kim, *Nat. Commun.*, 2016, **7**, 10600.
- 27 T. Kim, J. S. Lee, G. Lee, H. Yoon, J. Yoon, T. J. Kang and Y. H. Kim, *Nano Energy*, 2017, **31**, 160–167.
- 28 J. Duan, G. Feng, B. Yu, J. Li, M. Chen, P. Yang, J. Feng, K. Liu and J. Zhou, *Nat. Commun.*, 2018, **9**, 1–8.
- 29 L. Jin, G. W. Greene, D. R. MacFarlane and J. M. Pringle, *ACS Energy Lett.*, 2016, **1**, 654–658.
- 30 P. Yang, K. Liu, Q. Chen, X. Mo, Y. Zhou, S. Li, G. Feng and J. Zhou, *Angew. Chemie - Int. Ed.*, 2016, **55**, 12050–12053.
- 31 J. Wu, J. J. Black and L. Aldous, *Electrochim. Acta*, 2017, **225**, 482–492.
- 32 J. M. Nugent, K. S. V Santhanam, A. Rubio and P. M. Ajayan, *Nano Lett.*, 2001, **1**, 87–91.
- 33 L. Tang, Y. Wang, Y. Li, H. Feng, J. Lu and J. Li, *Adv. Funct. Mater.*, 2009, **19**, 2782–2789.
- 34 R. Hu, B. A. Cola, N. Haram, J. N. Barisci, S. Lee, S. Stoughton, G. Wallace, C. Too, M. Thomas, A. Gestos, M. E. Dela Cruz, J. P. Ferraris, A. A. Zakhidov and R. H. Baughman, *Nano Lett.*, 2010, **10**, 838–846.
- 35 S. W. Hasan, S. M. Said, M. F. M. Sabri, A. S. A. Bakar, N. A. Hashim, M. M. I. M. Hasnan, J. M. Pringle and D. R. MacFarlane, *Sci. Rep.*, 2016, **6**, 1–11.
- 36 L. Zhang, T. Kim, N. Li, T. J. Kang, J. Chen, J. M. Pringle, M. Zhang, A. H. Kazim, S. Fang, C. Haines, D. Al-Masri, B. A. Cola, J. M. Razal, J. Di, S. Beirne, D. R. MacFarlane, A. Gonzalez-Martin, S. Mathew, Y. H. Kim, G. Wallace and R. H. Baughman, *Adv. Mater.*, 2017, **29**, 1–7.
- 37 H. Zhou, T. Yamada and N. Kimizuka, *J. Am. Chem. Soc.*, 2016, **138**, 10502–10507.
- 38 D. A. Aikens, *Electrochemical methods, fundamentals and applications*, 2009, vol. 60.
- 39 H. Zhou, T. Yamada and N. Kimizuka, *Sustain. Energy Fuels*, 2018, **2**, 472–478.
- 40 T. Yamada, X. Zou, Y. Liang and N. Kimizuka, *Polym. J.*, 2018, **50**, 771–774.

Chapter 2

Hexakis(2,3,6-tri-*O*-methyl)- α -cyclodextrin- I_5^- Complex in Aqueous I^-/I_3^- Thermocells and Enhancement in the Seebeck Coefficient

Abstract: A large Seebeck coefficient (S_e) of 1.9 mV K⁻¹ is recorded for the I^-/I_3^- thermocell by harnessing host-guest complexation of hexakis(2,3,6-tri-*O*-methyl)- α -cyclodextrin (Me₁₈- α -CD) with the oxidized iodide species. The thermocell measurement and UV-vis spectroscopy unveiled the formation of a Me₁₈- α -CD-pentaiodide (I_5^-) complex, which is in remarkable contrast to the triiodide complex α -CD- I_3^- previously reported. Although precipitation of α -CD- I_3^- complex in the presence of an electrolyte such as potassium chloride has been a problem for their application to thermocells, this issue has solved by using Me₁₈- α -CD as a host compound. The absence of precipitation in the Me₁₈- α -CD and I^-/I_3^- system containing potassium chloride not only improves S_e of the I^-/I_3^- thermocell but also significantly enhances the temporal stability of the power output. This is the first observation that I_5^- species are formed in an aqueous solution which has been utilized in thermocells. The solution equilibrium of redox couples is controllable by tuning the chemical structure of host compounds. The integration of host-guest chemistry with redox couples thus pushes the limit of thermocells.

2.1. Introduction

Thermo-electric conversion based on Seebeck effect has been attracting much interest because of its potential to retrieve the waste heat and converting it to electricity, which provides a promising way to reduce the consumption of fossil fuel. The semiconductor-based device has been shared a major position of the thermo-electric materials for many years. However, their

small S_e limited the improvement of their development.¹⁻⁵ Thermocells, often referred to as thermo-electrochemical cells or thermo-galvanic cells, offer an alternative approach to design a thermo-electric device which attracted growing attention due to their relatively high S_e and low cost.⁶⁻⁸

Thermocells composed of a redox pair that is dissolved into the electrolyte. As reviewed by Quikenden, Pringle and their coworkers, various strategies were devoted to improving the performance of thermocells, and S_e reached up to 1.4 mV K^{-1} by using Pt electrodes and an aqueous solution of $[\text{Fe}(\text{CN})_6]^{3-/4-}$.⁹⁻¹¹ Recently, carbon nanotube was utilized as the electrodes and the conversion efficiency of thermocell was enhanced to 3.95% relative to the Carnot cycle.¹²⁻¹⁴ Ionic liquid based thermocells have also been extensively studied, which marked a high S_e of 2.2 mV K^{-1} in the wide temperature range.¹⁵⁻¹⁷ However, a strategy to improve the figure-of-merit value is still required for the practical usage of thermocells

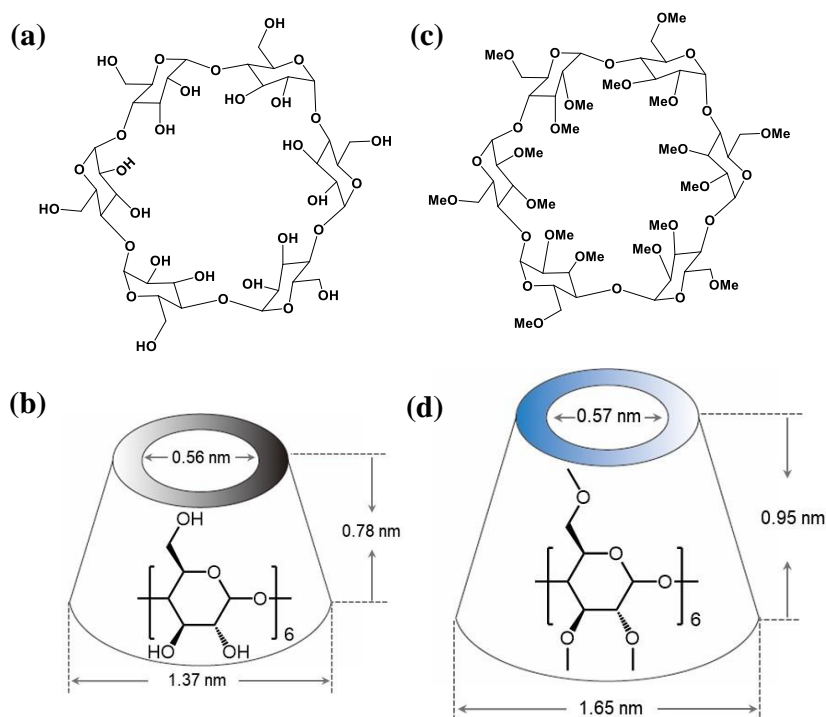


Figure 2-1. (a, b) The molecular structure and size of α -Cyclodextrin (α -CD)¹⁸ and (c, d) hexakis(2,3,6-tri-*O*-methyl)- α -Cyclodextrin (Me_{18} - α -CD)¹⁹, respectively.

We recently reported the concept of supramolecular thermocell, which was demonstrated by introducing α -Cyclodextrin (α -CD, Fig. 2-1a) as a molecular host to the I^-/I_3^- thermocell. α -CD selectively captured hydrophobic I_3^- anion, which led to a significant enhancement of S_e from 0.8 to 1.4 mV K⁻¹.²⁰ The addition of KCl, supporting electrolyte, caused precipitation of the α -CD- I_3^- complex in the lower-temperature cells, which further increased the S_e value to ca. 2 mV K⁻¹. Polymers such as starch and poly (vinyl pyrrolidone) also served as host matrices, which showed an increase of S_e to 1.5 and 1.2 mV K⁻¹, respectively.²¹ This host-guest approach is applicable to various kinds of redox species and the effect independent from the type of electrodes. It turned out to be useful in improving the S_e value in thermocells, and the highest S_e of ca. 2 mV K⁻¹ has been achieved for the precipitation-dissolution equilibrium system of α -CD- I_3^- in aqueous KCl.

Although the addition of KCl was desirable to increase the conductivity of the electrochemical thermocell, the precipitation observed for the α -CD- I_3^- system decreased the diffusion ratio of the redox species and also impaired the durability of the thermocell. To solve this issue, it is essential to develop host molecules that show the enhanced stability of the inclusion complex in aqueous electrolytes. We herein report that hexakis(2,3,6-tri-*O*-methyl)- α -Cyclodextrin (Me₁₈- α -CD, Fig. 2-1c) as a suitable host molecule for the I^-/I_3^- thermocell. The aqueous solution of Me₁₈- α -CD and iodide showed high stability and no precipitation was observed even in the presence of supporting electrolytes. The S_e of thermocell reached 1.92 mV K⁻¹ which is the highest value reported to date for the homogeneous I^-/I_3^- thermocells.

In addition, we found the system show an unusual off-stoichiometric interaction between Me₁₈- α -CD and I_3^- , and the formation of Me₁₈- α -CD-pentaiodide (I_5^-) complex is demonstrated for the first time. It is to note that the formation of I_5^- species in aqueous solution has never been confirmed, which presence has been only reported for the solid crystals²²⁻²⁵. This result shows the design of proper host molecules lead to superior thermoelectric conversion (Fig. 2-2).

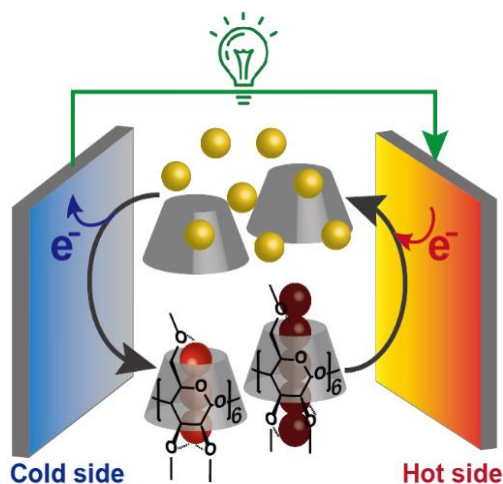


Figure 2-2. Schematic illustration of supramolecular thermocell composed by I^- (yellow balls), I_3^- (a trio of red balls), I_5^- (connecting five dark red balls) and $\text{Me}_{18}\text{-}\alpha\text{-CD}$ (gray cone-shaped cylinder).

2.2. Results and discussion

2.2.1. Thermocell measurement

In order to investigate the effect of host–guest interaction, I^-/I_3^- thermocells were prepared under various concentrations of $\text{Me}_{18}\text{-}\alpha\text{-CD}$. The concentrations of redox couple was kept same as the previous work ($[\text{KI}] = 10 \text{ mM}$, $[\text{I}_3^-] = 2.5 \text{ mM}$).²⁰ In contrast to the previous $\alpha\text{-CD-I}^-/\text{I}_3^-$ system, the present $\text{Me}_{18}\text{-}\alpha\text{-CD}$ did not cause precipitation even in the presence of KCl . The detail of the experimental procedure is described in the experimental part. The open circuit voltage (V_{oc}) of the cell between the hot and cold electrodes corresponds to the generating voltage of the cell. The temperature dependence of V_{oc} at varied concentrations of hosts is shown in Fig. 2-3a. V_{oc} values were proportional to the temperature difference (ΔT), where the slope of lines corresponds to the Seebeck coefficients. That is, a high S_e value means the large voltage emergence with the same temperature difference. In Fig. 2-3b, the obtained S_e was plotted as the function of $\text{Me}_{18}\text{-}\alpha\text{-CD}$ and $\alpha\text{-CD}$ concentrations, respectively. The data for the $\alpha\text{-CD-I}^-/\text{I}_3^-$ system was also shown for comparison. The S_e value obtained without hosts is 0.84 mV K^{-1} , which confirms the reproducibility of the previous work (0.86 mV K^{-1}).²⁰ In the case of $\text{Me}_{18}\text{-}\alpha\text{-CD-I}^-/\text{I}_3^-$ system, S_e value was almost constant below the $\text{Me}_{18}\text{-}\alpha\text{-CD}$ concentration of

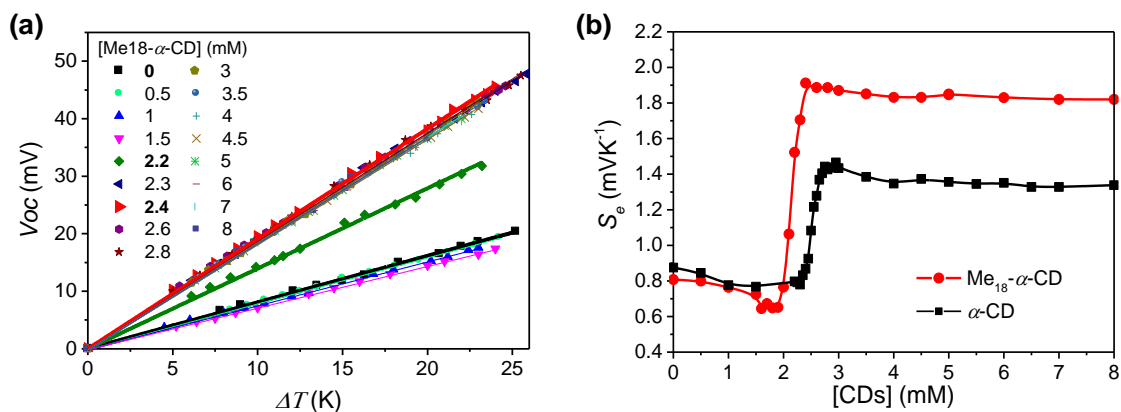


Figure 2-3. (a) The plots of V_{oc} and ΔT with various Me₁₈- α -CD concentration. $[KI]_0 = 12.5$ mM and $[I_2]_0 = 2.5$ mM. (b) Seebeck coefficient estimated from the slope of Fig. 2 (a) with various concentration of Me₁₈- α -CD (red circles) and α -CD (black squares) thermocells. The margin of error for each point is less than 0.02 mV K⁻¹.

1.5 mM, while a drastic increase was observed above the concentration of 2.0 mM. The high S_e value was maintained above the concentration of ca. 2.4 mM. The maximum S_e of 1.92 mV K⁻¹ was observed at the concentration of 2.2 mM, which is 1.08 mV K⁻¹ higher than that without host molecule. This value is also ca. 0.5 mV K⁻¹ higher than that obtained from the pristine α -CD- I^-/I_3^- cell system in the absence of KCl, and provides the highest value of the homogeneous I^-/I_3^- thermocells. Although we have reported a slightly higher S_e value of 1.97 mV K⁻¹ for the inhomogeneous precipitate–dissolution equilibrium mixtures caused by the addition of KCl into the α -CD- I^-/I_3^- thermocell, the presence of such precipitates significantly decreased its durability.²⁰

We note that an inflection point was observed for the curve at $[Me_{18}\text{-}\alpha\text{-CD}] = \text{ca. } 2.1$ mM, which is well below that observed for α -CD (ca. 2.5 mM). In the case of α -CD, it stoichiometrically captures I_3^- and thus the concentration of the inflection point was almost the same as the initial concentration of I_3^- . The observed shift of the inflection point for Me₁₈- α -CD reflects the formation of complexes with different stoichiometry. As discussed below, the observed shift is derived from the complexation of Me₁₈- α -CD with I_5^- species.

2.2.2. Isothermal titration calorimetry

The stoichiometry of Me₁₈- α -CD and polyiodide anion was investigated by isothermal titration calorimetry (ITC) (Fig. 2-4). In the case of pristine α -CD, the inflection point of the ITC curve

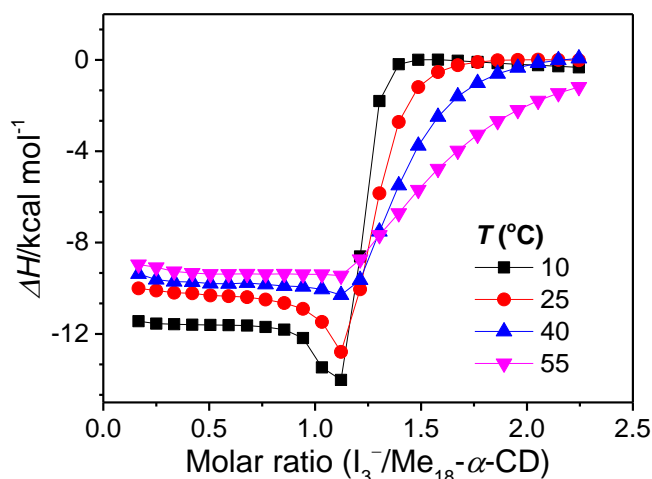
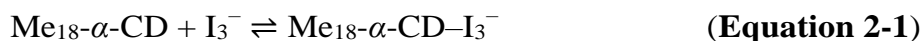


Figure 2-4. ITC curves of the aqueous solutions of I₃⁻ to Me₁₈- α -CD at various temperature.

for α -CD with I₃⁻ was observed at ca. 1:1, which reflects the 1:1 complexation between I₃⁻ and α -CD.^{20,26-28} In contrast, the inflection point of the ITC curve for Me₁₈- α -CD with I₃⁻ is ca. 1.2:1 at 10 °C, which further shifted to 1.3:1 with increasing temperature. This result shows that the interaction of two I₃⁻ molecules with one Me₁₈- α -CD is involved. The most probable reaction is the encapsulation of I₅⁻ ion according to the following equations. The formation of I₅⁻ ion in aqueous Me₁₈- α -CD is supported by the UV-Vis and Raman spectral measurements described later.



Since Eq. 2-2 is an equilibrium reaction, the encapsulation reaction occurs at a high concentration of I₃⁻. ITC curves in Fig. 2-4a has a hump of ΔH at the molar ratio between 0.8 to 1.1 eq., which could be attributed to the encapsulation of I₅⁻.

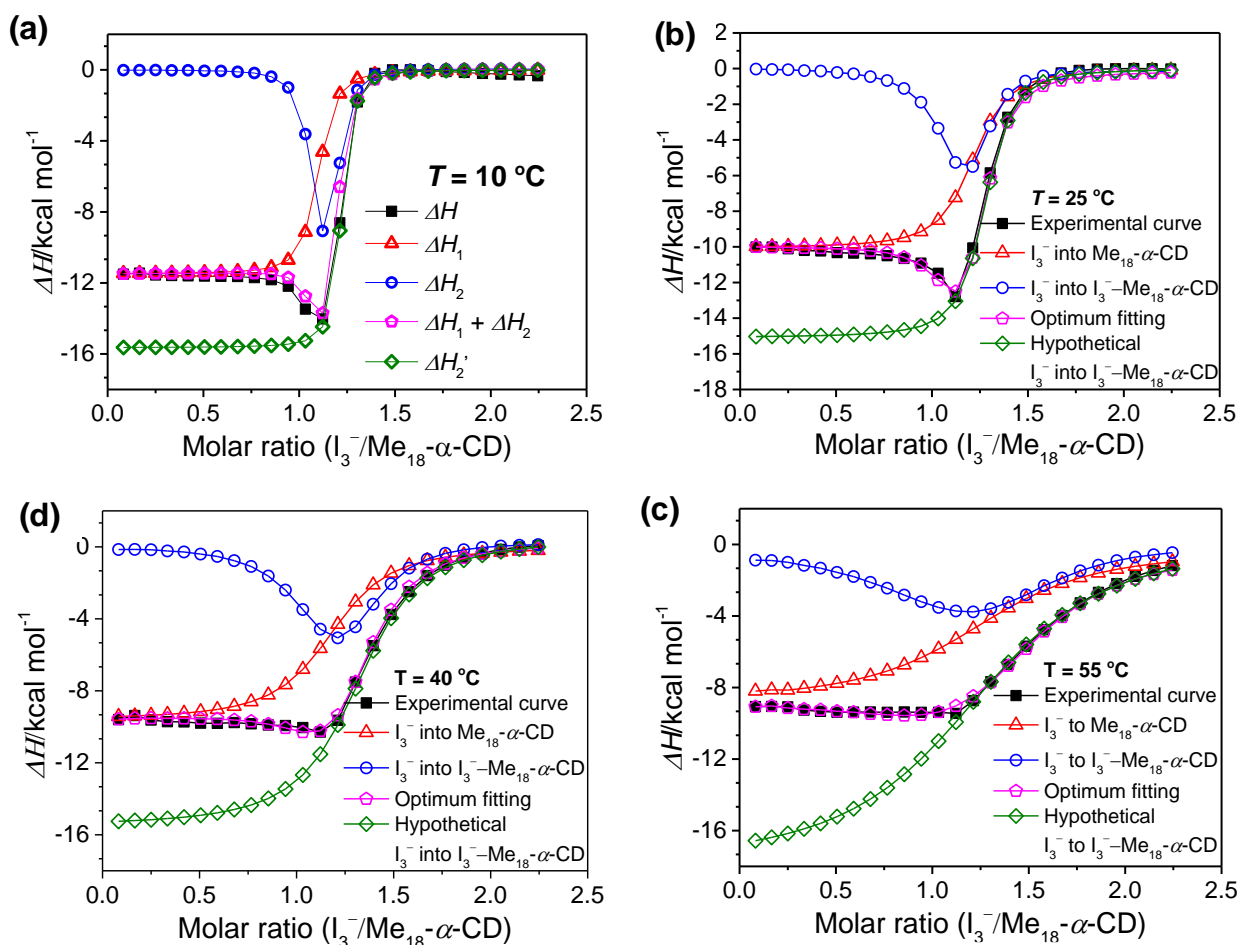


Figure 2-5. (a) Optimum fitting ΔH_1 (red triangles), ΔH_2 (blue circles), the sum of ΔH_1 and ΔH_2 (pink pentagons) and the experimental result (black squares) of $I_3^-/Me_{18}\text{-}\alpha\text{-CD}$ titration at 10 °C. $\Delta H_2'$ (green diamonds) is a hypothetical ITC curve for the second binding stage generated by the SSIS model with the absence of the initial binding stage. The enthalpy change in the figures is normalized. (b-d) Optimum fitting of the experimental titration curve for the sum of I_3^- into $Me_{18}\text{-}\alpha\text{-CD}$ and I_3^- into $I_3^-\text{-}Me_{18}\text{-}\alpha\text{-CD}$ at 25, 40 and 55 °C respectively.

To get insight into the unique ITC data, curve fitting was executed. As above mentioned, in the case of pristine $\alpha\text{-CD}$, the ITC curve can be fitted with a simple 1:1 binding model between the host and I_3^- (a simple set of identical sites, SSIS) as reported previously.^{20,26–28} In contrast, the SSIS model did not fit the ITC curve obtained for the $Me_{18}\text{-}\alpha\text{-CD}\text{-}I_3^-$ system (Fig. 2-4). The fitting was not satisfactory even by applying the TSIS (two sets of independent sites) model

where two kinds of sites bind independently to guest molecules. These observations indicate that the

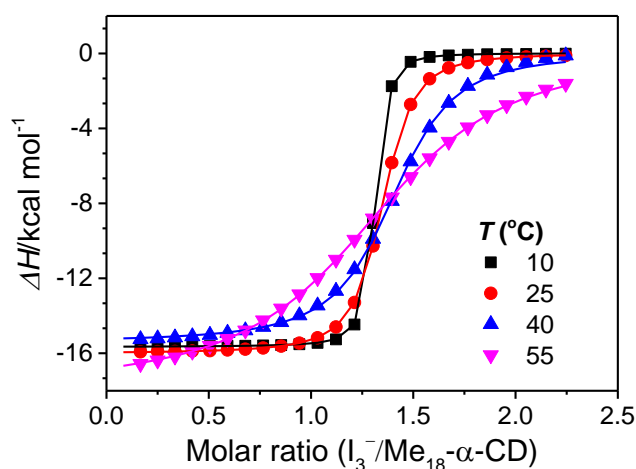


Figure 2-6 The ITC curves for the second binding stage, i.e., I_3^- into $Me_{18}\text{-}\alpha\text{-CD-I}_3^-$ at various temperatures.

second binding reaction in Eq. 2-2 occurs cooperatively with the complexation between I_3^- and $Me_{18}\text{-}\alpha\text{-CD}$ (Eq. 2-1). We therefore fitted the ITC curve to the model reported by Kataoka and coworkers, which is a modified model based on the SSIS.²⁹ In this model, the concentration of

Table 2.1. Parameters for initial and second binding stages.

$Me_{18}\text{-}\alpha\text{-CD} + I_3^- \rightarrow Me_{18}\text{-}\alpha\text{-CD-I}_3^-$				
	10 °C	25 °C	40 °C	55 °C
ΔH_1 (kcal mol ⁻¹)	-11.5	-10.1	-9.61	-8.89 ± 0.04
ΔS (cal K ⁻¹ mol ⁻¹)	-6.03	-8.15	-9.86	-10.28
$K_{as}/10^4$ (M ⁻¹)	215 ± 5	79.8 ± 0.5	18.1 ± 0.4	4.12 ± 0.13
$Me_{18}\text{-}\alpha\text{-CD-I}_3^- + I_3^- \rightarrow Me_{18}\text{-}\alpha\text{-CD-I}_5^- + I^-$				
ΔH_2 (kcal mol ⁻¹)	-15.6	-15.99	-15.39	-17.75
ΔS (cal K ⁻¹ mol ⁻¹)	-24.38	-29.35	-29.95	-41.64
$K_{as}/10^4$ (M ⁻¹)	564 ± 5	85.1 ± 0.3	21.5 ± 1.0	4.01 ± 0.04

the substance in the second reaction is generated by the initial reaction, and the experimental curve in Fig. 2-4 was fitted by the simultaneous control of these two interactions. The details of the fitting were revealed in experimental part. As shown in Fig. 2-5, the experimental ITC curve was successively fitted by the sum of ΔH_1 and ΔH_2 , derived from enthalpy changes

according to Eq. 2-1 and Eq. 2-2, respectively. The ITC curves for the second binding stage (Eq. 2-2) are described in Fig. 2-6. The thermodynamic parameters are shown in Table 2-1. The ITC curve of the initial binding stage, i.e., I_3^- into $Me_{18}\text{-}\alpha\text{-CD}$ is presented in the red

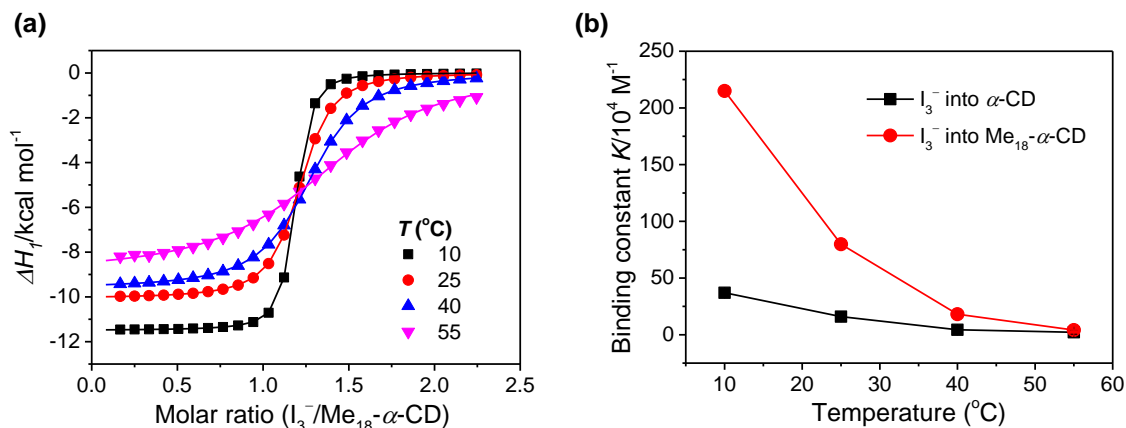


Figure 2-7. (a) The initial binding enthalpy (ΔH_1 in Fig. 3b) of the ITC curves for $Me_{18}\text{-}\alpha\text{-CD}$ with I_3^- at various temperature. (b) The temperature difference of the binding constant K observed for $\alpha\text{-CD}$ (black squares), $Me_{18}\text{-}\alpha\text{-CD}$ (red circles) with I_3^- .

triangles in Fig. 2-5. The shift of the stoichiometry from 1:1 to ca. 1.2:1 for the initial bonding stage should be attributed to the contribution of the second binding stage, which consumed a fraction of added I_3^- .

The complexation enthalpy between $Me_{18}\text{-}\alpha\text{-CD}$ and I_3^- at various temperature were extracted in Fig. 2-7a. The binding constants (K) of $Me_{18}\text{-}\alpha\text{-CD}$ and I_3^- were estimated by these fittings and were plotted in Fig. 2-7b. The K of pristine $\alpha\text{-CD}$ was also plotted in the figure, which is ca. 25 times larger at 10 °C than that observed at 55 °C as reported previously.²⁰ On the other hand, $Me_{18}\text{-}\alpha\text{-CD}$ shows remarkable temperature dependence and ca. 50-fold increase in K value was observed upon cooling the temperature from 55 °C to 10 °C. This larger change in K observed for the $Me_{18}\text{-}\alpha\text{-CD}$ and I_3^- enlarges the concentration difference of free I_3^- between the cold- and hot-branches of the cell.

The enhancement of S_e can be attributed to the changes in association enthalpy, and the increase of -1 kcal mol^{-1} in ΔH increases 0.06 mV/K . From Table S3, the initial binding enthalpy ΔH_I at $25 \text{ }^\circ\text{C}$ was $-10.1 \text{ kcal mol}^{-1}$ and the bonus of S_e was estimated to be 0.6 mV/K . On the other hand, the $\text{Me}_{18}\text{-}\alpha\text{-CD}$ enhance the S_e of the thermocell of 1.08 mV/K . This discrepancy indicates that the association of I_5^- into $\text{Me}_{18}\text{-}\alpha\text{-CD}$ further increased the concentration difference of I_3^- between both branches of the cell, which further enhances the Seebeck coefficient.

2.2.3. UV-vis spectroscopy

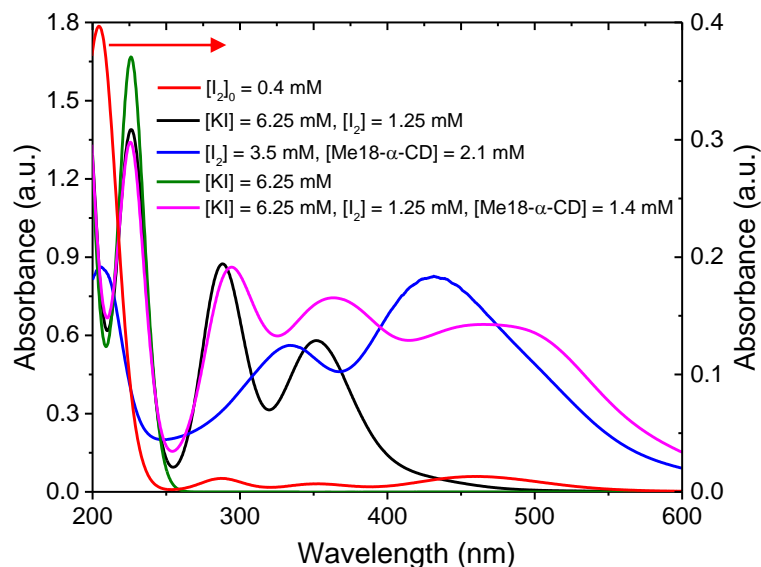


Figure 2-8. UV-Vis spectra of various aqueous solutions of 6.25 mM of KI (green); 6.5 mM of KI and 1.25 mM of I_2 (black); 0.4 mM of I_2 (red); 6.25 mM of KI, 1.25 mM of I_2 and 1.4 mM of Me18- α -CD (pink); and 3.5 mM of I_2 and 2.1 mM of Me18- α -CD, which were used to attribute all of the peaks in I_2 , KI and Me18- α -CD composed solutions.

In order to investigate the species present in the mixed solution of I_2 , KI and Methyl- α -CD, UV-vis spectroscopy was executed. The peaks were primarily assigned by using reference solutions (Fig. 2-8). As shown in Fig. 2-8, aqueous solution of pure KI has two peaks at 192 and 225 nm, which are attributed to the absorption peaks of I^- .^{30,31} When I_2 was added to the KI solution, new peaks emerged at 290 and 352 nm, which reflects the formation of I_3^- ion through Eq. 2-2.³⁰⁻³⁴



A saturated I₂ solution without KI has four peaks at 205, 290, 352, 460 nm, among which the peaks at 205 and 460 nm are attributed to I₂.^{30,31,33,34} The other two peaks at 290 and 352 nm are derived from the I₃⁻ ion generated by the hydrolysis of iodine, as described in literatures.³⁵⁻³⁷ The α-CD-I₃⁻ complex formed upon the addition of α-CD to the aqueous mixture of KI and I₂ gave almost identical peaks at 290 and 353 nm.^{27,28,37} Meanwhile, upon the addition of Me₁₈-α-CD, considerable red-shifts to 300 and 375 nm were observed (Fig. 2-8), reflecting the complexation by Me₁₈-α-CD according to Eq. 1. This red-shift in comparison with those of α-CD could be ascribed to the modified bond distance of I₃⁻ in the relatively deeper and more hydrophobic cavity of Me₁₈-α-CD, which may have affected the electronic structure of I₃⁻.³⁸ The component observed for the mixture of I₂ and Me₁₈-α-CD at 430 nm is attributed to Me₁₈-α-CD-I₂, which is blue shifted due to the elevated LUMO level of I₂ by the interaction with oxygen atoms of Me₁₈-α-CD.³⁹⁻⁴² Furthermore, a shoulder peak at 503 nm was observed in the spectrum (Fig. 2-8), which has never been reported in the previous solution systems. In the solid state, the absorption around 500 nm has been assigned to that of I₅⁻ anion,⁴³⁻⁴⁸ and we attribute the peak at 503 nm to Me₁₈-α-CD-I₅⁻. The complex is formed through Eq. 2-2.

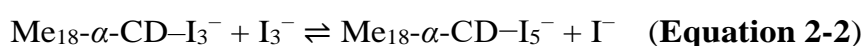


Table 2-2. The summary of the attribution of peaks on UV-vis spectra

	I ⁻	I ₂	Me ₁₈ -α-CD-I ₂	I ₃ ⁻	Me ₁₈ -α-CD-I ₃ ⁻	Me ₁₈ -α-CD-I ₅ ⁻
Wavelength	192	205	326	290	298	503
(nm)	225	460	445	352	372	

As described above, the Me₁₈-α-CD provides deeper hydrophobic cavity as compared to that of α-CD (Fig. 2-1), which must have stabilized the I₅⁻ species in the form of Me₁₈-α-CD-I₅⁻ complex. The assignment of the six peaks was summarized in Table 2-2. I₅⁻ ions have been found in the solid polarizer film for liquid crystal displays, but to date, it has not been identified

to exist in aqueous solutions. Thus, the formation of $\text{Me}_{18-\alpha}\text{-CD-I}_5^-$ in aqueous solution provides a means to investigate the property of the discrete I_5^- ion.

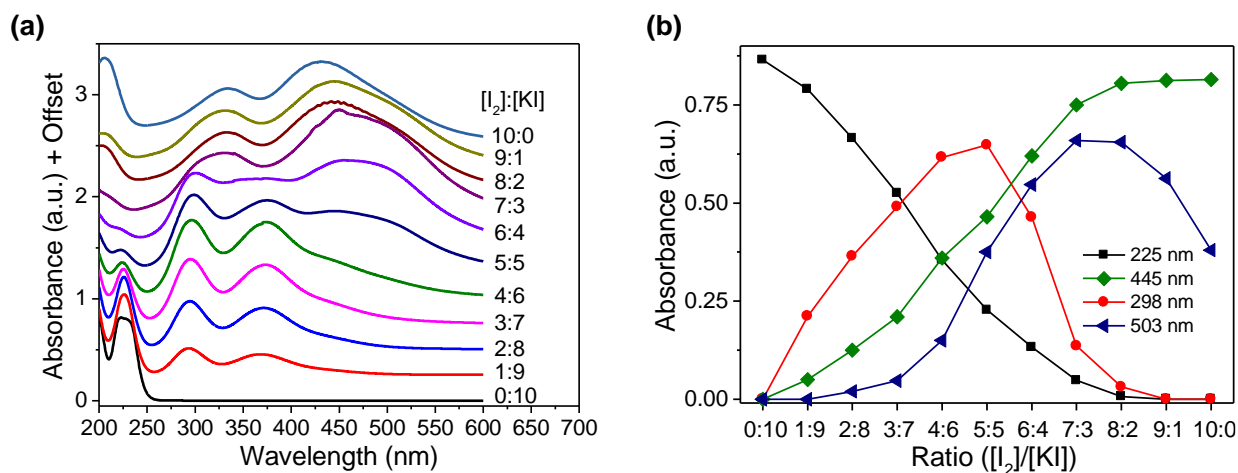


Figure 2-9. (a) The UV-vis spectra of aqueous solutions with varying concentrations. (b) The absorbance of all peaks on UV spectra plotted against the ratio of $[\text{I}_2]/[\text{KI}]$. $[\text{Me}_{18-\alpha}\text{-CD}] = 2.1 \text{ mM}$.

The existed six peaks were further analyzed by Job's method.⁴⁹ Peaks in Fig. 2-9a corresponds to I^- (225 nm), $\text{Me}_{18-\alpha}\text{-CD-I}_3^-$ (298 and 372 nm), $\text{Me}_{18-\alpha}\text{-CD-I}_2$ (326 and 445 nm) and $\text{Me}_{18-\alpha}\text{-CD-I}_5^-$ (503 nm). These peaks were separated using Gaussian fitting and the peak intensities were plotted against the initial concentration ratio of I_2 and KI, as shown in Fig. 2-9b. The peak intensity of I^- at 225 nm monotonically decreases with the increase in concentration ratio. Meanwhile, the absorbance of $\text{Me}_{18-\alpha}\text{-CD-I}_3^-$ at 298 nm, increased almost proportionally at a low concentration of I_2 . After reaching maximum intensity at the ratio of 5:5, the 298 nm-peak decreased beyond that ratio. The peak at 445 nm ($\text{Me}_{18-\alpha}\text{-CD-I}_2$) naturally shows a monotonic increase upon increasing I_2 concentration. The peak at 503 nm ($\text{Me}_{18-\alpha}\text{-CD-I}_5^-$) showed a maximum at the $[\text{I}_2]/[\text{KI}]$ ratio of 7:3 to 8:2, and decreased beyond that ratio.

If the triiodide is the only polyiodide product in the aqueous mixture of KI and I_2 , the plot of triiodide species (at 298 nm) should give a parabolic curve. The sharp decrease of the $\text{Me}_{18-\alpha}$ -

CD-I₃⁻ (298 nm) and the increase of the Me₁₈-α-CD-I₅⁻ (503 nm) species in between the ratio of 5:5 to 7:3 indicate that when the ratio of I₂ is higher than 5:5, the Me₁₈-α-CD-I₃⁻ react with I₃⁻ to give the Me₁₈-α-CD-I₅⁻ complex through Eq 2-2.

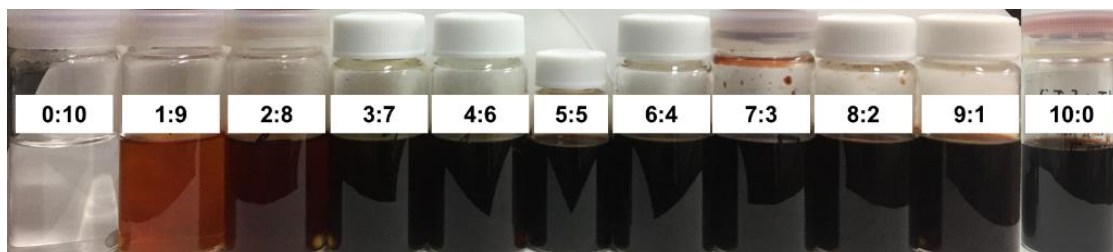


Figure 2-10. The appearance of solutions 2 at room temperature. Because of the Me₁₈-α-CD inclusion and iodine hydrolysis, an excess of iodine can be dissolved in water even at the high ratio of 10:0.

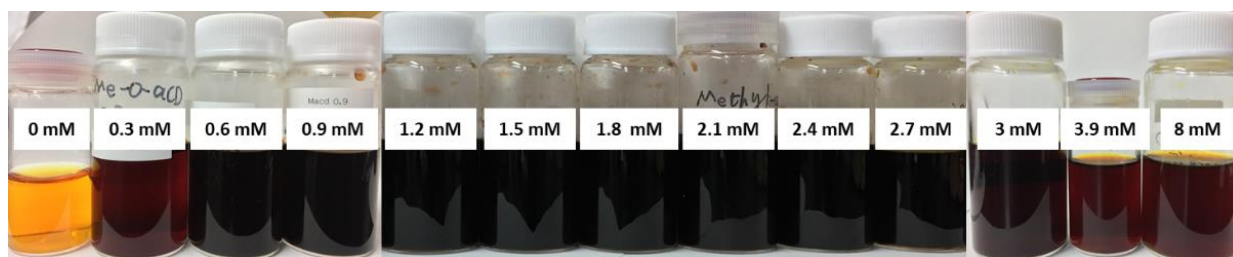


Figure 2-11. The pictures of solutions 1 (see Table S1) at varied Me₁₈-α-CD concentrations. The color of solutions changes from yellow to red black then to deep red-black. When the concentration of Me₁₈-α-CD is increased beyond 3 mM, the color returns to red black again. The change of the color indicates the formation of Me₁₈-α-CD-I₅⁻ and its transformation to Me₁₈-α-CD-I₃⁻ species at higher Me₁₈-α-CD concentrations.

Although molecular iodine is slightly soluble in water (1.18 mM, 20 °C),⁵⁰⁻⁵² no precipitation was observed in our experiments even in the absence of added KI. This would be attributed to the high water solubility of Me₁₈-α-CD-I₂ and formation of Me₁₈-α-CD-I₅⁻. In addition, the weak acidity of saturated iodine solution pH 6.6 can be associated with the hydrolysis of iodine.

The appearance of each solution was shown in Fig. 2-10. The dark color of the solution 10:0 indicates the coexistence of $\text{Me}_{18}\text{-}\alpha\text{-CD-I}_2$ and $\text{Me}_{18}\text{-}\alpha\text{-CD-I}_5^-$.

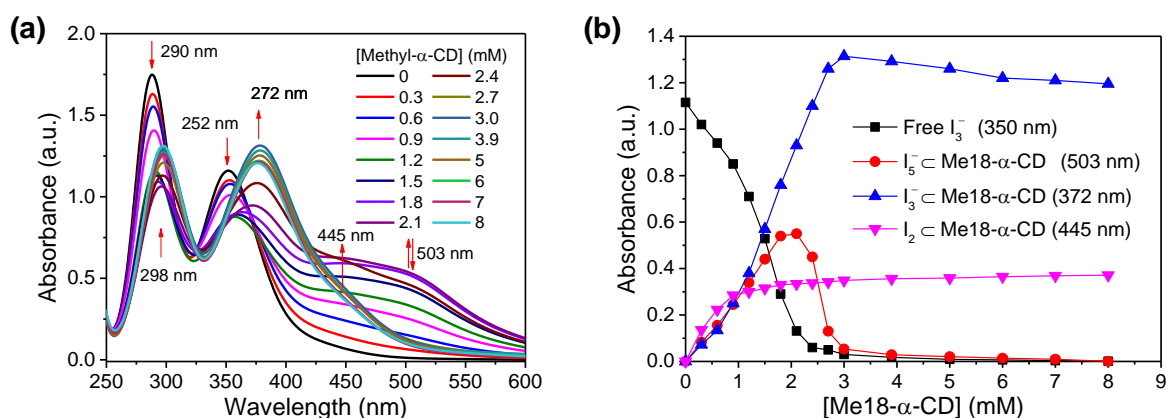
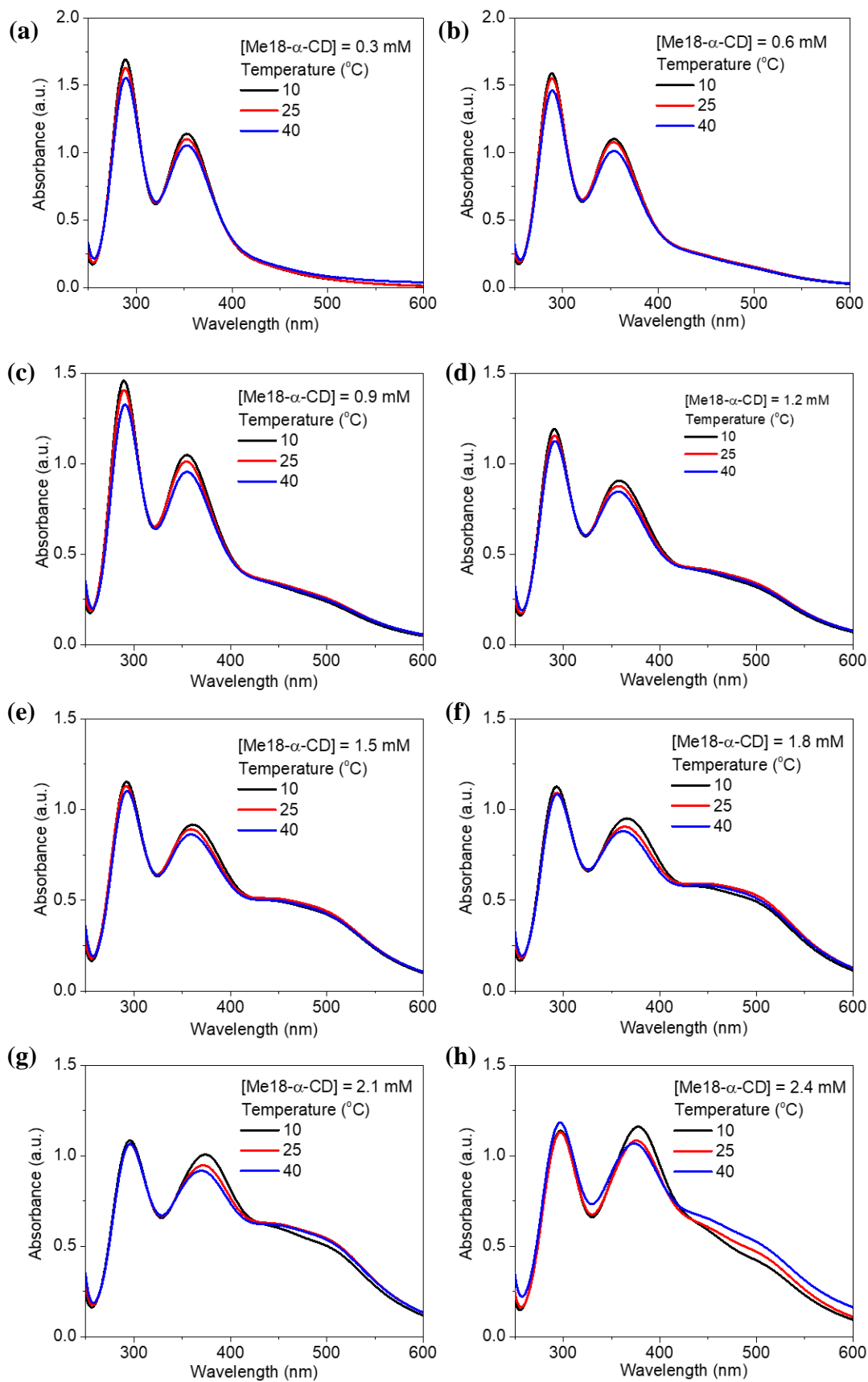


Figure 2-12. (a) The UV-vis spectra of Solution 1 with various concentration of $\text{Me}_{18}\text{-}\alpha\text{-CD}$ at $25\text{ }^\circ\text{C}$. (b) The plots of the peak absorbance of I_3^- , $\text{Me}_{18}\text{-}\alpha\text{-CD-I}_3^-$, $\text{Me}_{18}\text{-}\alpha\text{-CD-I}_5^-$, and $\text{Me}_{18}\text{-}\alpha\text{-CD-I}_2$ in (a). each solution was shown in Fig. 2-10. The dark color of the solution 10:0 indicates the coexistence of $\text{Me}_{18}\text{-}\alpha\text{-CD-I}_2$ and $\text{Me}_{18}\text{-}\alpha\text{-CD-I}_5^-$.

Based on these spectral analyses, the concentration of the iodide species in the thermocell was then estimated by UV-vis spectroscopy. Fig. 2-12 shows UV spectra with various concentration of $\text{Me}_{18}\text{-}\alpha\text{-CD}$ at $25\text{ }^\circ\text{C}$. As discussed previously, two peaks of I_3^- at 290 and 352 nm show a red shift upon the addition of $\text{Me}_{18}\text{-}\alpha\text{-CD}$, which correspond to the formation of $\text{Me}_{18}\text{-}\alpha\text{-CD-I}_3^-$. Other peaks at 445 and 503 nm are attributed to $\text{Me}_{18}\text{-}\alpha\text{-CD-I}_2$ and $\text{Me}_{18}\text{-}\alpha\text{-CD-I}_5^-$, respectively. Upon increasing the concentration of $\text{Me}_{18}\text{-}\alpha\text{-CD}$, peaks at 445 and 503 nm increased and the color of the solution showed changes from yellow to deep red black (Fig. 2-11), which reflect the formation of $\text{Me}_{18}\text{-}\alpha\text{-CD-I}_5^-$. Upon the addition of $\text{Me}_{18}\text{-}\alpha\text{-CD}$ at higher concentrations beyond 3 mM, the color of the solution returns to weak red (Fig. 2-11). To understand these color changes, the intensity of the peaks is plotted in Fig. 2-12b with varied concentration of the host. As the absorbance of I_3^- (290 nm) decreases, absorption intensities for $\text{Me}_{18}\text{-}\alpha\text{-CD-I}_3^-$ (372 nm) and $\text{Me}_{18}\text{-}\alpha\text{-CD-I}_2$ (445 nm) species increased. The absorbance

of $\text{Me}_{18}\text{-}\alpha\text{-CD-I}_3^-$ and $\text{Me}_{18}\text{-}\alpha\text{-CD-I}_2$ reached almost constant when the concentration of $\text{Me}_{18}\text{-}\alpha\text{-CD}$ was elevated to ca. 3 mM. The absorbance of $\text{Me}_{18}\text{-}\alpha\text{-CD-I}_5^-$ increased similarly as that



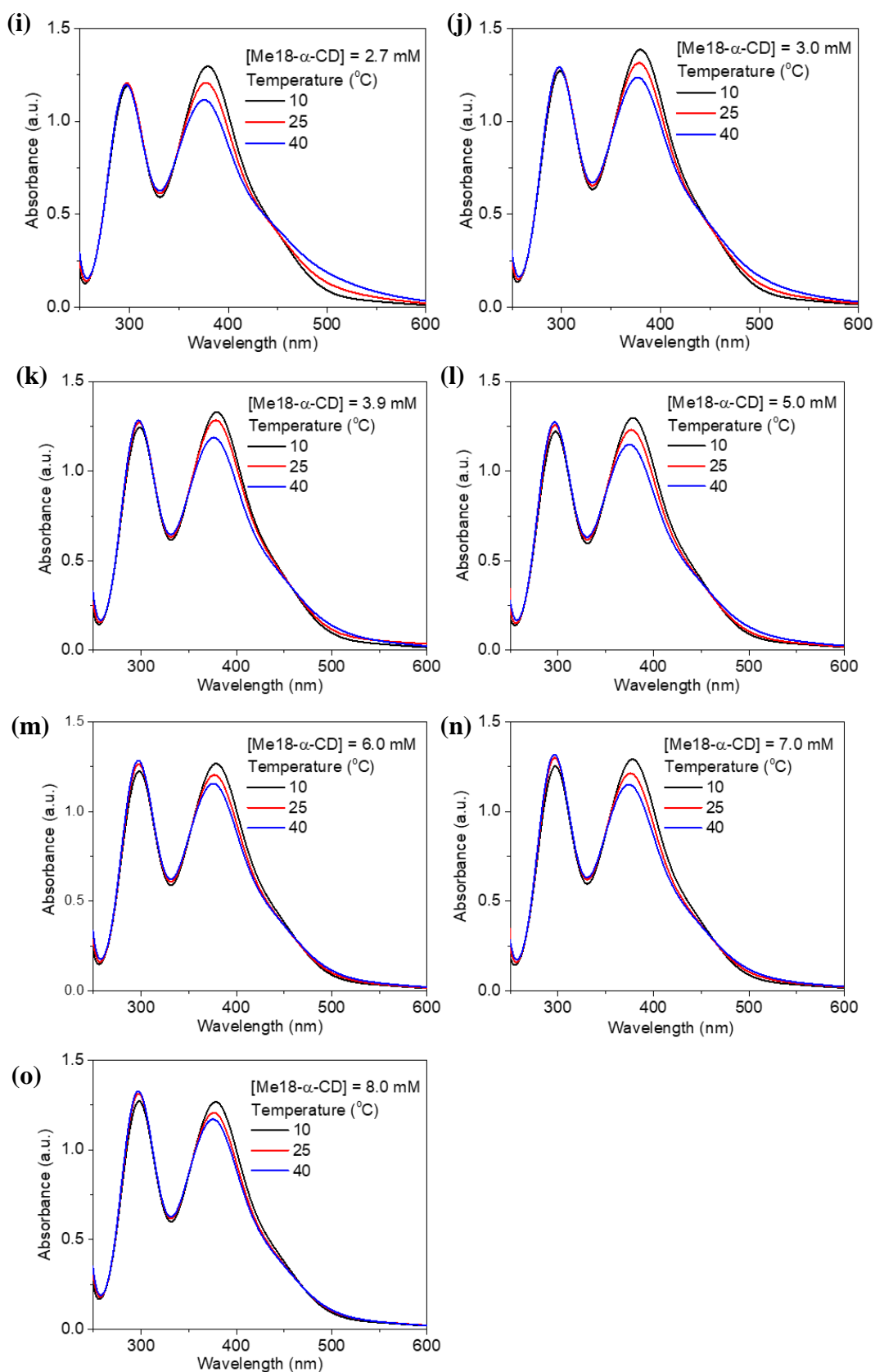
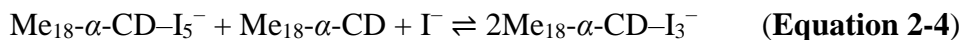


Figure 2-12. The UV-vis spectra of Solution 1 with different concentrations of Me₁₈-α-CD. Temperatures at 10, 25 and 40 °C.

of $\text{Me}_{18}\text{-}\alpha\text{-CD-I}_3^-$ below the $\text{Me}_{18}\text{-}\alpha\text{-CD}$ concentration of 2.1 mM, but it showed abrupt decrease beyond this host concentration. It indicates that $\text{Me}_{18}\text{-}\alpha\text{-CD-I}_5^-$ underwent comproportionation to two $\text{Me}_{18}\text{-}\alpha\text{-CD-I}_3^-$ molecules according to Eq. 2-4.⁵³⁻⁵⁶



The increase in V_{oc} and S_e values of the thermocell could be associated with the concentration difference of free I_3^- ions between the lower- and higher-temperature half-cells, which undergoes the reduction reaction in the thermocell.²⁰ Therefore, the temperature dependence of the concentration of free I_3^- was estimated by UV-vis spectroscopy under various host concentrations. All spectra are revealed in Fig. 2-12, and the peak intensity of free I_3^- species

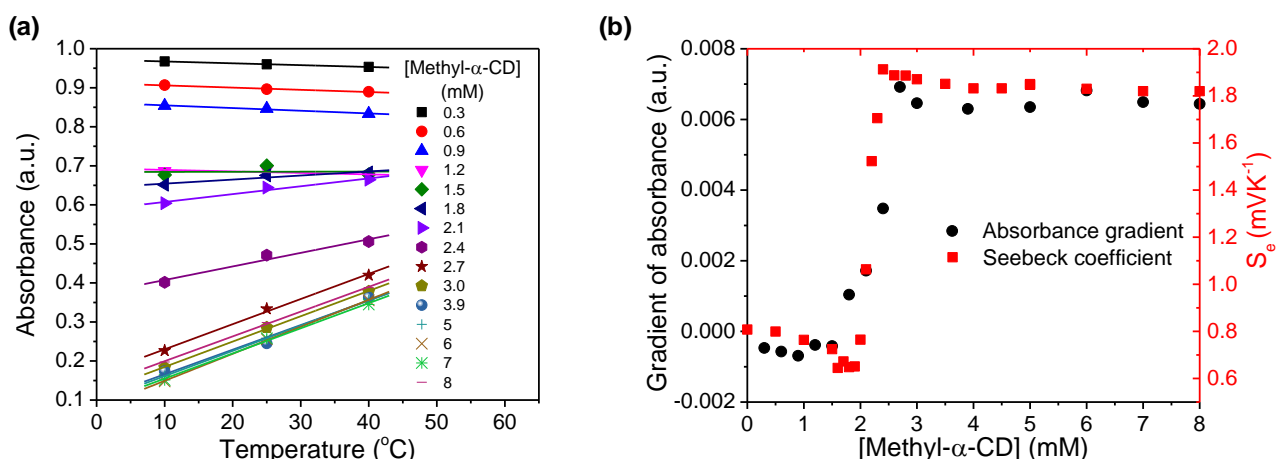


Figure 2-13. (a) The temperature dependence of the absorbance of free I_3^- species at 352 nm at various concentration of $\text{Me}_{18}\text{-}\alpha\text{-CD}$ at $[\text{KI}] = 12.5$ mM, $[\text{I}_2] = 2.5$. The slope of the graph changes from negative to positive. (b) The temperature gradient of the UV peak at 352 nm and S_e at various concentration of $\text{Me}_{18}\text{-}\alpha\text{-CD}$. They are in good agreement with each other.

at 352 nm was estimated and plotted at various temperature and $\text{Me}_{18}\text{-}\alpha\text{-CD}$ concentrations as shown in Fig. 2-13a. At lower concentrations of $\text{Me}_{18}\text{-}\alpha\text{-CD}$, a slight decrease of the peak intensity was observed with increasing its temperature. The peak intensity of free I_3^- also decreased with increasing the concentration of $\text{Me}_{18}\text{-}\alpha\text{-CD}$. Upon increasing temperature, a

relatively large increase of free I_3^- signal was observed for the aqueous $Me_{18}\text{-}\alpha\text{-CD}$ above the host concentration of 1.8 mM. This is ascribed to the decrease in the binding constant between $Me_{18}\text{-}\alpha\text{-CD}$ and I_3^- , and the dissociation of the complex to liberate free I_3^- species by heating.

The slope of the lines of Fig. 2-13a at various $Me_{18}\text{-}\alpha\text{-CD}$ concentration was plotted in Fig. 2-13b. The change of the slope drastically increases in the concentration range from 2.0 to 2.2 mM. The change of the I_3^- concentration affects the S_e , and the trend of the graph quite resembles the curve of the S_e . Thus, the enhancement of S_e of the thermocell can be attributed to the host-guest interaction between $Me_{18}\text{-}\alpha\text{-CD}$ and I_3^- .

The temperature dependency of UV-vis spectra was recorded in Fig. 2-14. Peak intensities at 370 and 503 nm decreases with increasing temperature. This result shows that the ΔH of host-guest interaction of $Me_{18}\text{-}\alpha\text{-CD}$ and pentaiodide is negative. This result is in good agreement with previous literature.

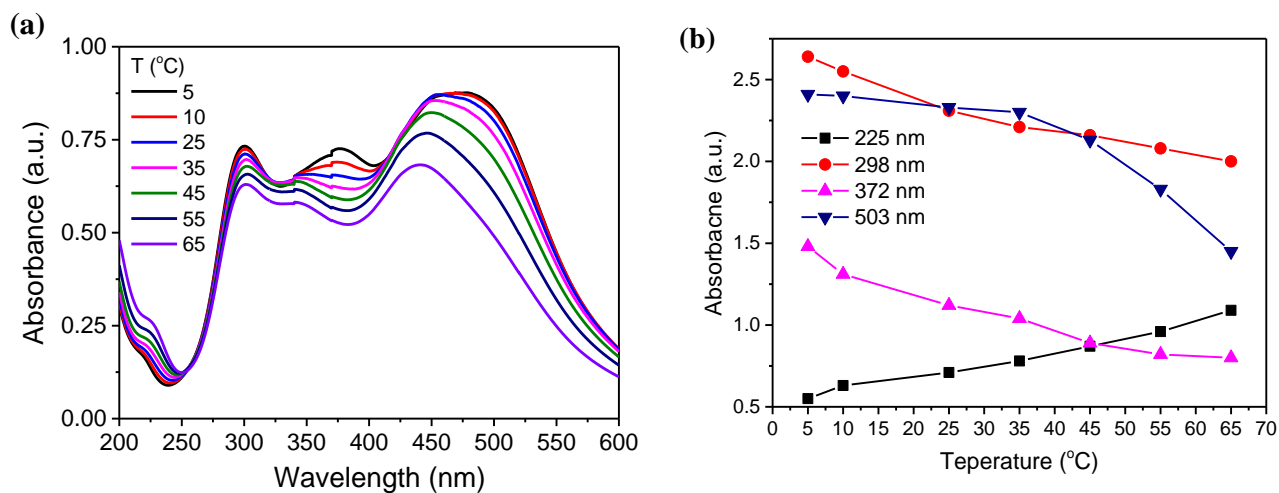


Figure 2-14. (a) UV-vis spectra of KI (1.4 mM), I_2 (2.1 mM) and $Me_{18}\text{-}\alpha\text{-CD}$ (2.1 mM) at various temperature. Peak at ca. 503 nm was attributed to $Me_{18}\text{-}\alpha\text{-CD-I}_5^-$. (b) The peak intensities were plotted with various temperature.

2.2.4. Raman spectroscopy

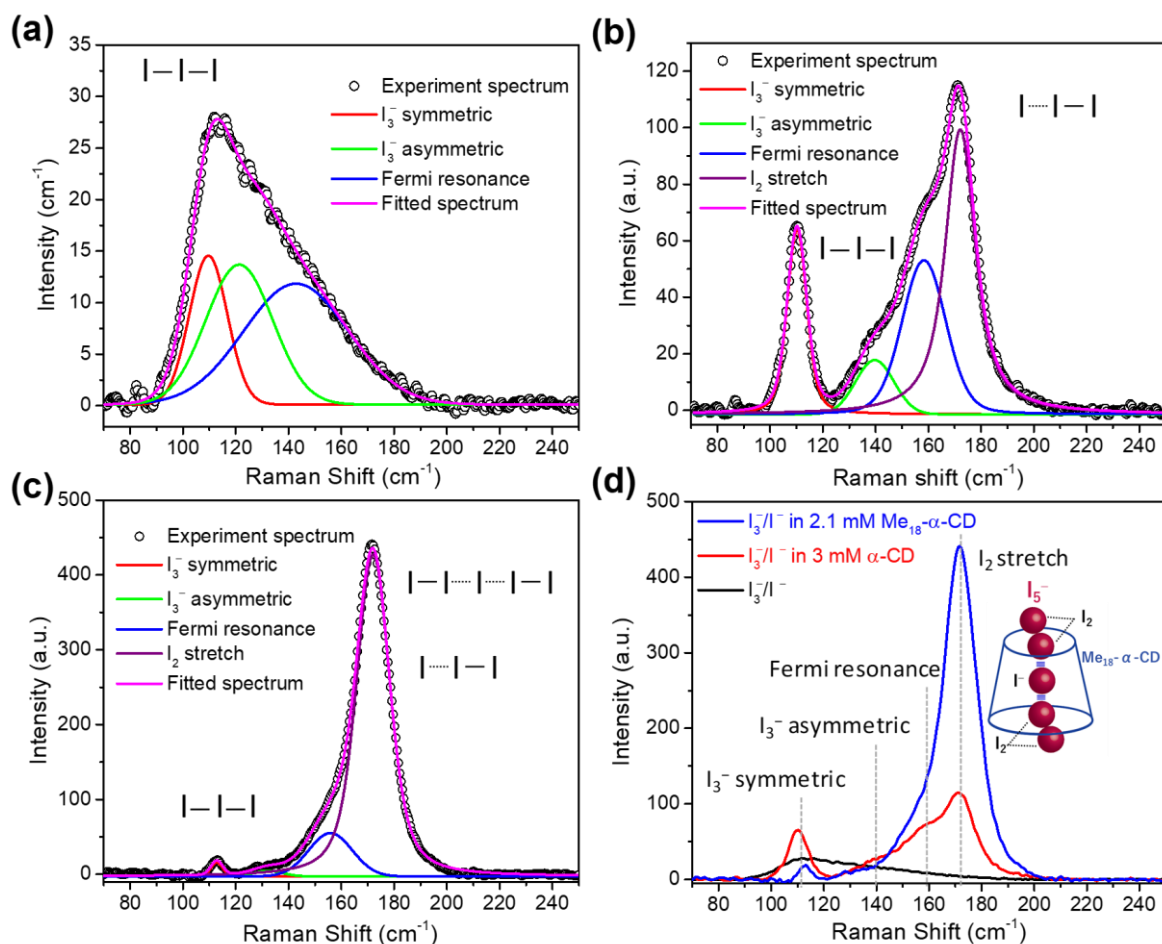


Figure 2-15. Raman spectra of (a) aqueous solution of KI (12.5 mM) and I₂ (2.5 mM), (b) 3 mM α -CD in addition of (a) and (c) 2.1 mM Me₁₈- α -CD in (a). Each spectrum was fitted with Pseudo Voigt functions. All experimental data were overlapped in (d).

The formation of Me₁₈- α -CD-I₅⁻ was further confirmed by Raman spectroscopy (Fig. 2-15) by the increase of I₂ stretching signal at ca. 170 cm⁻¹, which corresponds to the I₅⁻ as an adduct of I⁻·2I₂.^{43,57-59}

UV-vis spectra reveal that I₃⁻/I⁻ aqueous solution in 3 mM α -CD and 2.1 mM Me₁₈- α -CD possess the maximum I₃⁻ and I₅⁻ respectively, thus the Raman spectra were recorded at such conditions and the corresponding fittings are shown in Fig. 2-15. A triiodide cation shows a strong peak at ca. 110 cm⁻¹ and a weak peak at ca. 140cm⁻¹,⁵⁹⁻⁶³ which are attributed to the symmetric (ν_1) and asymmetric (ν_2) stretch vibration respectively. Another weak peak at 160 cm⁻¹ is assigned to the Fermi resonance

between ν_1 and the overtone of bending mode (ν_3) of triiodide, though the ν_3 is proposed to be at 50-70 cm^{-1} while it is very weak and not observed in the spectra.^{59,61,64} When 3 mM α -CD was added to the I_3^-/I^- solution, the increment of the peak intensity of ν_1 indicates that the host-guest interaction. A new peak appeared at ca. 170 cm^{-1} , which was assigned to the I-I stretch mode, and a fraction of the captured I_3^- in α -CD should be described as an adduct of $\text{I}^- \cdot \text{I}_2$ ($\nu_{\text{I-I}} = 170 \text{ cm}^{-1}$).^{59,61,64} In the case of $\text{Me}_{18}\text{-}\alpha\text{-CD}$ as a host, the intensity of ν_1 peak decreased and the of a peak at 170 cm^{-1} significantly enhanced. I_5^- in the solid state exists as an adduct of $\text{I}^- \cdot 2\text{I}_2$ or $\text{I}_3^- \cdot \text{I}_2$,^{57-59,61,62} and a peak at 170 cm^{-1} was enhanced in the case of $\text{I}^- \cdot 2\text{I}_2$. Thus, $\text{Me}_{18}\text{-}\alpha\text{-CD}$ stabilizes the $\text{I}^- \cdot 2\text{I}_2$ adduct in aqueous solution.

2.2.5. Temporal stability of the thermocell

The power output can be obtained by applying external load voltage (V) to the thermocell (Fig 2-16) and the measurement of the I - V curves. The maximum power output at each condition was obtained by the plot of power and voltage (Fig. 2-16b). The addition of the supporting electrolyte, KCl, to the supramolecular thermocell leads to the increase in the current output, as reported previously.¹⁸ However, in the previous study, precipitation emerged when pristine α -CD was used as a host matrix, and the power output shows a drastic degradation in 6 hrs. The precipitation occurred due to the

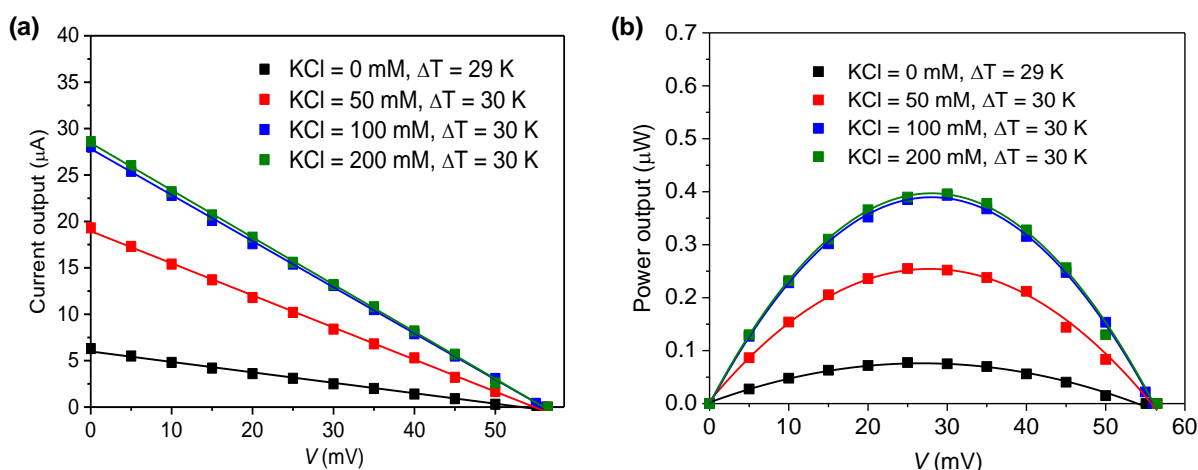


Figure 2-16. (a) Current output and (b) power out of the $\text{Me}_{18}\text{-}\alpha\text{-CD}$ -based supramolecular thermocell. Temperature difference (ΔT) was controlled between 29–30 K, and the supporting electrolyte KCl was increased from 0 to 200 mM. Errors in the figure are smaller than the size of the squares.

hydrogen bonding between the α -CD- I_3^- species, and this was the fatal flaw for the long-term operation of α -CD-based thermocells. Meanwhile, such precipitation was not observed when KCl was added to the aqueous mixtures of Me₁₈- α -CD, I₂ and KI.

Apparently, methylation of the hydroxy groups effectively prevented the precipitation. Fig 2-17 shows time dependence of the power output obtained for the Me₁₈- α -CD-based

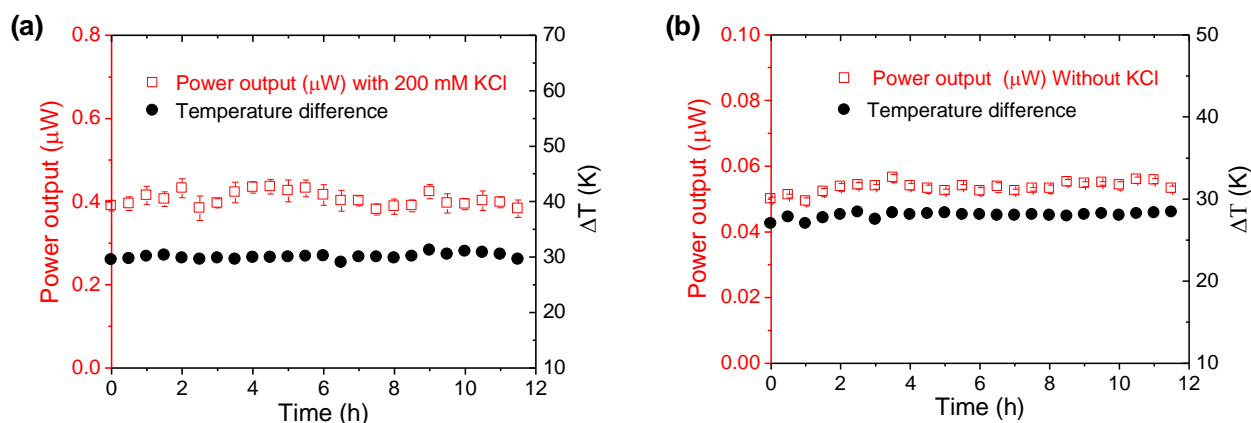


Figure 2-17. Time dependency of the power output of the thermocell (KI = 12.5 mM, I₂ = 2.5 mM, Me₁₈- α -CD = 4 mM) with (a) and without (b) KCl. The temperature difference was controlled at ca. 29 K (a) and 30 K (b), which were monitored and added to these figures.

supramolecular thermocell with and without KCl. As shown in the figure, stable power output was observed, reflecting the stability of Me₁₈- α -CD- I_3^- complex in aqueous media. The stable power output of Me₁₈- α -CD- I_3^- based thermocell, normalized by the temperature difference, is 0.21 mW m⁻² K⁻¹, which is ca. 2.3 times higher compared with the α -CD- I_3^- based thermocell after continuous working for 6 hrs (0.09 mW m⁻² K⁻¹)

2.3. Conclusion

Me₁₈- α -CD was added to I^-/I_3^- thermocell and the Seebeck coefficient was improved by host-guest interactions. Compared to pristine α -CD, Me₁₈- α -CD shows stronger interaction with I_3^- , and the S_e of the thermocell was enhanced up to 1.9 mV K⁻¹ without precipitation. The observed S_e value is the highest among the pure-water thermocell system.

UV-vis spectroscopy reveals that the I_5^- was captured in the aqueous $Me_{18}\text{-}\alpha\text{-CD}$, in addition to $Me_{18}\text{-}\alpha\text{-CD}\text{-}I_3^-$. This result is the first observation of I_5^- formed in the solution system. The binding constants of $Me_{18}\text{-}\alpha\text{-CD}$ and I_3^- was estimated by ITC measurement. The estimated enhancement of S_e was ca. 0.6 mV K^{-1} . The additional enhancement of S_e was derived from the formation of I_5^- , which boosted the concentration difference between the hot and cold branches of the cell. Thermal change of the free I_3^- concentration was evaluated by UV-vis measurement, which has resembled tendency to the S_e trends. The methylation of the hydroxyl groups in $Me_{18}\text{-}\alpha\text{-CD}$ effectively prevented the formation of hydrogen-bonded polymer complexes observed for the $\alpha\text{-CD}\text{-}I_3^-$ complex. As a result, the absence of precipitation in the present $Me_{18}\text{-}\alpha\text{-CD}/I_3^-$ system offered high durability, which has been a critical issue in the previous $\alpha\text{-CD}\text{-}I_3^-$ system. These results indicate that the precise design of the host-guest interaction is imperative to improve the thermocell performance.

2.4. Experimental

2.4.1. Materials and sources

Iodine (99.8%), Potassium iodide (99.5%) and Potassium chloride (>99%) were purchased from Kanto Chemical Co. Inc. (Japan). α -Cyclodextrin (α -CD) and hexakis(2,3,6-*O*-Me)- α -cyclodextrin (Me₁₈- α -CD) were purchased from Cyclodextrin-Shop of AraChem (Tilburg, Netherlands). All reagents were used without any further purification.

2.4.2. Preparation of aqueous solution

Various kinds of stock solutions were prepared as summarized in [Table 2-3](#) and [Table 2-4](#).

Solution 1: I₂ (25.4 mg, 1.0 mmol), KI (83 mg, 5.0 mmol) and various amount of Me₁₈- α -CD were dissolved into 40 ml water so that initial concentration of KI and I₂ to be 12.5 and 2.5 mM, respectively. The concentration of Me₁₈- α -CD was listed in [Table 2-3](#). The solutions were called as S1-x where x corresponds to the concentration of Me₁₈- α -CD (mM).

Table 2-3. The mixing conditions of Solution 1.

	I ₂ (mM)	KI (mM)	Me ₁₈ - α -CD (mM)
S1-0.0	2.5	12.5	0
S1-0.3	2.5	12.5	0.3
S1-0.6	2.5	12.5	0.6
S1-0.9	2.5	12.5	0.9
S1-1.2	2.5	12.5	1.2
S1-1.5	2.5	12.5	1.5
S1-1.8	2.5	12.5	1.8
S1-2.1	2.5	12.5	2.1
S1-2.4	2.5	12.5	2.4
S1-2.7	2.5	12.5	2.7
S1-3.0	2.5	12.5	3.0
S1-3.9	2.5	12.5	3.9
S1-5.0	2.5	12.5	5.0
S1-6.0	2.5	12.5	6.0
S1-8.0	2.5	12.5	8.0

Solution 2: Solutions containing various I₂/KI ratio were prepared. The concentration of each solution was listed in Table 2-4. These solutions are called S2-a:b where a:b corresponds to the ratio of I₂ and KI.

Table 2-4 The mixing conditions of Solution 2.

	I ₂ (mM)	KI (mM)	Me ₁₈ - α -CD (mM)
S2-0:10	0	3.50	2.10
S2-1:9	0.35	3.15	2.10
S2-2:8	0.70	2.80	2.10
S2-3:7	1.05	2.45	2.10
S2-4:6	1.40	2.10	2.10
S2-5:5	1.75	1.75	2.10
S2-6:4	2.10	1.40	2.10
S2-7:3	2.45	1.05	2.10
S2-8:2	2.80	0.70	2.10
S2-9:1	3.15	0.35	2.10
S2-10:0	3.50	0	2.10

2.4.3. Seebeck coefficient measurements

40 ml of solution 1 (S1-0.0 to S1-8.0) were poured into the H-shaped glass cell consists of two half-cells soaked into a couple of water baths at different temperature (Fig. 2-18). Each half-cell has

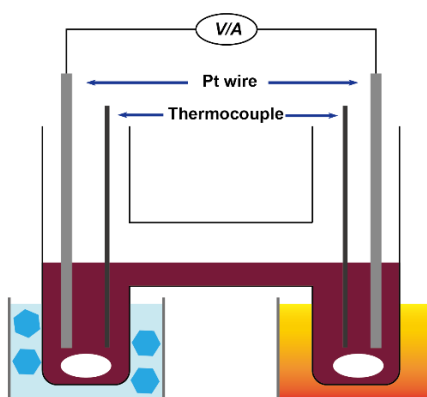


Figure 2-18. Schematic illustration of the H-shaped cell. The two half-cells were immersed in cold and hot water baths. A stirrer was put into each side to accelerate the thermal equilibrium. Two platinum wire electrodes were used to measure the open circuit voltage (V_{oc}) and the temperature difference was evaluated by thermocouples.

a diameter of ca. 2 cm and the distance between them is ca. 10 cm for creating a stable temperature

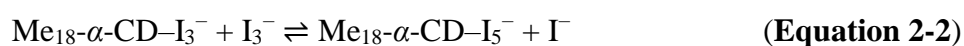
difference. The temperatures inside the half-cells were monitored with thermometers (TM201, AS ONE, Japan) and the cold side was kept at approximately 10 °C. Meanwhile, the electrolyte was stirred during the measurements to accelerate the equilibrium in the cell. Platinum wires ($\varphi = 1$ mm) were washed with concentrated sulfuric acid and used as electrodes for measuring a potential difference generated by the temperature difference. The potential difference was recorded by a source meter 2401 (KEITHLEY).

2.4.4. Isothermal titration calorimetry (ITC) measurements

The MicroCal VP-ITC titrator (LLC, Northampton, Ma, USA) was used for the calorimetric titrations. An aqueous solution of 13.5 mM of KI and 3.5 mM of I₂ was previously degassed using a vacuum degasser Thermovac (MicroCal, LLC, Northampton, Ma, USA). The solution was drawn into the syringe (250 μ l). Another aqueous solution containing 0.3 mM of Me₁₈- α -CD was also degassed and introduced into the ITC cell (1.4 ml). Data were collected during twenty-five injections of 10 μ l I₃⁻/I⁻ titrant into Me₁₈- α -CD titrate (duration 24 s) at 10, 25, 40 and 55 °C with stirring at 310 rpm and 240 s injection spacing.

The fitting model is not the general single set of identical sites (SSIS) or two sets of independent sites (TSIS), as discussed in the manuscript. Thus, the experimental results were analyzed by a novel fitting method based on the single set of identical sites (SSIS).

In the novel fitting model, the concentration of the substances in Eq. 2 is dependent on the initial binding reaction (Eq. 1).



The total heat generated can be regarded as a sum of Eq. 1 and Eq. 2 and generated heat at each injection can be written as Eq. S1,

$$\Delta Q(i) = \Delta Q(i)_1 + \Delta Q(i)_2 \quad (\text{Equation 2-3})$$

where $\Delta Q(i)$ is the heat generated of the i^{th} injection step, $\Delta Q(i)_1$ and $\Delta Q(i)_2$ are heat generated by

Eq. 2-1 and Eq. 2-2, respectively.

The reaction of each step can be fitted by SSIS model.

2.4.4.1. SSIS model

The SSIS model is introduced as follows.^{29,65,66}

K = Binding constant;

n = The number of the binding sites;

V_o = Cell volume;

M_t = The total concentration of host molecules in V_o ;

X_t and $[X]$ are total and free concentrations of guest molecules;

Θ = the fraction of binding sites occupied by a guest.

The binding constant K and the relationship of the total and free guest are described as:

$$K = \frac{\Theta}{(1 - \Theta)[X]} \quad \text{(Equation 2-4)}$$

$$X_t = [X] + n\Theta M_t \quad \text{(Equation 2-5)}$$

Combing Eq. S1 and Eq. S2 gives

$$\Theta^2 - \Theta \left[1 + \frac{X_t}{nM_t} + \frac{1}{nKM_t} \right] + \frac{X_t}{nM_t} = 0 \quad \text{(Equation 2-6)}$$

The total heat content Q of the solution contained in V_o at fractional saturation Θ is

$$Q = n\Theta M_t \Delta H V_o \quad \text{(Equation 2-7)}$$

Where ΔH is the molar heat of guest binding. Solving the quadratic equation (Eq. 2-6) for Θ and then substituting this into Eq. 2-7 gives

$$Q = \frac{nM_t \Delta H V_o}{2} \left[1 + \frac{X_t}{nM_t} + \frac{1}{nKM_t} - \sqrt{\left(1 + \frac{X_t}{nM_t} + \frac{1}{nKM_t} \right)^2 - \frac{4X_t}{nM_t}} \right] \quad \text{(Equation 2-8)}$$

The value of Q above can be calculated at the end of the i^{th} injection and designated $Q(i)$. The parameter of interest for comparison with experiment, however, is the change in heat content from the completion of the $(i-1)^{\text{th}}$ injection to completion of the i^{th} injection. The expression for Q in Eq. 2-7 only applies to the liquid contained in volume V_0 . Therefore, after completing an injection, it is obvious that a correction must be made for displaced volume (i.e., $\Delta V_i = \text{injection volume}$) since some of the liquid in V_0 after the $(i-1)^{\text{th}}$ injection will no longer be in V_0 after the i^{th} injection, even though it will contribute to the heat effect (assuming the kinetics of reaction and mixing are fast) before it passes out of the working volume V_0 . The liquid in the displaced volume contributes about 50% as much heat effect as an equivalent volume remaining in V_0 . The correct expression for the heat released $\Delta Q(i)$, from the i^{th} injection is

$$\Delta Q(i) = Q(i) + \frac{dV_i}{V_0} \left[\frac{Q(i) + Q(i-1)}{2} \right] - Q(i-1) \quad \text{(Equation 2-9)}$$

By dividing $\Delta Q(i)$ with moles in the i^{th} injected volume, the normalized heat, $\Delta Q(i)$ is obtained, which is described by three parameters n , ΔH , and K .

2.4.4.2. The fitting of the present research

In the current fitting model, the total generated heat can be separated by two kinds of heat $Q_1(i)$ and $Q_2(i)$, which are generated according to Eq. 2-1, and Eq. 2-2, respectively.

$$Q_1(i) = \frac{n_1 M_{t1} \Delta H_1 V_0}{2} \left[I + \frac{X_{t1}}{n_1 M_{t1}} + \frac{I}{n_1 K_1 M_{t1}} - \sqrt{\left(I + \frac{X_{t1}}{n_1 M_{t1}} + \frac{I}{n_1 K_1 M_{t1}} \right)^2 - \frac{4X_{t1}}{n_1 M_{t1}}} \right]$$

$$Q_2(i) = \frac{n_2 M_{t2} \Delta H_2 V_0}{2} \left[I + \frac{X_{t2}}{n_2 M_{t2}} + \frac{I}{n_2 K_2 M_{t2}} - \sqrt{\left(I + \frac{X_{t2}}{n_2 M_{t2}} + \frac{I}{n_2 K_2 M_{t2}} \right)^2 - \frac{4X_{t2}}{n_2 M_{t2}}} \right]$$

Where,

ΔH_1 = Enthalpy change at the initial binding stage;

K_1 = Binding constant between I_3^- and $Me_{18-\alpha}$ -CD;

n_1 = The number of binding sites in $Me_{18-\alpha}$ -CD;

V_o = Cell volume;

M_{11} = The total concentration of Me₁₈- α -CD in V_o ;

X_{11} = The total concentration of I₃⁻;

$Q_1(i)$: The total released heat until the i^{th} injection in the initial stage (Eq. 1).

Similarly, the symbols in the second binding stage can be defined as:

ΔH_2 = The enthalpy change at the second binding stage

K_2 = Equilibrium constant between I₃⁻ and I₃⁻-Me₁₈- α -CD

N_2 = The number of the binding sites in I₃⁻-Me₁₈- α -CD

V_o = Cell volume

M_{12} = The total concentration of I₃⁻-Me₁₈- α -CD in V_o , which equals to $X_{11}[\Delta Q_1/(i\Delta H_1)]$

X_{12} = The total concentration of I₃⁻, which equals to $X_{11}[1-\Delta Q_1/(i\Delta H_1)]$

$Q_2(i)$: The total released heat until the i^{th} injection in the second stage (Eq. 2).

Then, the experimental ITC curve can be fitted by $\Delta Q = \Delta Q(i)_1 + \Delta Q(i)_2$, where $\Delta Q(i)_1$ and $\Delta Q(i)_2$ are the released heat for i^{th} titration in the initial and second stages, respectively.

The result in the thermodynamic parameters ΔH_1 , K_1 , ΔH_2 , and K_2 . Are shown in Table S3. ΔS_1 and ΔS_2 were obtained by van't Hoff equation.

2.4.5. UV-vis spectroscopy

UV-vis spectra were recorded by UV-vis spectrometer (V670, JASCO, Japan) in the wavelength range between 200 to 600 nm, with a resolution of 0.5 nm and a fixed slit width of 0.5 nm. 0.2 mm path length quartz cuvettes were used.

2.4.6. Raman spectroscopy

Raman spectra were recorded on a micro-Raman spectrometer (Jasco NRS 3100KK) equipped with

YAG laser (power 1.5 mW, Wavelength 532 nm) and a thermoelectrically cooled CCD detector (DU401-BV-120, Andor). All the measurements were performed at ambient temperature.

Reference

- 1 K. Biswas, J. He, I. D. Blum, C.-I. Wu, T. P. Hogan, D. N. Seidman, V. P. Dravid and M. G. Kanatzidis, *Nature*, 2012, **489**, 414-418.
- 2 L. M. Goncalves, P. Alpuim and J. H. Correia, *J. Electron. Mater.*, 2010, **39**, 1516-1521.
- 3 A. R. M. Siddique, S. Mahmud and B. Van Heyst, *Renew. Sustain. Energy Rev.*, 2017, **73**, 730-744.
- 4 T. G. W. Harman T C, Walsh M P, Laforge B E, *J. Electron. Mater.*, 2012, **34**, L19-L22.
- 5 G. Jeffrey Snyder and eric S. Toberer, *Nat. Mater.*, 2008, **7**, 105-114.
- 6 T. I. Quickenden; Y. Mua, *J. Electrochem. Soc.*, 1995, **142**, 3985-3994.
- 7 A. Gunawan, C. H. Lin, D. A. Buttry, V. Mujica, R. A. Taylor, R. S. Prasher and P. E. Phelan, *Nanoscale Microscale Thermophys. Eng.*, 2013, **17**, 304-323.
- 8 L. Zhang, T. Kim, N. Li, T. J. Kang, J. Chen, J. M. Pringle, M. Zhang, A. H. Kazim, S. Fang, C. Haines, D. Al-Masri, B. A. Cola, J. M. Razal, J. Di, S. Beirne, D. R. MacFarlane, A. Gonzalez-Martin, S. Mathew, Y. H. Kim, G. Wallace and R. H. Baughman, *Adv. Mater.*, 2017, **29**, 1605652.
- 9 Q. T. I. Mua Y, *J. Electrochem. Soc.*, 1996, **143**, 2558-2564.
- 10 T. I. Quickenden and C. F. Vernon, *Sol. Energy*, 1986, **36**, 63-72.
- 11 M. F. Dupont, D. R. MacFarlane and J. M. Pringle, *Chem. Commun.*, 2017, **53**, 6288-6302.
- 12 R. Hu, B. A. Cola, N. Haram, J. N. Barisci, S. Lee, S. Stoughton, G. Wallace, C. Too, M. Thomas, A. Gestos, M. E. Dela Cruz, J. P. Ferraris, A. A. Zakhidov and R. H. Baughman, *Nano Lett.*, 2010, **10**, 838-846.
- 13 H. Im, T. Kim, H. Song, J. Choi, J. S. Park, R. Ovalle-Robles, H. D. Yang, K. D. Kihm, R. H. Baughman, H. H. Lee, T. J. Kang and Y. H. Kim, *Nat. Commun.*, 2016, **7**, 10600.
- 14 M. S. Romano, N. Li, D. Antiohos, J. M. Razal, A. Nattestad, S. Beirne, S. Fang, Y. Chen, R. Jalili, G. Wallace, R. Baughman and J. Chen, *Adv. Mater.*, 2013, **25**, 6602-6606.
- 15 T. J. Abraham, D. R. MacFarlane and J. M. Pringle, *Energy Environ. Sci.*, 2013, **6**, 2639-2645.
- 16 T. J. Abraham, D. R. MacFarlane and J. M. Pringle, *Chem. Commun. (Camb.)*, 2011, **47**, 6260-6262.
- 17 T. Kim, J. S. Lee, G. Lee, H. Yoon, J. Yoon, T. J. Kang and Y. H. Kim, *Nano Energy*, 2017, **31**, 160-167.
- 18 Z. Liu, A. Samanta, J. Lei, J. Sun, Y. Wang and J. F. Stoddart, *J. Am. Chem. Soc.*, 2016, **138**, 11643-11653.
- 19 F. Harata, K., Uekama, K., Otagiri, M., Hirayama, *Bull. Chem. Soc. Jpn.*, 1987, **60**, 497-502.
- 20 H. Zhou, T. Yamada and N. Kimizuka, *J. Am. Chem. Soc.*, 2016, **138**, 10502-10507.
- 21 H. Zhou, T. Yamada and N. Kimizuka, *Sustain. Energy Fuels*, 2018, **2**, 472-478.
- 22 J. Nour, E. M.; Chen L. H.; Laane, *J. Phys. Chem.*, 1986, **90**, 2841-2846.
- 23 E. E. Havinga and E. H. Wiebenga, *Acta Crystallogr.*, 1958, **11**, 733-737.
- 24 R. J. Hach and R. E. Rundle, *J. Am. Chem. Soc.*, 1951, **73**, 4321-4324.
- 25 F. H. Herbstein and M. Kapon, *Nat. Phys. Sci.*, 1972, **239**, 153-154.
- 26 S. Kitamura, K. Nakatani, T. Takaha and S. Okada, *Macromol. Rapid Commun.*, 1999, **20**, 612-615.
- 27 J. L. Pursell and C. J. Pursell, 2016, **120**, 2144-2149.

- 28 J. W. Minns and A. Khan, *J. Phys. Chem. A*, 2002, **106**, 6421–6425.
- 29 W. Kim, Y. Yamasaki and K. Kataoka, *J. Phys. Chem. B*, 2006, **110**, 10919–10925.
- 30 S. V. Kireev and S. L. Shnyrev, *Laser Phys.*, 2015, **25**, 75602.
- 31 L. M. Yong-ju W, Cui-ge L, *Spectrosc. Spectr. Anal.*, 2005, **25**, 86.
- 32 Y. Bichsel and U. Von Gunten, *Anal. Chem.*, 1999, **71**, 34–38.
- 33 D. A. Palmer, R. W. Ramette and R. E. Mesmer, *J. Solution Chem.*, 1984, **13**, 673–683.
- 34 R. C. Troy, M. D. Kelley, J. C. Nagy and D. W. Margerum, *Inorg. Chem.*, 1991, **30**, 4838–4845.
- 35 I. Lengyel, I. R. Epstein and K. Kusth, *Inorg. Chem.*, 1993, **32**, 5880–5882.
- 36 J. W. Minns and A. Khan, *J. Phys. Chem. A*, 2002, **106**, 6421–6425.
- 37 V. Calabrese and A. Khan, *J. Phys. Chem. A*, 2000, **104**, 1287–1292.
- 38 D. L. Mould, *Biochem. J.*, 1954, **58**, 593–600.
- 39 R. S. Mulliken, *J. Am. Chem. Soc.*, 1950, **72**, 600–608.
- 40 R. P. Lang, *J. Am. Chem. Soc.*, 1962, **84**, 1185–1191.
- 41 K. H. Kim, H. Ki, J. H. Lee, S. Park, Q. Kong, J. Kim, J. Kim, M. Wulff and H. Ihee, *Phys. Chem. Chem. Phys.*, 2015, **17**, 8633–8637.
- 42 C. Reichardt, *Chem. Rev.*, 1994, **94**, 2319–2358.
- 43 P. H. Svensson and L. Kloo, *Chem. Rev.*, 2003, **103**, 1649–1684.
- 44 H. Kim, *Biopolym. Orig. Res. Biomol.*, 1982, **21**, 2083–2096.
- 45 W. Saenger, *Naturwissenschaften*, 1984, **71**, 31.
- 46 B. K. H. Wiebenga E H, Havinga E E, *Advances inorganic Chem. Radiochem.*, 1961, **3**, 133–169.
- 47 I. H. Mizuno, Masagi, Jiro Tanaka, *J. Phys. Chem.*, 1981, **85**, 1789–1794.
- 48 W. S. M. Noltemeyer, *Nature*, 1976, **259**, 629–632.
- 49 Paul Job, *Ann. di Chim. Appl.*, 1928, **9**, 113.
- 50 L. I. Katzin and E. Gebert, *J. Am. Chem. Soc.*, 1955, **77**, 5814–5819.
- 51 F. C. Kracek, *J. Phys. Chem.*, 1931, **35**, 417–422.
- 52 D. Diaz, I. Vargas-Baca and J. Gracia-Mora, *J. Chem. Educ.*, 1994, **71**, 708–714.
- 53 L. Martin, S. Yang, A. C. Brooks, P. N. Horton, L. Male, O. Moulfi, L. Harmand, P. Day, W. Clegg and W. Harrington, *CrystEngComm*, 2015, **17**, 7354–7362.
- 54 C. A. L. Filgueiras, H. Jr and M. S. Skakle, *Acta Crystallogr. Sect. E Struct. Reports Online*, 2001, **57**, 0338-0340.
- 55 A. J. Blake, F. A. Devillanova, R. O. Gould, W. Li, S. Parsons and M. Schr, *Chem. Soc. Rev.*, 1998, **27**, 195–205.
- 56 L. Kloo, H. Svensson and M. J. Taylor, *J. Chem. Soc. Dalt. Trans.*, 2000, **7**, 1061–1065.
- 57 P. Deplano, J. R. Ferraro, M. L. Mercuri and E. F. Trogu, *Coord. Chem. Rev.*, 1999, **188**, 71–95.
- 58 P. H. Svensson and L. Kloo, , DOI:10.1021/cr0204101.
- 59 L. A. Bengtsson, H. Stegemann, B. Holmberg and H. Füllbier, *Mol. Phys.*, 1991, **73**, 283–296.
- 60 F. Bigoli, P. Deplano, A. Ienco, C. Mealli, M. L. Mercuri, M. A. Pellinghelli, G. Pintus, G. Saba and E. F. Trogu, *Inorg Chem*, 1999, **38**, 4626–4636.
- 61 P. Deplano, F. A. Devillanova, J. R. Ferraro, M. L. Mercuri, V. Lippolis and E. F. Trogu, *Appl.*

- Spectrosc.*, 1994, **48**, 1236–1241.
- 62 P. H. Svensson and L. Kloo, *J. Chem. Soc. Dalt. Trans.*, 2000, **951**, 2449–2455.
- 63 E. M. Nour, L. H. Chen and J. Laane, 1986, **77843**, 2841–2846.
- 64 J. S. Zambounis, E. I. Kamitsos, A. P. Patsis and G. C. Papavassiliou, *J. Raman Spectrosc.*, 1992, **23**, 81–85.
- 65 E. Freire, L. Obdulio and M. Straume, *Anal. Chem.*, 1990, **62**, 950A-959A.

Chapter 3 A theoretical basis for the enhancement of Seebeck Coefficients in Supramolecular Thermocells

Abstract: Seebeck coefficients (S_e) of supramolecular thermocells harnessing four kinds of cyclodextrins as host molecules were investigated. The theoretical analysis revealed that association enthalpy between the hosts and triiodide has a major influence on the Seebeck coefficients of the thermocells. Thermodynamic parameters of host-guest associations were evaluated by isothermal titration calorimetry, which is in good agreement with the theoretically estimated values from thermocell measurements. This result provides a guideline to estimate the Seebeck coefficient of supramolecular thermocells and to determine the thermodynamic parameters.

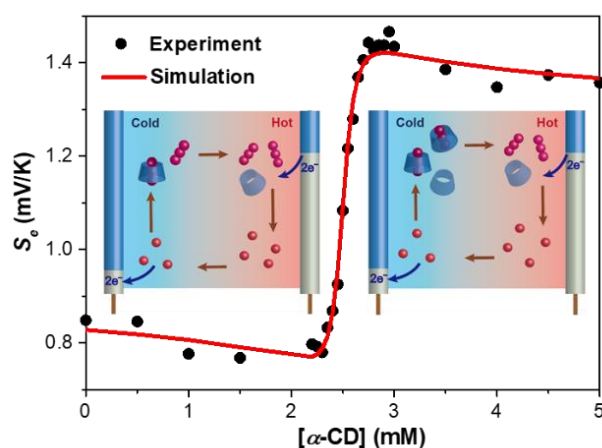


Figure 3-1. The Seebeck coefficient enhancement based on the increased concentration of host molecules, which reflects the controlled concentration gap of redox species.

3.1. Introduction

Thermoelectric conversion is one of the promising methods for waste energy usage.¹⁻⁵ Solid thermoelectric semiconductors have been the main focus of the thermoelectric devices because of their high conversion efficiency.⁶⁻⁸ Meanwhile, thermocells or thermo-electrochemical cells have recently attracted increasing interest because they generate an electromotive force (Seebeck coefficient, S_e) that is one order higher than those reported for commercial semiconductors.^{9,10} A high S_e is essential for

harvesting sufficient quantity of electric power from a small temperature difference. The thermoelectric power of the thermocells is derived from the temperature dependency of the difference in chemical potentials in electrolyte solutions, which was first discussed by Richards in the late 19th century.^{11,12} This simple mechanism allows us to utilize a variety of redox-active species as the components of thermocells, and the studies on thermocell have been rekindled by Burrow,² Quickenden,^{13,14} and Ikeshoji¹⁵ et al. since the 1980s. They discovered that a redox couple of hexacyanoferrate(II/III) exhibits a high S_e of -1.4 mV/K and high stability in aqueous media, which serves as a benchmark of thermocells nowadays.¹⁶⁻¹⁸ Recently, Zhou and coworkers reported surprisingly high S_e of -4.2 mV K⁻¹ by addition of guanidinium into the hexacyanoferrate(II/III) thermocell.¹⁹ In recent years, Pringle and co-workers discovered a new redox couple tris(bipyridyl)cobalt(II/III), which showed a high S_e up to 2.2 mV/K.^{20,21} Pringle, Weaver and Y.H. Kim²²⁻²⁴ showed the influence of solvents on the Seebeck coefficients of thermocells, and optimization of the redox couples, solvents and electrodes contribute to the improvement of the Seebeck coefficient. Thanks to their efforts, thermoelectric conversion efficiency reached 3.95% compared to Carnot efficiency. However, further improvement of the performance is required to maximize the potential of thermocells and find their wide applications.

We have recently proposed a novel strategy for improving the Seebeck coefficient by introducing host-guest chemistry.²⁵⁻²⁹ α -cyclodextrin (α -CD) selectively binds triiodide ion (I_3^-) at a lower temperature while it is released by elevating the temperature. The selective capture and elimination of the oxidant resulted in the difference in the I_3^- concentration between two electrodes which generates an additional voltage according to the Nernst Equation (Fig. 3-1). By introducing host-guest interactions to the thermocell, the Seebeck coefficient was enhanced by 0.6 mV/K.

This principle of the supramolecular thermocell is related to that of concentration cells,³⁰ and it could also be described as thermal concentration cells. Although selective molecular recognition holds promise to a wide range of applications, it has been difficult to generate energy. In supramolecular thermocells, electric energy is created based on the temperature-dependent host-guest interactions,

which is the key to improving the performance. It provided a first example of the heat-to-electric energy conversion based on supramolecular chemistry.

In this study, we provide a theoretical basis that relates host–guest reactions to electromotive force. Thermocell measurements were investigated for the redox-couple of iodide (I^-)/ I_3^- in the presence of various cyclodextrins (CDs). The experimental data were compared with theoretically-estimated ΔH , ΔS and the binding constant of the inclusion reactions from S_e at varied host concentrations. A novel host, Me_{12} - α -CD, was also investigated which showed higher S_e as compared to α -CD. This result will provide a rational strategy for the enhancement of the Seebeck coefficient.

3.2. Results and Discussion

3.2.1. Thermodynamics for complexation of I_3^- with CDs

In a conventional I^-/I_3^- thermocell, reduction of I_3^- to three equivalents of I^- (Eq. 3-1) preferably occurs at the high-temperature side of the thermocell because this reaction gains entropy. Conversely, oxidation of I^- (Eq. 3-2) is preferred at the low-temperature side.^{1,31}



In supramolecular thermocells, various host molecules such as cyclodextrins (CDs) are added to capture I_3^- anion. α -, β - and γ -CDs are applied as the host molecules, which are 6-, 7- and 8-membered rings of glucose chains, respectively, as well as Me_{12} - α -CD that is a hexakis-(2,6-di-O-methyl)- α -Cyclodextrin. Their inner cavities show hydrophobic nature in an aqueous environment.³² The inclusion phenomena of CDs for hydrophobic guest molecules have been applied in many disciplines including the synthesis of supramolecular interlocked molecules,^{33,34} molecular separations,³⁵ hydrogels,^{36,37} and drug delivery systems.³⁸ α -CD binds one equivalent of hydrophobic I_3^- .³⁹

Although supramolecular thermocells utilize the temperature dependence of the binding constant of these CDs, their thermodynamics has not been fully investigated to date. The binding constant (K), inclusion enthalpy (ΔH) and entropy (ΔS) between I_3^- and CDs were evaluated by isothermal titration

Table 3-1. Binding constant (K), reaction enthalpy (ΔH), and reaction entropy (ΔS) between CDs and I_3^- at various temperatures. K , ΔH , ΔS at 25 °C were also estimated from the results of thermocell measurements. $T\Delta S$ was also shown.

	T (°C)	K ($10^3 M^{-1}$)	ΔH (kcal mol $^{-1}$)	ΔS (cal K $^{-1}$ mol $^{-1}$)	$T\Delta S$ (kcal mol $^{-1}$)
Me ₁₂ - α -CD	10	771 \pm 22	-9.86 \pm 0.05	-27.9 \pm 0.3	-7.9 \pm 0.1
	25	597.5 \pm 1.8	-9.36 \pm 0.01	-26.4 \pm 0.4	-7.8 \pm 0.1
	40	224.1 \pm 0.5	-9.43 \pm 0.02	-24.5 \pm 0.5	-7.7 \pm 0.2
	55	67.1 \pm 0.1	-9.36 \pm 0.02	-22.1 \pm 0.3	-7.3 \pm 0.1
	TEC [#]	1440	-13.13	-15.76	-4.70
α -CD	10	370 \pm 30	-12.02 \pm 0.09	-17.0 \pm 0.5	-4.8 \pm 0.1
	25	160 \pm 20	-11.97 \pm 0.18	-16.4 \pm 0.9	-4.9 \pm 0.3
	40	44 \pm 18	-12.14 \pm 0.10	-17.6 \pm 1.2	-5.5 \pm 0.4
	55	22 \pm 17	-10.21 \pm 0.15	-13.9 \pm 0.9	-4.6 \pm 0.3
	TEC [#]	50.5	-11.97	-12.84	-3.83
β -CD	10	3.4 \pm 0.3	-6.06 \pm 0.14	-5.2 \pm 0.2	-1.5 \pm 0.1
	25	2.6 \pm 0.2	-6.19 \pm 0.17	-5.1 \pm 0.3	-1.5 \pm 0.1
	40	1.91 \pm 0.17	-6.5 \pm 0.3	-5.6 \pm 0.5	-1.8 \pm 0.2
	TEC [#]	3.65	-5.66	-2.7	-0.81
γ -CD	10	0.39 \pm 0.01	-2.81 \pm 0.03	1.93 \pm 0.18	0.55 \pm 0.10
	25	0.27 \pm 0.02	-2.98 \pm 0.03	1.13 \pm 0.12	0.34 \pm 0.04
	40	0.20 \pm 0.01	-2.90 \pm 0.04	1.23 \pm 0.09	0.39 \pm 0.03
	TEC [#]	1.13	-1.83	8.1	2.4

calorimetry (ITC) at various temperatures (Table 3-1, the titration curves are shown in Fig. 3-2, 3-3 and 3-4). For α -CD, the binding constants decreased upon increasing temperatures, while the ΔH and ΔS are less temperature dependent. The association reactions of I_3^- and CDs is exothermic ($\Delta H < 0$) and preferably occurs at a lower temperature. It is to be noted that the ΔS values of the Me₁₂- α -CD, α -

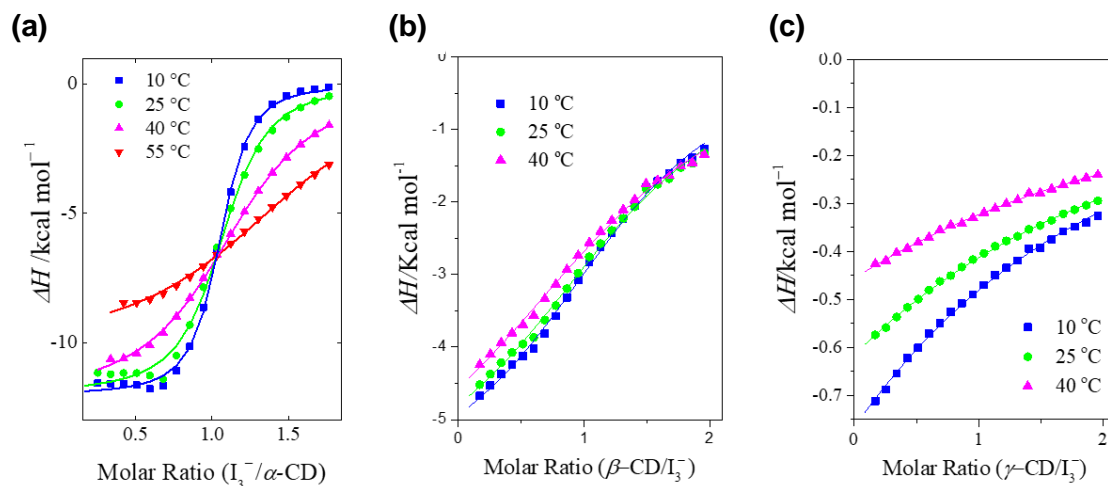


Figure 3-2. Titration curves and the fitting of ITC measurement. (a) α -CD, (b) β -CD, (c) γ -CD.

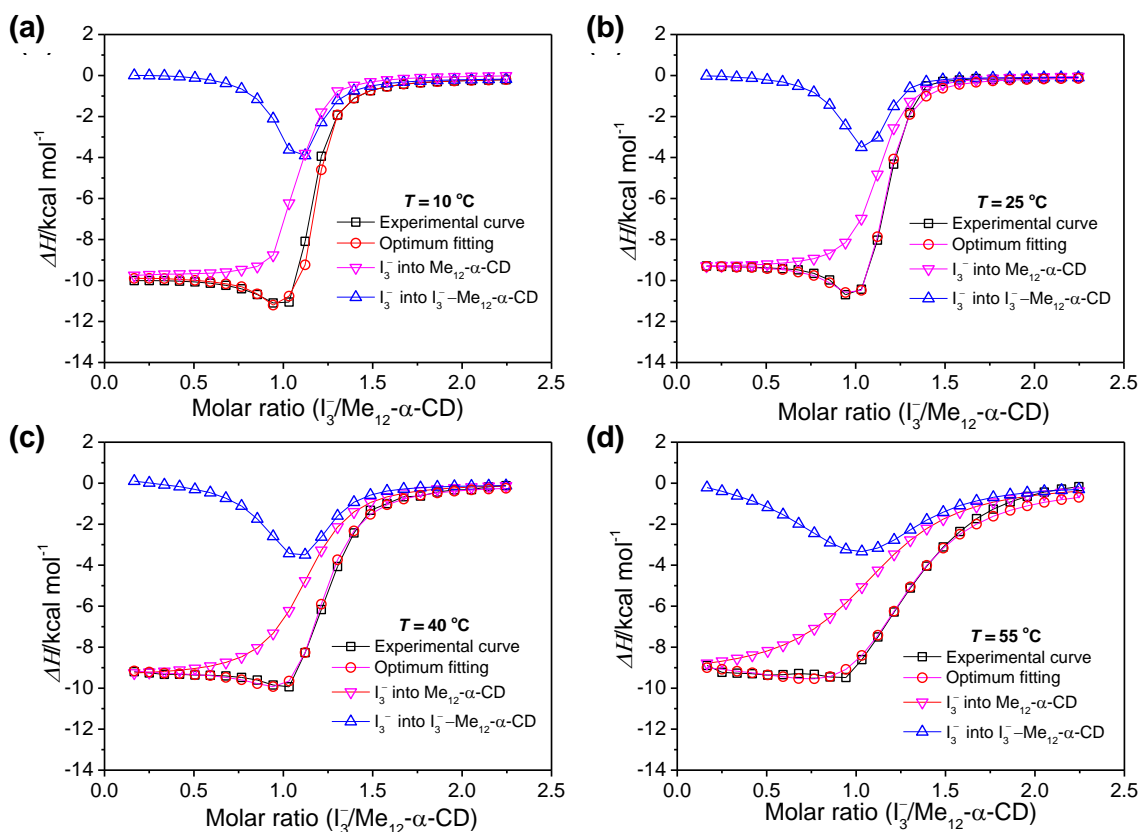


Figure 3-3. The ITC measurements between I_3^- and Me_{12} - α -CD at different temperatures 10, 25, 40 and 55 °C were fitted by the two binding stages model. Experimental curve (black squares), Optimum fitting (red circles), titration of stage 1 (pink triangles), titration of stage 2 (blue triangles), Hypothetical stage 2 (green squares), Where optimum fitting is the sum of the stage 1 and 2.

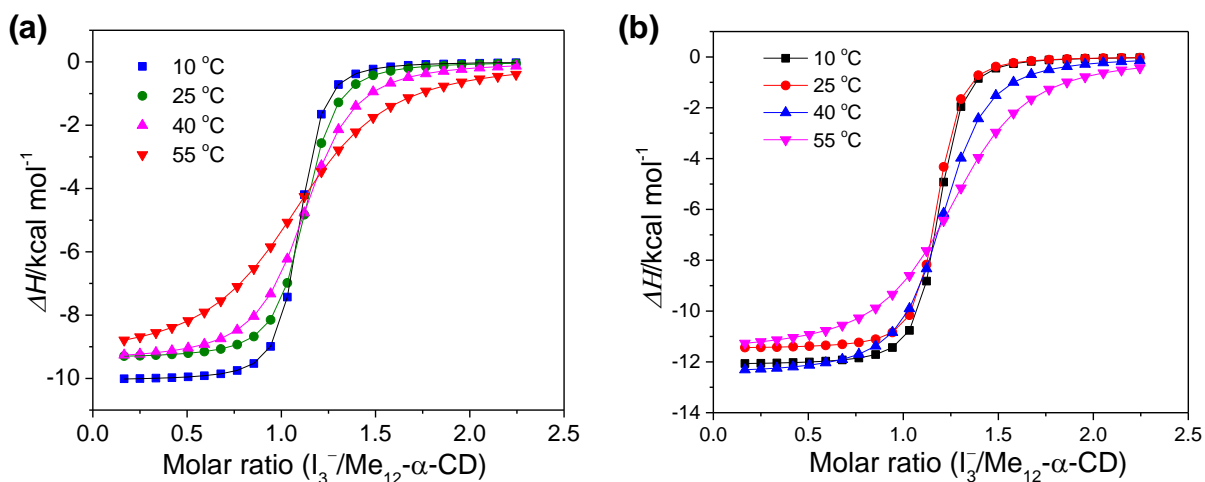


Figure 3-4. The fitting of the binding stage 1 (a) and the hypothetical curves of the binding stage 2 (b).

CD and β -CD are negative, which can be attributed to the loss of transition and rotational freedom of both guest and host molecules.⁴⁰ The interaction between the methyl groups of Me₁₂- α -CD and I₃⁻ was confirmed by ¹H NMR spectroscopy as shown in Fig 3-9. The ¹H peak at 3.39 ppm is attributed to that from 6-*O*-methyl groups, which shifts by the addition of I₃⁻, associated with the increase of the shoulder peaks. It indicates that the interaction between them, which could contribute to the change of entropy by the inclusion reaction. On the other hand, fairly positive entropy change can be observed for γ -CD, which is caused by the replacing of binding water to I₃⁻.⁴¹ Therefore, the conformation of I₃⁻ is highly restricted in the cavity of α -CD and Me₁₂- α -CD, while it has a certain freedom in the larger cavity of γ -CD. In the cavity of β -CD, the conformational restriction of I₃⁻ is at the intermediate between α - and γ -species. The association reaction of Me₁₂- α -CD and I₃⁻ contains two stages, which is similar to the previous report for Me₁₈- α -CD,²⁸ and the thermodynamic parameters of first and second association step are presented in Table 3-1 and Table 3-2 respectively.

Table S2. Parameters for the second binding stage

$\text{Me}_{12}\text{-}\alpha\text{-CD-I}_3^- + \text{I}_3^- \rightarrow \text{Me}_{12}\text{-}\alpha\text{-CD-I}_5^- + \text{I}^-$				
	10 °C	25 °C	40 °C	55 °C
ΔH (kcal mol ⁻¹)	-12.1 ± 0.3	-11.47 ± 0.17	-12.5 ± 0.2	-11.6 ± 0.4
ΔS (cal K ⁻¹ mol ⁻¹)	-14.99	-27.81	-25.05	-41.64
$K_{as}/10^4$ (M ⁻¹)	116 ± 25	85.1 ± 0.3	30 ± 2	11.1 ± 0.4

3.2.2. Estimation of thermodynamic parameters from the Seebeck coefficients in thermocells

The host-guest reaction decreases the concentration of unbound I_3^- species at the cold side of the thermocell and consequently, the electrochemical potential is generated according to the Nernst Equation. The thermocell measurement was executed at the various temperature differences between both sides of the thermocell (Fig. 3-10). Fig. 3-5 shows the linear increase of the electromotive force (V_{oc}) with increasing the difference in temperature (ΔT). Seebeck coefficient (S_e) is defined as $S_e = V_{oc} / \Delta T$, which was determined from the slope of the plots in Fig. 3-5. The intrinsic S_e of the thermocell without CD is ca. 0.85 mV K^{-1} , which is slightly higher than that in the literature (0.53 mV K^{-1}).¹ The deviation is ascribable to the difference in the initial concentration of KI and I_2 , and different temperature range applied to the thermocell.

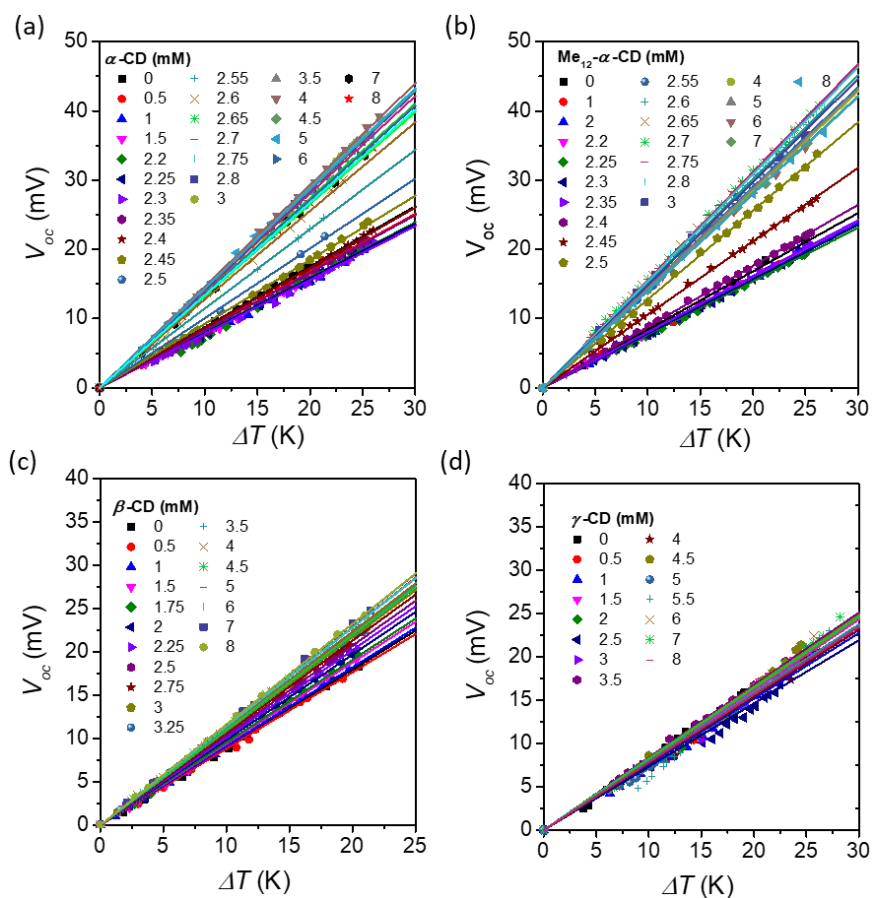


Figure 3-5. Electromotive force of thermocells consisting of I^-/I_3^- and various CDs at various concentrations.

(a) α -CD, (b) Me_{12} - α -CD, (c) β -CD, (d) γ -CD. S_e was estimated from the slope of the plots.

Fig. 3-6 shows the S_e values obtained at varying concentrations of Me₁₂- α -CD, α -, β - and γ -CDs. The S_e values of Me₁₂- α -CD thermocells drastically increased when the concentrations of CDs surpassed the initial concentration of I₂ (2.5 mM). The S_e value in the presence of α -CD is the same as that reported previously.²⁵ A similar curve can be observed for Me₁₂- α -CD, with a slight enhancement of the S_e . The electrolyte contains ca. 2.5 mM of I₃⁻ and the drastic increase of S_e was observed after the addition of equimolar hosts to the guest. The increments of S_e are 0.76, 0.66 and 0.25 mV K⁻¹ for Me₁₂- α -CD, α -CD and β -CD, respectively. The change of S_e was negligible for γ -CD.

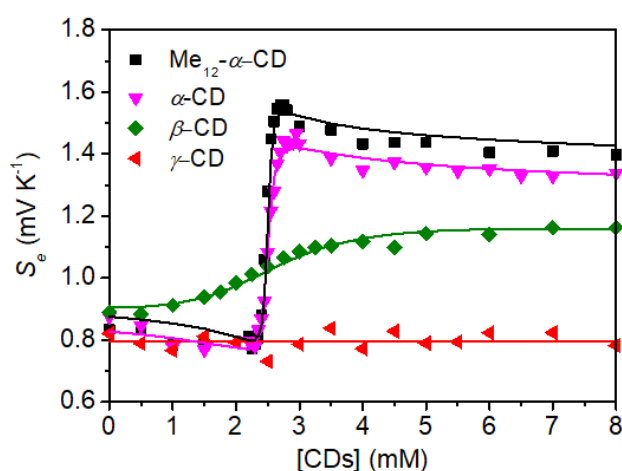


Figure 3-6. Experimental dependence of S_e on the concentration of various hosts. The simulated S_e was shown as solid lines. Initial concentrations of KI and I₂ are 12.5 and 2.5 mM, respectively.

3.2.3. Theoretical analysis of the Seebeck coefficient in TEC

Theoretical analysis of these characteristic changes in S_e values and the influence of host molecular structures are discussed as follows. Upon complexation, CD derivatives mask the redox activity of I₃⁻, while the uncaptured I₃⁻ serves as a redox-active species. The concentration of free I₃⁻ species was estimated from the host-guest equilibrium described as Eq. 3-3.

$$[I_3^-] = \frac{1}{2} \left([I_3^-]_0 - [CD]_0 - K^{-1} + \sqrt{([I_3^-]_0 + [CD]_0 + K^{-1})^2 - 4[I_3^-]_0[CD]_0} \right) \quad (\text{Equation 3-3})$$

The subscript zero in Eq. 3-3 denotes the initial concentration of the corresponding species. The relation between binding constant K and temperature T is given by Eq. 3-4, and the linear relations

between $\log K$ and T^{-1} was confirmed in Fig. 3-7a.

$$\ln K = -\frac{\Delta G^0}{RT} \quad (\text{Equation 3-4})$$

The concentration of uncaptured I_3^- ($[I_3^-]$) was estimated for various concentrations of the hosts, as shown in Fig. 3-7b. The decrease in the concentrations of redox-active I_3^- species is observed upon increasing the relative concentration of CD ($[CD]_0/[I_3^-]_0$). The simulation was carried out at $T = 10$ and 40 °C, respectively. In the cases of Me_{12} - α -CD and α -CD, the differences of $[I_3^-]$ between 10 and 40 °C are significant where the initial concentrations of hosts are higher than that of I_3^- . The changes in concentration are not salient for β - and γ -CD as hosts. (Fig. 3-7b).

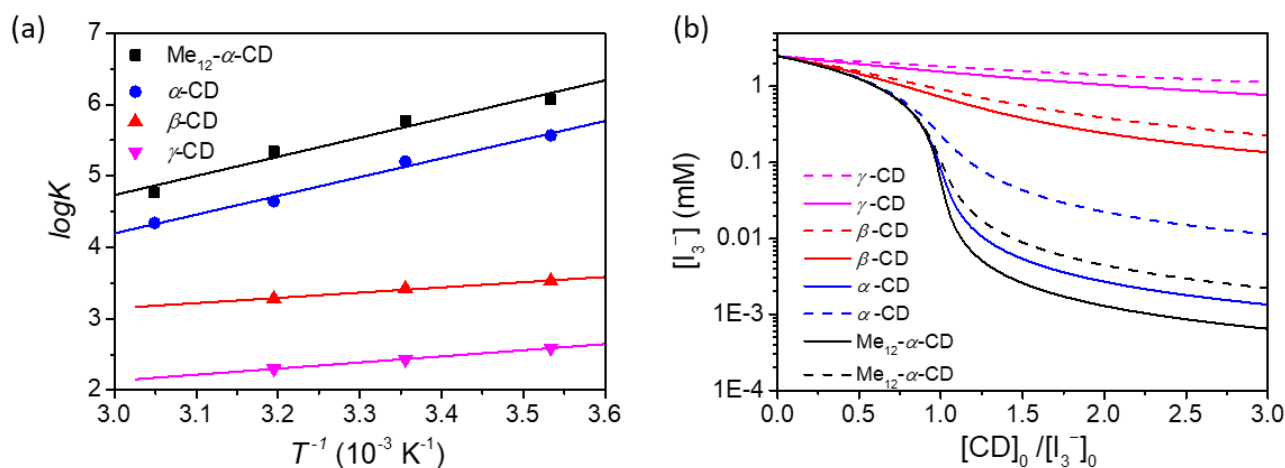


Figure 3-7. (a) Plots of $\log K$ versus T^{-1} for various CDs. (b) The estimated concentration of uncaptured I_3^- between 10 (line) and 40 °C (dash).

The electrochemical potential was estimated from the Nernst Equation (Eq. 3-5)¹², and the concentration of I_3^- was derived from Eq. 3. The Seebeck coefficient of thermocell was obtained by the deriving Eq. 3-4.

$$E = E^0 - \frac{RT}{2F} \ln \frac{[I_3^-]}{[I^-]} \quad (\text{Equation 3-5})$$

$$S_e = \frac{\Delta E_f}{\Delta T} + \frac{\Delta H}{2FT} \times \frac{[CD]_0 - [I_3^-]_0 + K^{-1} - \sqrt{([CD]_0 + [I_3^-]_0 + K^{-1})^2 - 4[CD]_0[I_3^-]_0}}{2\sqrt{([CD]_0 + [I_3^-]_0 + K^{-1})^2 - 4[CD]_0[I_3^-]_0}} + \frac{R}{2F} \times \ln \frac{[CD]_0 - [I_3^-]_0 - K^{-1} + \sqrt{([CD]_0 + [I_3^-]_0 + K^{-1})^2 - 4[CD]_0[I_3^-]_0}}{2} \quad \text{(Equation 3-6)}$$

Where ΔE_f is the difference of formal potential between hot and cold sides, which can be estimated from the intrinsic S_e of the thermocell ($\Delta E_f / \Delta T = 0.62 \text{ mV K}^{-1}$).

The ΔH and K^{-1} were obtained by fitting Eq. 3-6 to Fig. 3-6, and summarized in Table 3-1. The results show that the estimated values of α -CD are in good agreement that obtained from the ITC measurements, thus justifying the theoretical framework. The significant deviation for Me_{12} - α -CD is due to the two binding stages and the formation of Me_{12} - α -CD- I_5^- , the details are described in the ESI. Thus, it is concluded that the enhanced S_e of the thermocells results from the difference in the concentration of electroactive I_3^- species between the hot ($[\text{I}_3^-]_h$) and the cold ($[\text{I}_3^-]_c$) electrode sides. The present method provides the change in entropy, enthalpy and binding constants related to the host-guest interactions by a simple measurement of the generated voltages in between two electrodes which

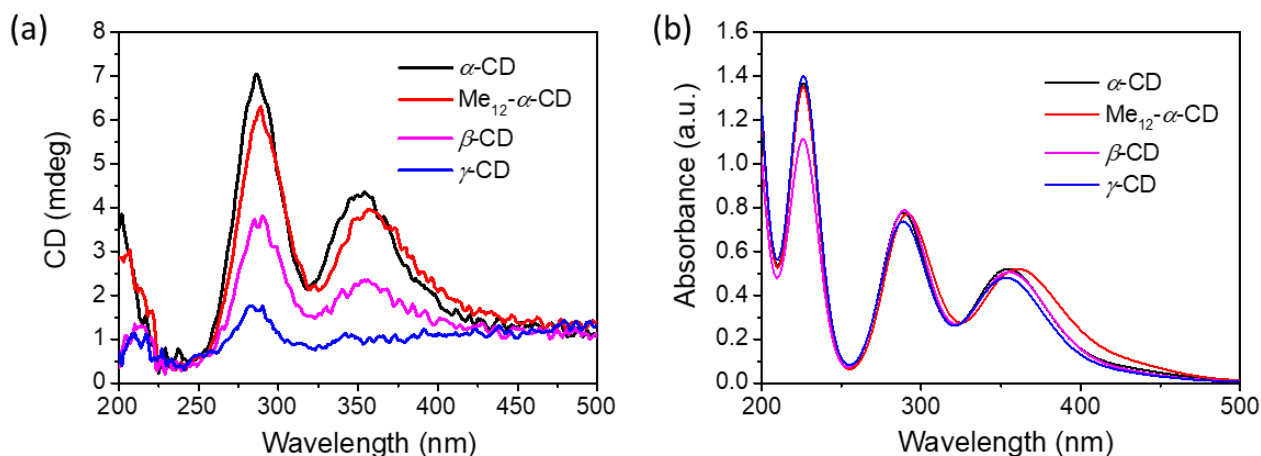


Figure 3-8. (a) Induced circular dichroism (ICD) spectra of I_3^- in the presence of α -, Me_{12} - α -, β - and γ -CDs. (b) The corresponding UV-vis spectra of the solutions in the CD spectroscopic measurement.

are set at different temperatures. The change of S_e by the addition of γ -CD is small, while the association enthalpy could be evaluated by the fitting. Hence, this method is widely applicable to host–

guest combinations with redox active guest molecules. The association of I_3^- was confirmed by the circular dichroism (CD) spectroscopy. As shown in Fig. 3-8, a couple of CD peaks were observed at 286 and 350 nm in the CD spectra of I_3^- and α -, β -, γ -, and Me₁₂- α -CD. These peaks are attributed to I_3^- , and the CD signals were induced by the incorporation by CDs, which provide the chiral environment. A slight red shift of the peaks was observed for Me₁₂- α -CD, as measured by the UV-vis spectroscopic study in our previous paper.⁴² The absence of the peak at 225 nm, which is attributed to that for I^- , indicates that CDs selectively capture I_3^- out of I^- . The weak bands for γ -CD induced spectrum mean the weak binding between γ -CD and I_3^- , which has a good agreement with ITC and thermocell studies.

3.3. Conclusion

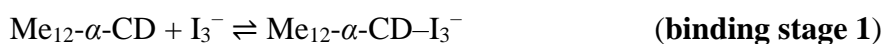
The introduction of temperature-dependent host-guest interactions in thermocells allows to control the concentration of redox-active guest molecules and enhances the S_e . It is found that Me₁₂- α -CD showed higher temperature dependence against the inclusion phenomena, raising the S_e to a higher value. This new approach to empower thermocell will be potentially applicable to other redox couples such as iron- or cobalt complexes, whose intrinsic S_e is higher than the I^-/I_3^- couple. Supramolecular chemistry, therefore, will provide a clue to innovate thermocells.

3.4. Experimental

3.4.1. Isothermal titration calorimetry.

The fitting of the titrations between α -CD, β -CD or γ -CD and I_3^- were carried out by Origin (ver.5 SR2, Micro cal. Inc) and iterated until the χ^2 value reached the minimum. The titration between I_3^- and Me_{12} - α -CD was fitted by a previously reported model.²⁸

According to the previously reported method, the host-guest interaction between Me_{12} - α -CD and I_3^- including two binding stages as follows,



3.4.2. NMR Spectroscopy

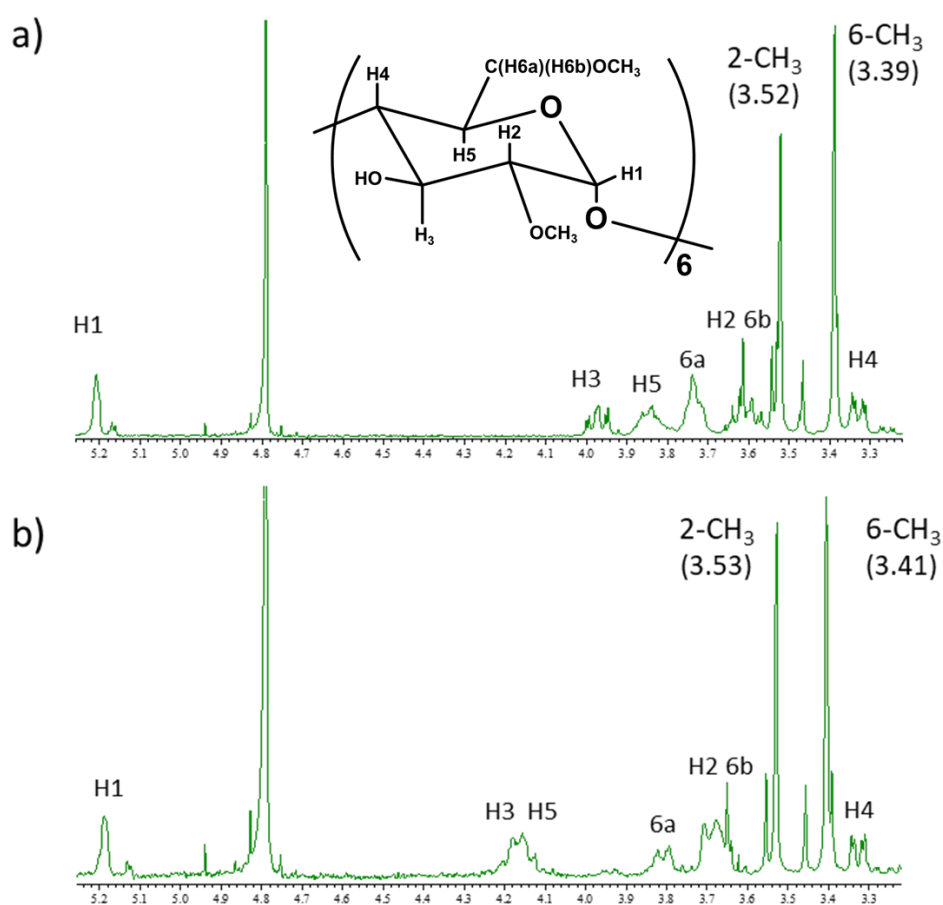


Figure 3-9. 400 MHz ¹H-NMR spectrum of (a) Me_{12} - α -CD (3mM) (b) Me_{12} - α -CD (3mM), I_2 (2.5 mM) and KI (12.5 mM) in 700 μ L of D_2O .

3.4.3. Seebeck coefficient measurement

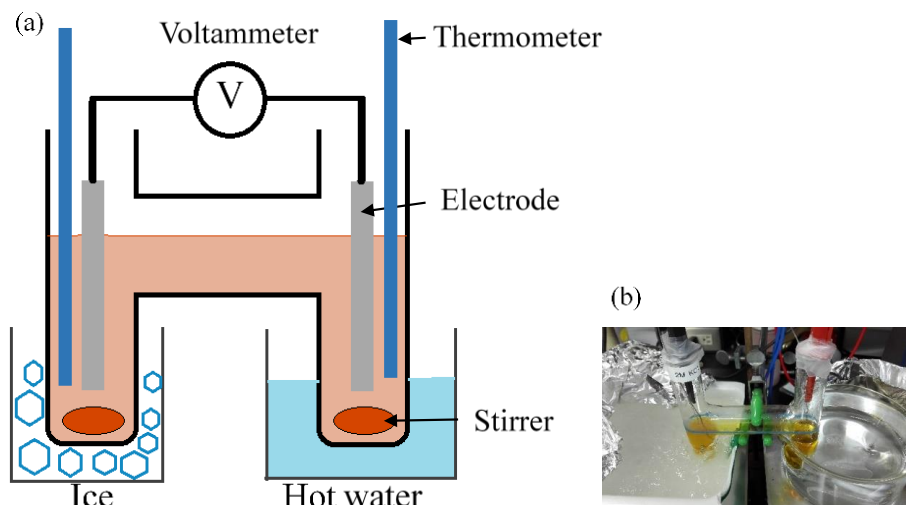


Figure 3-10. (a) A schematic illustration of the TEC. (b) A photograph of the TEC.

3.4.4. Theoretical analysis on the Seebeck coefficient of TEC

3.4.4.1. Seebeck coefficient and reaction entropy.

Seebeck coefficient is the temperature derivative of the redox potential (dE/dT), and Weaver pointed out that the reaction entropy (ΔS_{rc}) during redox reaction is related to the dE/dT as: ²³

$$S_e = \frac{dE}{dT} = \frac{\Delta S_{rc}}{nF} \quad \text{(Equation 3-7)}$$

where n is number of electrons in the redox reaction and F is Faraday's constant. Weaver evaluated ΔS_{rc} of various redox couples in water and non-aqueous solvent. He also used Born's model to calculate the ΔS_{rc} as:

$$\Delta S_{rc} = - \frac{e^2 N}{2\epsilon T} \frac{d \ln \epsilon}{d \ln T} \left(\frac{Z_{ox}^2}{r_{ox}} - \frac{Z_{red}^2}{r_{red}} \right) \quad \text{(Equation 3-8)}$$

where ϵ is the dielectric constant of the solvent, Z_{ox} and Z_{red} are the valence charges of the oxidant and reductant, respectively, r_{ox} and r_{red} are the corresponding radii, e is the electronic charge and N is Avogadro's constant. According to Weaver's theory, redox ions with high valence and small radius most likely result in high reaction entropy and high Seebeck coefficient. Although the ΔS_{rc} evaluated from the experimental results of dE/dT and Eq. S1 have a linear relationship with theoretical values of $(Z_{ox}^2/r_{ox} - Z_{red}^2/r_{red})$, the empirical ΔS_{rc} does not fit with the theoretical one. He concluded that, in

addition to Born's model, the coordination of the solvent molecule around ions and the spin transition between redox could influence the ΔS_{rc} .²³

3.4.4.2. Seebeck coefficient and the concentration of redox couple.

In order to derive the relationship between concentration of the redox couple and Seebeck coefficient, we use Nernst formula to express the equilibrium potential of TEC.¹² When a redox reaction reaches an equilibrium $Ox + ne^- \rightleftharpoons Red$, the equilibrium potential can be expressed with the concentration of oxidized specie ([Ox]) and reduced specie ([Red]):

$$E = E_f + \frac{RT}{nF} \ln \frac{[Ox]}{[Red]^n} \quad (\text{Equation 3-9})$$

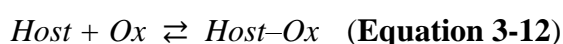
$$E_f = E^0 + \frac{RT}{nF} \ln \frac{\gamma_{ox}}{\gamma_{red}} \quad (\text{Equation 3-10})$$

In Eq. 3-9 and 3-10, R is the standard gas constant, E_f is formal potential, E^0 is the standard potential, γ_{ox} and γ_{red} are the activity coefficient of oxidized and reduced species, respectively. Debye–Hückel theory⁴³ describes that γ is also related to Z^2 , r and ε , which appear in Eq. 3-8. Seebeck coefficient (S_e) is a deviation of voltage by temperature, and when ΔT is small enough to regard ΔE as proportional to ΔT , it can be written as:

$$S_e = \frac{\Delta E}{\Delta T} = \frac{\Delta E_f}{\Delta T} + \frac{R}{nF} \ln \frac{[Ox]}{[Red]^n} + \frac{RT}{nF} \frac{\Delta(\ln \frac{[Ox]}{[Red]^n})}{\Delta T} \quad (\text{Equation 3-11})$$

3.4.4.3. Calculations of Seebeck coefficient of [Red] / [Ox] with [Host]

When a host is added into the TEC, host–guest interaction between Host and either oxidized or reduced form occur. When oxidized form is selectively bind to the host, after the system reaches an equilibrium below;



the binding constant and the initial concentration of host and Ox are expressed below:

$$K = [Host-Ox]/[Ox][Host] \quad (\text{Equation 3-13a})$$

$$[Host]_0 = [Host] + [Host-Ox] \quad (\text{Equation 3-13b})$$

$$[Ox]_0 = [Ox] + [Host-Ox] \quad (\text{Equation 3-13c})$$

By solving equation (Eq. 3-13a) to (Eq. 3-13c), the concentration of electroactive oxidized form at temperature T can be obtained as follows.

$$[Ox] = \frac{1}{2}([Ox]_0 - [Host]_0 - K^{-1} + \sqrt{([Ox]_0 - [Host]_0 + K^{-1})^2 - 4[Ox]_0[Host]_0})$$

$$(\text{Equation 3-14}).$$

The concentration of the oxidized form changes with temperature change after the introduction of supramolecular interaction. While that of reduced form is constant. Then (Eq. 3-11) is expressed as:

$$S_e = \frac{\Delta E_f}{\Delta T} + \frac{RT}{nF} \times \frac{\Delta \ln[Ox]}{\Delta[Ox]} \times \frac{\Delta[Ox]}{\Delta(K^{-1})} \times \frac{\Delta(K^{-1})}{\Delta T} + \frac{R}{nF} \ln[Ox] \quad (\text{Equation 3-15})$$

In Eq. 3-15,

$$\frac{\Delta \ln[Ox]}{\Delta[Ox]} = \frac{1}{[Ox]} \quad (\text{Equation 3-16a})$$

$$\frac{\Delta(K^{-1})}{\Delta T} = -\frac{K^{-1}\Delta H}{RT^2} \quad (\text{Equation 3-16b})$$

$$\frac{\Delta[Ox]}{\Delta K^{-1}} = \frac{1}{2} \left(\frac{[Host]_0 + [Ox]_0 + K^{-1} - \sqrt{Q}}{\sqrt{Q}} \right) \quad (\text{Equation 3-16c})$$

Where

$$\sqrt{Q} = \sqrt{([Ox]_0 - [Host]_0 + K^{-1})^2 - 4[Ox]_0[Host]_0}$$

By substituting Eq. S10-a to c, Eq. S9 can be written as :

$$S_e = \frac{\Delta E_f}{\Delta T} + \frac{\Delta H}{nFT} \times \frac{[Host]_0 - [Ox]_0 + K^{-1} - \sqrt{Q}}{2\sqrt{Q}} + \frac{R}{nF} \times \ln \frac{[Host]_0 - [Ox]_0 - K^{-1} + \sqrt{Q}}{2} \quad (\text{Equation 3-17})$$

Thus Seebeck coefficient can be estimated by the initial concentrations of the host, redox-active species, binding constant, and binding enthalpy.

Eq. 3-17 has a peak where $[Ox]_0 = [Host]_0 - K^{-1}$. In that case, the Seebeck coefficient become maximum at

$$S_e = -\frac{\Delta H}{2nFT} + \frac{R}{nF} \times \ln(\sqrt{[Host]_0([Host]_0 - K^{-1})} - K^{-1}) \quad (\text{Equation 3-18})$$

Reference

- 1 T. J. Abraham, D. R. MacFarlane and J. M. Pringle, *Chem. Commun. (Camb)*., 2011, **47**, 6260–6262.
- 2 B. Burrows, *J. Electrochem. Soc.*, 1976, **123**, 154–159.
- 3 H. L. Chum, R. A. Osteryoung, *Rep. SERI/TR- 332416*, **1980**, 1.
- 4 T. I. Quickenden; Y. Mua, *J. Electrochem. Soc.*, 1995, **142**, 3985-3994.
- 5 S. W. Lee, Y. Yang, H.-W. Lee, H. Ghasemi, D. Kraemer, G. Chen and Y. Cui, *Nat. Commun.*, 2014, **5**, 3942.
- 6 T. M. Tritt, *Science* 1999, **283**, 804–805.
- 7 F. J. Disalvo, *Science* 1999, **285**, 703–706.
- 8 G. J. Snyder and E. S. Toberer, *Nat. Mater.*, 2008, **7**, 105–114.
- 9 B. Poudel, Q. Hao, Y. Ma, Y. Lan, A. Minnich, B. Yu, X. Yan, D. Wang, A. Muto, D. Vashaee, X. Chen, J. Liu, M. Dresselhaus, G. Chen and Z. Ren, *Science* 2008, **320**, 634–638.
- 10 K. Biswas, J. He, I. D. Blum, C.-I. Wu, T. P. Hogan, D. N. Seidman, V. P. Dravid and M. G. Kanatzidis, *Nature*, 2012, **489**, 414-418.
- 11 T. W. Richards, *Zeitschrift fur Phys. Chemie*, 1897, **24**, 39–54.
- 12 K. G. Y. Kuzminskii Y V, Zasukha V A, *J. Power Sources*, 1994, **52**, 231–242.
- 13 T. I. Quickenden and C. F. Vernon, *Sol. Energy*, 1986, **36**, 63–72.
- 14 Q. T. I. Mua Y, *J. Electrochem. Soc.*, 1996, **143**, 2558.
- 15 T. Ikeshoji, *Bull. Chem. Soc. Japan*, 1987, **60**, 1505–1514.
- 16 R. Hu, B. A. Cola, N. Haram, J. N. Barisci, S. Lee, S. Stoughton, G. Wallace, C. Too, M. Thomas, A. Gestos, M. E. Dela Cruz, J. P. Ferraris, A. A. Zakhidov and R. H. Baughman, *Nano Lett.*, 2010, **10**, 838–846.
- 17 T. J. Kang, S. Fang, M. E. Kozlov, C. S. Haines, N. Li, Y. H. Kim, Y. Chen and R. H. Baughman, *Adv. Funct. Mater.*, 2012, **22**, 477–489.
- 18 H. Im, T. Kim, H. Song, J. Choi, J. S. Park, R. Ovalle-Robles, H. D. Yang, K. D. Kihm, R. H. Baughman, H. H. Lee, T. J. Kang and Y. H. Kim, *Nat. Commun.*, 2016, **7**, 10600.
- 19 J. Duan, G. Feng, B. Yu, J. Li, M. Chen, P. Yang, J. Feng, K. Liu and J. Zhou, *Nat. Commun.*, 2018, **9**, 5146.
- 20 T. J. Abraham, D. R. MacFarlane and J. M. Pringle, *Energy Environ. Sci.*, 2013, **6**, 2639–2645.
- 21 M. A. Lazar, D. Al-Masri, D. R. MacFarlane and J. M. Pringle, *Phys. Chem. Chem. Phys.*, 2016, **18**, 1404–1410.
- 22 S. Sahami and M. J. Weaver, *J. Electroanal. Chem.*, 1981, **122**, 171–181.
- 23 J. Hupp and M. Weaver, *Inorg. Chem*, 1984, **23**, 3639–3644.
- 24 M.-L. Seol, S.-B. Jeon, J.-W. Han and Y.-K. Choi, *Ferrofluid-based triboelectric-electromagnetic hybrid generator for sensitive and sustainable vibration energy harvesting*, 2017, vol. 31.
- 25 H. Zhou, T. Yamada and N. Kimizuka, *J. Am. Chem. Soc.*, 2016, **138**, 10502–10507.
- 26 T. Yamada, X. Zou, Y. Liang and N. Kimizuka, *Polym. J.*, 2018, 771–774.
- 27 H. Zhou, T. Yamada and N. Kimizuka, *Sustain. Energy Fuels*, 2018, **2**, 472–478.

- 28 Y. Liang, T. Yamada, H. Zhou and N. Kimizuka, *Chem. Sci.*, 2019, **10**, 773-780.
- 29 T. Shimono, M. Matsuki, T. Yamada, M. Morikawa, N. Yasuda, T. Fujigaya and N. Kimizuka, *Chem. Lett.*, 2017, **47**, 261-264.
- 30 J. E. Anderson and Y. B. Graves, *J. Electrochem. Soc.*, 1981, **128**, 294–300.
- 31 C. L. Bentley, A. M. Bond, A. F. Hollenkamp, P. J. Mahon and J. Zhang, *J. Phys. Chem. C*, 2015, **119**, 22392–22403.
- 32 G. Crini, *Chem. Rev.*, 2014, **114**, 10940–10975.
- 33 A. Harada, *Acc. Chem. Res.*, 2001, **34**, 456–464.
- 34 Y.-L. Zhao, W. R. Dichtel, A. Trabolsi, S. Saha, I. Aprahamian and J. F. Stoddart, *J. Am. Chem. Soc.*, 2008, **130**, 11294.
- 35 A. Alsaiee, B. J. Smith, L. Xiao, Y. Ling, D. E. Helbling and W. R. Dichtel, *Nature*, 2016, **529**, 190–194.
- 36 Y. Okumura and K. Ito, *Adv. Mater.*, 2001, **13**, 485–487.
- 37 A. Harada, Y. Takashima and M. Nakahata, *Acc. Chem. Res.*, 2014, **47**, 2128.
- 38 J. Zhang and P. X. Ma, *Adv. Drug Deliv. Rev.*, 2013, **65**, 1215–1233.
- 39 J. P. Diard, E. Saint-Aman and D. Serve, *J. Electroanal. Chem.*, 1985, **189**, 113–120.
- 40 K. L. Larsen, *J. Incl. Phenom.*, 2002, **43**, 1–13.
- 41 J. Of and P. Sciences, 2015, **85**, 1017–1025.
- 42 R. D. Mukhopadhyay, G. Das and A. Ajayaghosh, *Nat. Commun.*, 2018, **9**, 1–9.
- 43 J. J. Kim and P. A. Rock, *Inorganic Chem.*, 1969, **8**, 563–566.

Chapter 4 Electrochemical Thermo-Electric Conversion Using Polysulfide as Redox Species

Abstract: Thermocells convert waste heat to electricity without any pollution; however, the high cost and the corrosivity of redox species hinder their commercialization. In this work, we report the first demonstration of a thermocell that utilize abundant polysulfide as redox species. 1-Butyl-1-methylpyrrolidinium polysulfide ($P_{14}S_3$) is synthesized and the redox species are prepared by the addition of sulfur to the $P_{14}S_3$ solution in DMSO. In thermoelectric measurement, the sign of the Seebeck coefficient changes from -0.68 to $+0.5$ mV/K by the addition of sulfur in the cell. Operando UV-vis spectroscopy, as well as open circuit voltage analysis revealed that the change in the sign is attributed to the change in the dominating redox reactions by the addition of sulfur. This result also provides a thermodynamic aspect of polysulfides electrochemistry, which is of high importance in lithium-sulfur battery.

4.1. Introduction

Waste heat is released in large volumes with wide temperature distribution, and its utilization has a great potential to improve the efficiency of fossil fuel consumption. Thermo-electric conversion is a general method to convert waste heat to electricity, and that based on the semiconductor-based device has been considered as the main approach. However, in addition to the use of toxic elements,¹ the high cost and the low Seebeck coefficient (induced thermoelectric voltage per unit temperature difference, S_e) have pushed it to its limitation.¹⁻⁴ Thermocells, which are fabricated by electrodes and redox pairs inside the electrolyte, can convert heat to electricity on the basis of redox reactions. The low cost and relatively high S_e made them promising and consequently, they are attracting increased attention. The $[Fe(CN)_6]^{3-/4-}$ redox pair-composed thermocell shows a S_e of 1.4 mV/K which was taken as benchmark,⁵ and higher S_e has been attained by those with water-organic solvent mixed solvent system (S_e , 2.9 mV/K)⁶ and cobalt-based redox compounds (2.2 mV/K).^{7,8} The S_e observed for the I^-/I_3^-

thermocell is ca. 0.8 mV/K, and it is enhanced to 1.9 mV/K by introducing cyclodextrins as a result of selective host-guest interaction with I_3^- .⁹⁻¹¹ However, the use of expensive metal compounds and corrosive I^-/I_3^- species render these systems unpractical. Thus, it is of importance to find low cost and non-corrosive redox species toward the application of thermocells.

Meanwhile, due to the abundance and low cost of elemental sulfur (S_8), the lithium-sulfur battery has been emerging as a promising power storage device.¹²⁻¹⁵ Disulfide¹⁶⁻¹⁸ and S^{2-}/S_n^{2-} redox species have also been introduced into dye-sensitized solar cells (DSCs) and dot-sensitized solar cells (DSSCs)¹⁹, respectively; The thiolate/disulfide (McMT⁻/BMT) composed thermocell was proved has high thermoelectric power,²⁰ however, S^{2-}/Sn^{2-} has never been used in thermocells. We herein report the first example of thermocell which utilizes anionic polysulfide redox species in thermocells. In addition, we observed a change in the sign of S_e from negative to positive in the presence of S_8 . This is ascribed to the transformation of main redox reactions as revealed by operando UV-vis spectroscopy.

4.2. Results and discussion

4.2.1. UV-vis spectroscopy of $(P_{14})_2S_3$ with various concentration of S_8

It is known that polysulfide in solution contains inevitably various species due to their disproportionation reactions. Hence, we added various amounts of elemental sulfur (S_8) to the DMSO solution of $(P_{14})_2S_3$ and investigated the composition of existing polysulfide anions. The UV-vis spectra of the solutions are shown in Fig. 4-1a. The absorption peaks were separated by Gaussian fitting, and the change of each peak intensity are plotted in Fig. 4-1b. The S_3^{2-} ion²¹⁻²⁹ has a single peak at 617 nm while S_4^{2-} (305 and 420 nm^{24-28,30-32}), S_8^{2-} (355 nm^{29,33,34} and 500 nm^{21,22,24-26,28,30,35}) and S_6^{2-} (340 and 475 nm²⁴⁻²⁸) anions show two peaks. The UV absorption edge of DMSO at 268 nm prohibit the quantitative analysis of the absorbance peak at 270 nm, which is attributed to S_3^{2-} . The peak absorbance of S_3^{2-} increases with the increase in S_8 concentration until 20 mM, and beyond this concentration, it decreases. The ascending absorbance of S_4^{2-} (305 nm), S_6^{2-} (336 nm), and S_8^{2-} (500 nm) with the addition of S_8 suggests the transformation of S_3^{2-} to the longer polysulfides. The

spectroscopy shows that the composition of polysulfide ions can be adjusted by the added S_8 ratio.

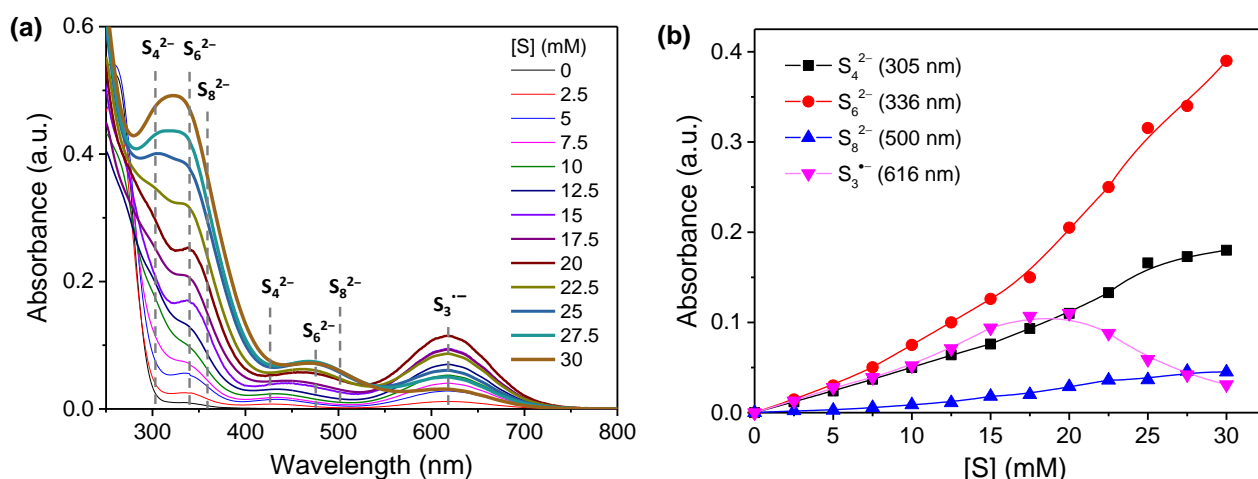


Figure 4-1. (a) UV-vis spectra of $(P_{14})_2S_3$ with various concentration of S_8 . (b) The plots of the absorbance change of polysulfide species.

4.2.2. Thermocell measurement

Thermocell measurement was executed with a home-made H-shape cell as shown in Fig. 4-2. The emerged voltage of each solution showed linear dependence to the temperature difference between both side of the cell (ΔT), which is typical of Seebeck effect and the slopes of these plots provide Seebeck coefficients (S_e). It is to note that without the addition of S_8 , the Seebeck effect was not observed. Without S_8 , S_3^{2-} is an only polysulfide species and no redox equilibrium emerges in the thermocell. As shown in Fig. 3b, the S_e value in the presence of 2.5 mM of sulfur was ca. -0.7 mV/K. The absolute S_e value decreases with the addition of sulfur until 17.5 mM, and the S_e turns to be positive when the sulfur concentration exceeded 20 mM. The S_e value became almost independent on the concentration of sulfur above this concentration. It is known that S_e value is proportional to the entropy change of the redox reaction, and the change of the S_e by the addition of S_8 would be reasonably attributed the change of polysulfide species that mainly contribute the redox equilibrium. Hence we investigated cyclic voltammetry of these solutions to identify the redox equilibrium at various S_8 concentrations.

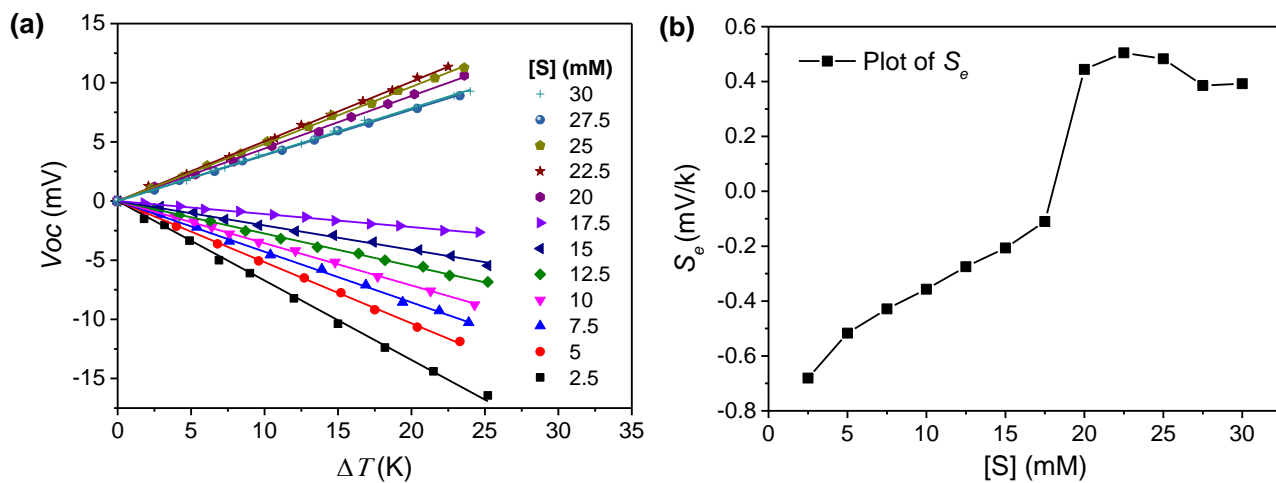


Figure 4-2. (a) The result of thermocell measurements. $[(P_{14})_2S_3] = 10$ mM in DMSO. (b) The plots of S_e with varying the concentration of sulfur. $T_c = \text{ca. } 20$ °C.

4.2.3. Cyclic voltammetry

In order to investigate the mechanism of the change of S_e , cyclic voltammetry was executed (Fig. 4-3) at various sulfur concentrations. The voltammograms have many redox peaks. With the increase of sulfur concentration up to 15 mM, the increase of the reduction peak current at -1.30 V vs Ag/AgCl was observed (Fig. 4-3a), and it decreases with the sulfur concentration above 20 mM. At higher S_8 concentrations, the emergence of reduction and re-oxidation peaks was observed at -1.43 and -1.32 V, respectively (Fig. 4-3b).

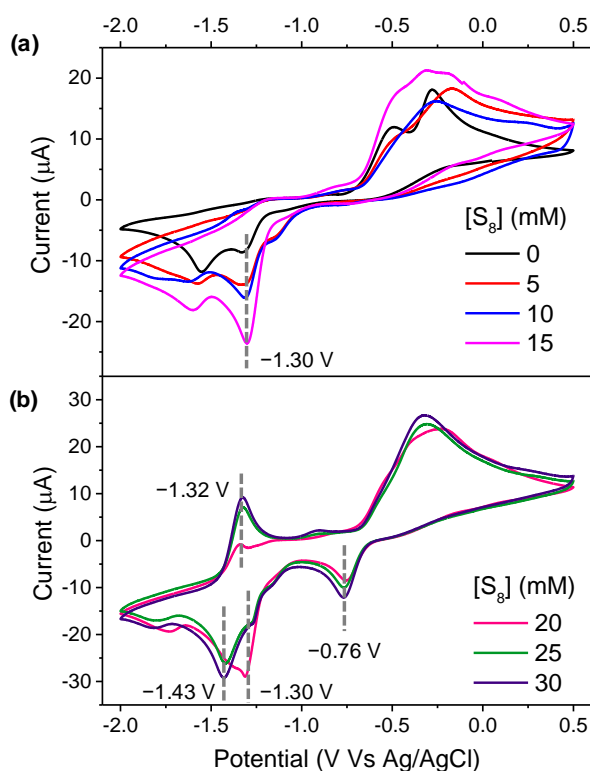


Figure 4-3. Cyclic voltammograms of 10 mM of $(P_{14})_2S_3$ and (a) 0 to 15 mM or (b) 20 to 30 mM of sulfur in DMSO. All curves were recorded at 25 °C.

These phenomena indicate the formation or increase of novel polysulfide species. We then carried out operando UV-vis spectroscopy to identify these polysulfide species.

According to the UV-vis spectroscopy during the voltage sweep at a first redaction peak from -0.5 to -0.85 V vs Ag/AgCl (Fig. 4-4b, R_1), the slight increase of peaks at 617, 500, 340 and 305 nm were observed, which are attributed to S_3^{2-} , S_8^{2-} , S_6^{2-} and S_4^{2-} , respectively.

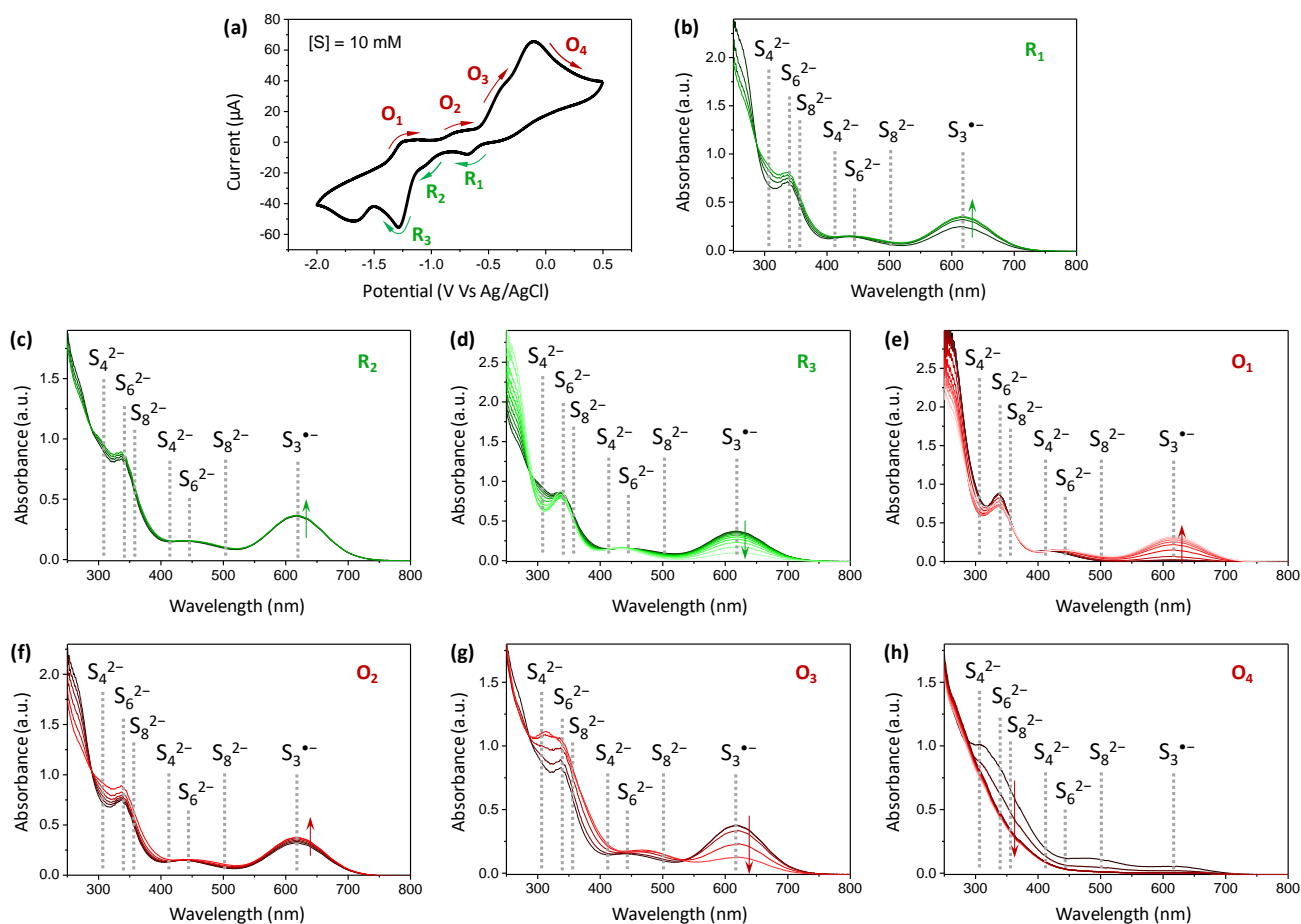
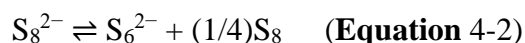


Figure 4-4. (a) A cyclic voltammogram of 10 mM of $(P_{14})_2S_3$ and 10 mM of S_8 in DMSO at a sweep rate of 1 mV/sec. (b-h) In situ UV-vis spectra of reduction reaction and oxidation sweeps between -0.5 to -0.85 V (b), -0.85 to -1.15 V (c), -1.15 to -2.0 V (d), -2.0 to -1.0 V (e), -1.0 to -0.58 V (f), -0.58 to -0.1 V (g) and -0.1 to 0.5 V (h) vs Ag/AgCl. Arrows indicate the direction of the spectral change.

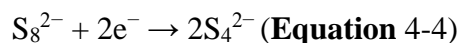
The reduction peak at -0.7 V was previously assigned to the reduction of S_8 , as shown in Eq. 4-1.^{27,31,34,36-40}



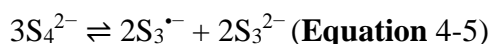
S_6^{2-} and S_3^{*-} are formed by disproportion and dissociation reactions.^{27,31,34,36-40}



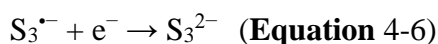
In Fig 4-4c, an increase of S_4^{2-} was observed for the R₂ peak from -0.85 to -1.15 V, and the observed change would be attributed to the following reduction reaction:



According to the report of Lu and coworkers, the decrease of S_8^{2-} is observed in this potential range.³⁶ In contrast, such a decrease in S_8^{2-} is not obvious in our experiment. This discrepancy derives from the low concentration of S_8 in our study since only 10 mM of S_8 was added into the solution, and the S_8 was consumed to the reduction of S_3^{2-} as shown in Fig. 6b. The decrease of S_8^{2-} is compensated by the increase of S_4^{2-} and probably S_6^{2-} through the disproportionation reaction as shown in Eq. 5 and the successive reaction of S_3^{*-} by Eq 4-3.



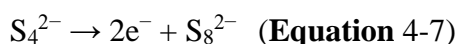
Upon scanning the electric potential from -1.15 to -2.0 V (R_3 peak), the significant decrease in the absorbance of S_3^{*-} is observed, and the increased S_3^{2-} can be detected by the decrease of the intersection of the spectra. This result suggests the following reduction reaction;



The decrease of S_4^{2-} is due to the shift of equilibrium in Eq 4-5 by decreasing the concentration of S_3^{*-} .

Another reduction peak was observed at around -1.75 V; however, the UV spectra do not show any change and the peak could be attributed to the reduction of 1-butyl-1-methylpyrrolidinium cation.

During the first oxidation wave O_1 (-2.0 V to -1.0 V), the increase of S_3^{*-} and decrease of S_3^{2-} are observed, which can be explained by the reverse oxidation reaction of R_3 . In the second oxidation wave O_2 (-1.0 V to -0.58 V), the UV peak of S_3^{*-} is almost constant while a large decrease of S_3^{2-} in addition to S_8^{2-} and S_6^{2-} were observed. The oxidation peak was previously assigned to the oxidation of S_8^{2-} to S_4^{2-} as shown in Eq. 4-7,^{36,39} however, the change of peak assigned to S_4^{2-} is small.



This discrepancy could be derived from the small oxidation peak in CV, and continuing oxidation of S_3^{2-} to S_3^{*-} and disproportionation reaction from S_3^{*-} to S_4^{2-} (Eq. 4-5) are the dominant reactions at this region.

In the O₃ (−0.58 V to −0.10 V) region in Fig 4-4g, the sharp decrease of S₃^{•−} peak along with the increase of S₄^{2−}, S₆^{2−} and S₈^{2−} peaks are observed, which are due to the electrochemical oxidation of S₃^{•−} to form high-ordered polysulfides.³⁶ O₄ region from −0.10 to 0.5 V, has the decreases of all peaks, which suggests the oxidation of polysulfide anion to S₈, which does not have absorption peak in the figures.

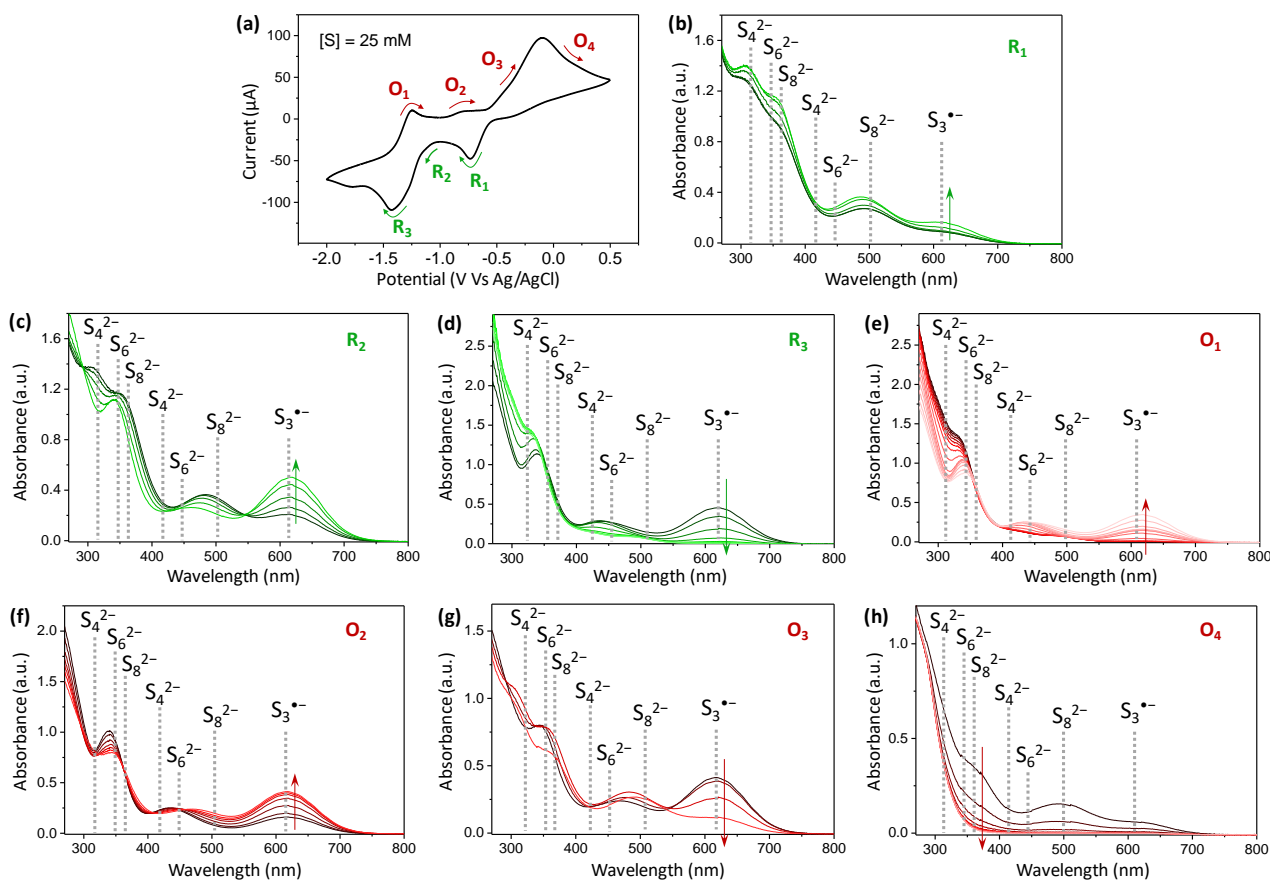


Figure 4-5. (a) Cyclic voltammogram of DMSO solution containing 10 mM (P14)₂S₃ and 25mM S₈. At a sweep rate of 1 mV/sec. (b-h) In situ UV-vis spectra of reduction and oxidation sweeps between (b) −0.5 to −1 V, (c)−1 to −1.2 V, (d) −1.2 to −2.0 V, (e) −2.0 to −1.0 V, (f) −1.0 to −0.6 V, (g) −0.6 to −0.1 V and (h) −0.1 to 0.5 V vs Ag/AgCl. Arrows indicate the direction of the spectral change.

The operand measurement was also executed with the addition of 25 mM sulfur as shown in Fig. 11. Similar to the solution with 10 mM S₈, the increase of all of the species in Fig. 4-5b can be attributed to the reduction reaction in Eq. 4-1 and successive reactions described in Eq. 4-2 and Eq. 4-3. The

reduction wave R₂ (−1.0 V to −1.2 V) was assigned to the reduction of S₈^{2−} as shown in Eq. 4-4; while the reduction current was negligible. Therefore, the change in the region can be attributed to the disproportionation reactions of S₄^{2−} to S₃^{•−} and S₃^{2−} as shown in Eq. 4-5.

As previously mentioned, the reduction wave at −1.30 V changes to one at −1.43 V with the increase of sulfur concentration from 10 mM to 25 mM. The peaks of S₃^{•−} and S₆^{2−} decrease by the reduction while that of S₃^{2−} increase by the reduction peak. Therefore, the peak at −1.43 V could be regarded as the reduction of S₆^{2−} to S₃^{2−} and shift of association equilibrium between S₃^{•−} to S₆^{2−} (Eq. 4-3).

The spectroscopic change in Fig. 4-5e for the first oxidation wave O₁ is opposite to R₃, and therefore the reaction is the oxidation of S₃^{2−} to S₆^{2−} species, which is partially dissociated to S₃^{•−}. Although the oxidation peak in O₂ region (−1.0 V to −0.6 V) is attributed to Eq. 4, the peak current is small and the main reaction is the oxidation of S₃^{2−} to S₆^{2−} and successive reaction with S₈ to form S₈^{2−} (Eq. 4-2), or dissociation reaction to S₃^{•−}. The existence of neutral S₈ species can be detected by the CV as discussed below.

The reactions in O₃ (−0.6 V to −0.1 V, Fig 4-5g), and O₄ (−0.1 V to 0.5 V, Fig. 11e) are similar to those in O₃ (oxidation of S₃^{•−} to form high-ordered polysulfides) and O₄ (oxidation of polysulfide anion to S₈) regions in Fig. 10, respectively.

As discussed above, the *S_e* changes negative to positive by the addition of sulfur. Open circuit voltage (OCV) was hence measured with various sulfur concentrations at varied temperatures, as shown in Fig. 4-6. The effect of temperature change on the OCV is negligible compared to the measurement precision. Meanwhile, with the increase of sulfur concentration from 5 to 30 mM at 20 °C, the OCV changes from −1.06 to −0.77 V vs. Ag/AgCl. In addition, an abrupt change of OCV was observed between 15 and 20 mM. The ascending of OCV from −0.96 to −0.66 V indicates the transformation of the species

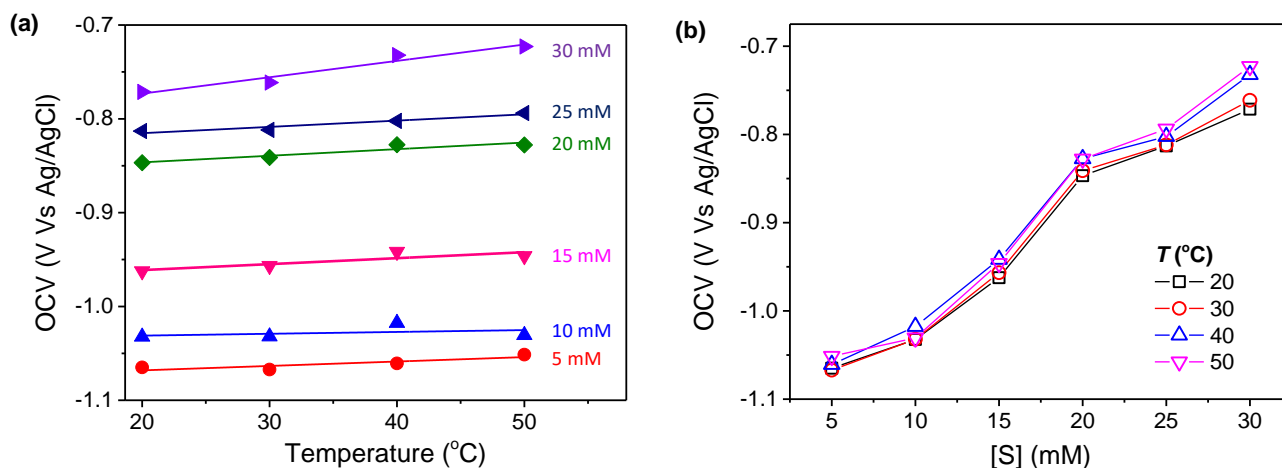


Figure 4-6. (a) Temperature dependence of the open circuit voltage (OCV) at various sulfur concentrations. The concentration of $(P_{14})_2S_3$ is 10 mM and the sulfur concentrations are written in the figure. (b) Sulfur concentration dependence of the OCV at various temperature.

from short to long polysulfides.^{41–43} Under the low sulfur concentration, OCV locates reduction side, and the main redox reactions in the thermocell should be R_3/O_1 in Fig. 4-4a ($S_3^{\cdot-} + e^- \leftrightarrow S_3^{2-}$) or R_2/O_2 ($S_8^{2-} + e^- \leftrightarrow 2S_4^{2-}$). Hence the OCV locates between these two redox reactions. The reaction at the hot and cold sides of the thermocell are driven by entropy and enthalpy, respectively, and the solvation entropy of $S_3^{\cdot-}$ in DMSO is smaller than that of S_3^{2-} . Thus the oxidation reaction occurs at the hot side, and S_e of R_3/O_1 is negative. The oxidation of S_8^{2-} to $2S_4^{2-}$ is an entropy-increasing reaction, thus the S_e should be positive. Therefore, the overall negative S_e in the thermocell with a low concentration of S_8 suggests that R_3/O_1 is the dominating reaction.

With increasing sulfur concentration, the OCV locates between R_3/O_1 ($S_6^{2-} + 2e^- \leftrightarrow 2S_3^{2-}$) and R_1/O_4 ($S_8 + 2e^- \leftrightarrow S_8^{2-}$) in Fig 4-5a. Since S_8 is a cyclic molecule and S_8^{2-} is a linear anion, and the entropy increases by the reduction reaction. Reduction reaction in R_3/O_1 is also entropy increasing. As a result, reduction reactions are preferred at the hot side, which gives positive S_e value.

4.3. Conclusion

In summary, the 1-butyl-1-methylpyrrolidinium trisulfide ($(P_{14})_2S_3$) was identified and utilized as redox species in thermocell for the first time. The polysulfide components showed changes upon the addition of S_8 , which lead to the change in the sign of S_e from negative to positive. This phenomenon was observed for the first time as well. The operando UV-vis spectroscopy and OCV measurements reveal the main redox equilibrium at various S_8 concentration. When the proportion of S_8 is low, the main redox equilibrium is that between S_3^{2-} and S_3^{-} that gives negative S_e . With a high proportion of S_8 , the main redox equilibrium changes to that S_3^{2-} and S_6^{2-} , which results in positive S_e . This study provides the first example of sulfur-based thermocell, and the detailed mechanism for the inversion of the sign of S_e is presented. The current polysulfide thermocells gives a way to fabricate thermocells inexpensively, and in addition, provides a thermodynamic points of view on the electrochemical reactions of polysulfides, which is of high importance in lithium-sulfur battery.

4.4. Experimental

4.4.1. Materials and sources

N-Methylpyrrolidine was purchased from Kanto Chemical (Japan). 1-chlorobutane was purchased from Kishida Chemical (Japan). Elemental sulfur was purchased from Sigma-Aldrich. Sodium sulfide was purchased from Wako Pure Chemical (Japan). Tetrabutylammonium hexafluorophosphate was purchased from Tokyo Chemical Industry (Japan). All solvents and reagents were used as supplied.

4.4.2. Synthesis of 1-Butyl-1-methylpyrrolidinium chloride ($P_{14}Cl$)

Because of the good solubility and low viscosity in most laboratory solvents, $P_{14}Cl$ was selected as the cation and synthesized by a modified reported method.⁴⁴ N-Methylpyrrolidine (20 mL, 0.19 mol) was dissolved in isopropanol (20 mL), then 1-chlorobutane (22 mL, 0.20 mol) was added slowly at room temperature. The reaction mixture was stirred at 85 °C for 24 hrs. After cooling to room temperature, the solvent was decanted, and the obtained pale yellow powder was purified by reprecipitation from ethyl acetate and acetonitrile for several times followed by washing with ethyl

acetate and was dried under heat and vacuum. $P_{14}Cl$ was obtained as white crystals. Yield: 27.34 g (82%). 1H NMR (400 MHz, $CDCl_3$, Fig. 4-7a): $\delta = 3.90\text{--}3.65$ (m, 4H; CH_2), 3.65–3.5 (m, 2H; CH_2), 3.26 (s, 3H; CH_3), 2.26 (s, 4H; CH_2), 1.8–1.65 (m, 2H; CH_2), 1.5–1.3 (m, 2H; CH_2), 0.95 (t, 3H; CH_3).

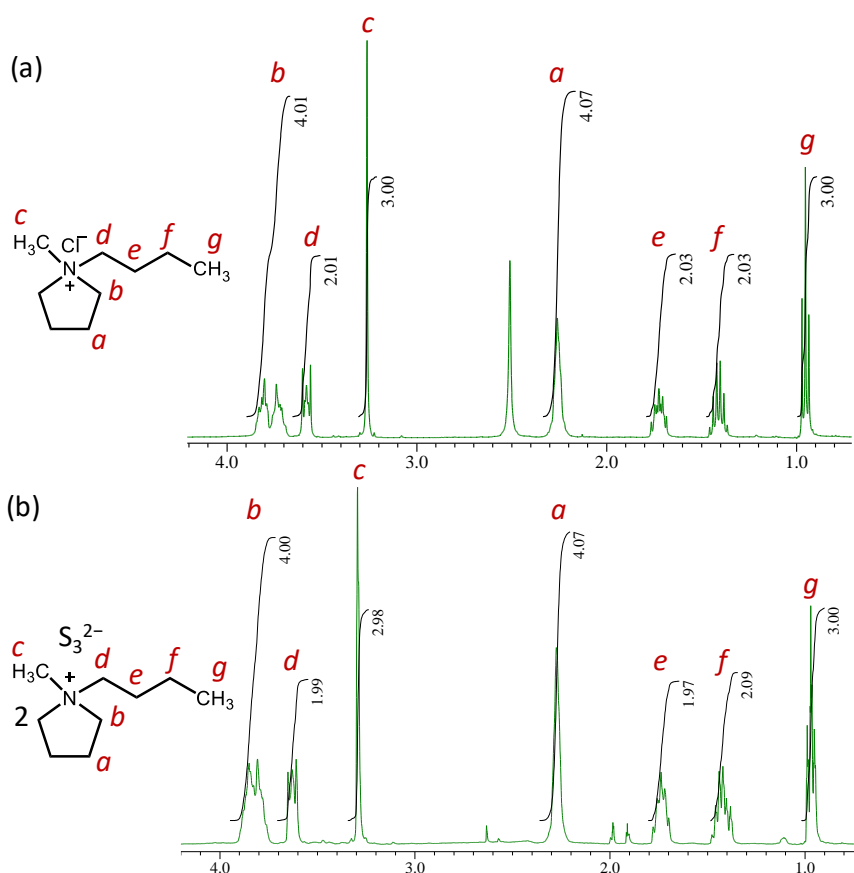


Figure 4-7. (a) 1H NMR spectra of 1-butyl-1-methylpyrrolidinium chloride, and (b) 1-butyl-1-methylpyrrolidinium sulfide.

4.4.3. Synthesis of 1-butyl-1-methylpyrrolidinium trisulfide ($(P_{14})_2S_3$)

4.36 g (24.6 mmol) of $P_{14}Cl$ and 2.12 g (27.2 mmol) of anhydrous Na_2S were dissolved in 40 ml of methanol and refluxed for 3 hrs. After cooled down to room temperature, the solvent was removed by evaporation. The solvent was further removed by heating under reduced pressure, and viscose pale

yellow solid was obtained. To this sample was added anhydrous acetonitrile, and undissolved solid was removed by membrane filtration. The solvent was eliminated by evaporation and heating of under reduced pressure and 4.22 g pale yellow solid was obtained. The ^1H NMR (400 MHz, CDCl_3 , Fig. 4-7b) spectrum of $(\text{P}_{14})_2\text{S}_3$ is similar to that of P_{14}Cl . Elemental analysis: calcd (found) % for $(\text{P}_{14})_2\text{S}_3$: C 56.79 (57.35), H 10.59 (10.46), N 7.36 (7.29). UV-vis spectra of $(\text{P}_{14})_2\text{S}_3$ in anhydrous acetonitrile contains a peak at around 270 nm, which is attributed to the S_3^{2-} anion (Fig. 4-8).^{28,36,45} It is to note that the previous report¹⁹ indicated that $\text{P}_{14}(\text{HS})$ and $(\text{P}_{14})_2\text{S}$ were obtained by a similar procedure, while the identification of these anions is unsatisfactory. Our results of elemental analysis and UV-vis spectroscopy rather indicate it is $(\text{P}_{14})_2\text{S}_3$.

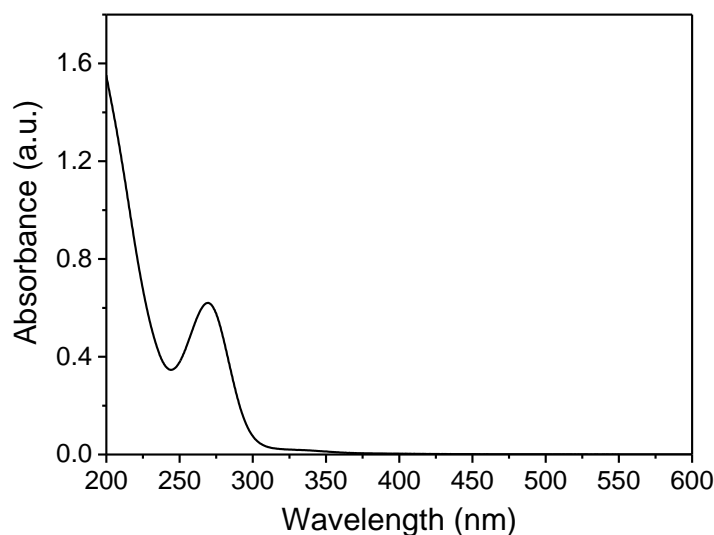


Figure 4-8. (a) UV-vis spectrum of $(\text{P}_{14})_2\text{S}_3$ (10 mM) in acetonitrile at 25 °C.

4.4.4. Seebeck Coefficient Measurements

$(\text{P}_{14})_2\text{S}_3$ (10 mM) and various amount of S_8 (0 to 30 mM) were dissolved in anhydrous and degassed DMSO under Ar atmosphere. The appearance of these solutions is shown in Fig. 4-9a. All the thermocell measurements were executed under Ar atmosphere. Seebeck coefficients of the solutions

were measured using an H-shaped glass cell as schematically shown in Fig. 4-9b. The cold side was

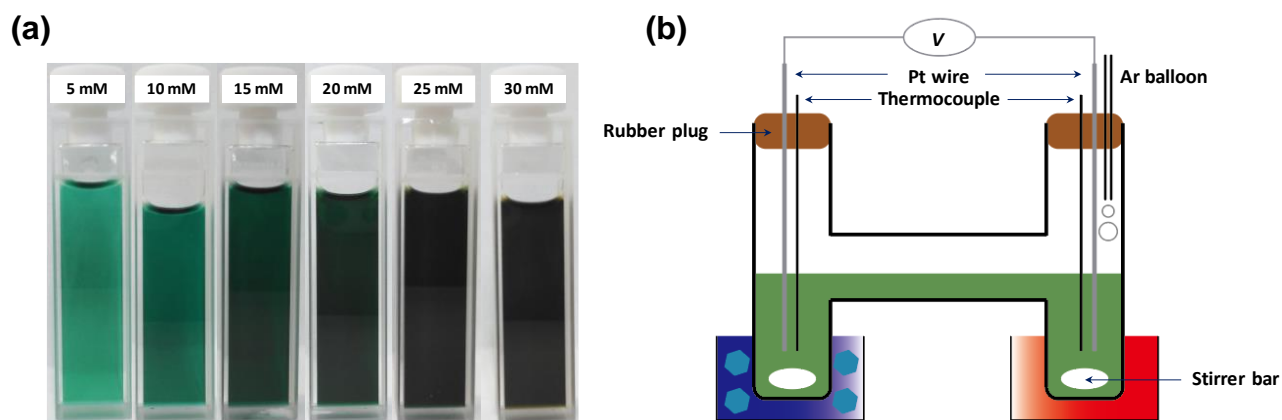


Figure 4-9. (a) Photographs of the solutions of $(P_{14})_2S_3$ (10 mM) with various concentration of S_8 in DMSO. (b) Schematic illustration of the H-shape cell used in S_e measurement. The diameter of each branch is ca. 20 mm and the distance between them is ca. 100 mm. 40 ml of solutions were added into the cell. These branches of the cell were soaked into water baths.

kept at approximately 20 °C. The temperatures were monitored with thermometers (TM201, AS ONE, Japan). The electrolyte of the cell was stirred during the measurements. Platinum wires (1 mm ϕ) were soaked into the hot and the cold branches and the potential difference between these wires was recorded by a source meter 2401 (KEITHLEY). These platinum wires were washed with concentrated sulfuric acid before use. Seebeck coefficient of each condition was estimated by the slope of $\Delta T-\Delta V$ plots.

4.4.5. Operando UV-Vis spectroscopy measurement

All measurements were executed under Ar atmosphere. The schematic illustration of the operando UV-Vis cell is shown in Fig. 4-10. A spectroelectrochemical cell with 1.0 mm path length was used. A gold mesh (BAS, Japan), a platinum wire (BAS) and Ag/AgCl electrode (RE-1B, BAS) were used

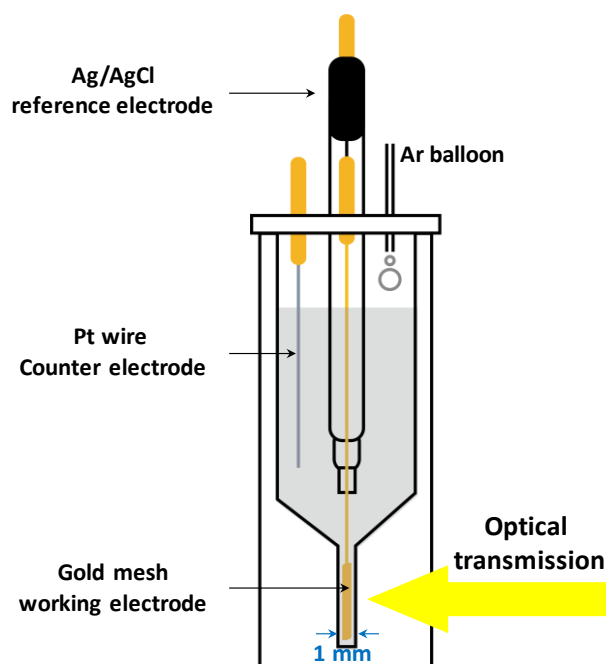


Figure 4-10. Schematic illustration of three electrode UV cell for operando measurement. An argon balloon was used to keep the inert atmosphere.

as working, counter and reference electrodes, respectively. 0.1 M tetrabutylammonium hexafluorophosphate was used as supporting electrolyte. The scanning rate of CV measurements is 1.0 mV/s. UV-vis spectra were recorded by UV-vis spectrometer (V670, JASCO) in the wavelength range between 270 to 800 nm, with a resolution of 0.5 nm and a fixed slit width of 0.5 nm. The scan speed was 1000 nm/min.

Reference

- 1 G. J. Snyder, E. S. Toberer, *Nat. Mater.* **2008**, *7*, 105–114.
- 2 K. Biswas, J. He, I. D. Blum, C.-I. Wu, T. P. Hogan, D. N. Seidman, V. P. Dravid, M. G. Kanatzidis, *Nature* **2012**, *489*, 414–418.
- 3 A. R. M. Siddique, S. Mahmud, B. Van Heyst, *Renew. Sustain. Energy Rev.* **2017**, *73*, 730–744.
- 4 L. M. Goncalves, P. Alpuim, J. H. Correia, *J. Electron. Mater.* **2010**, *39*, 1516–1521.
- 5 T. I. Quickenden; Y. Mua, *J. Electrochem. Soc.* **1995**, *142*, 3985–3994.
- 6 T. Kim, J. S. Lee, G. Lee, H. Yoon, J. Yoon, T. J. Kang, Y. H. Kim, *Nano Energy* **2017**, *31*, 160–167.
- 7 D. Al-Masri, M. Dupont, R. Yunis, D. R. MacFarlane, J. M. Pringle, *Electrochim. Acta* **2018**, *269*, 714–723.
- 8 T. J. Abraham, D. R. MacFarlane, J. M. Pringle, *Energy Environ. Sci.* **2013**, *6*, 2639–2645.
- 9 H. Zhou, T. Yamada, N. Kimizuka, *J. Am. Chem. Soc.* **2016**, *138*, 10502–10507.
- 10 Y. Liang, T. Yamada, H. Zhou, N. Kimizuka, *Chem. Sci.* **2019**, *10*, 773–780.
- 11 Y. Liang, H. Zhou, T. Yamada, N. Kimizuka, *Bull. Chem. Soc. Jpn.* **2019**, bcsj.20190062.
- 12 A. Manthiram, Y. Fu, Y. S. Su, *Acc. Chem. Res.* **2013**, *46*, 1125–1134.
- 13 M. Wild, L. O’Neill, T. Zhang, R. Purkayastha, G. Minton, M. Marinescu, G. J. Offer, *Energy Environ. Sci.* **2015**, *8*, 3477–3494.
- 14 Y. X. Yin, S. Xin, Y. G. Guo, L. J. Wan, *Angew. Chem. Int. Ed.* **2013**, *52*, 13186–13200.
- 15 S. S. Zhang, *J. Power Sources*, 2013, **231**, 153–162.
- 16 H. Tian, E. Gabrielsson, P. W. Lohse, N. Vlachopoulos, L. Kloo, A. Hagfeldt and L. Sun, *Energy Environ. Sci.*, 2012, **5**, 9752.
- 17 H. Tian, E. Gabrielsson, Z. Yu, A. Hagfeldt, L. Kloo, L. Sun, *Chem. Commun.* **2011**, *47*, 10124–10126.
- 18 H. Tian, Z. Yu, A. Hagfeldt, L. Kloo, L. Sun, *J. Am. Chem. Soc.* **2011**, *133*, 9413–9422.
- 19 V. Jovanovski, V. González-Pedro, S. Giménez, E. Azaceta, G. Cabañero, H. Grande, R. Tena-Zaera, I. Mora-Seró, J. Bisquert, *J. Am. Chem. Soc.* **2011**, *133*, 20156–20159.
- 20 V. Zinovyeva, S. Nakamae, M. Bonetti, M. Roger, *ChemElectroChem* **2014**, *1*, 426–430.
- 21 A. Kawase, S. Shirai, Y. Yamoto, R. Arakawa, T. Takata, *Phys. Chem. Chem. Phys.* **2014**, *16*, 9344–9350.
- 22 F. Gaillard, E. Levillain, *J. Electroanal. Chem.* **1995**, *398*, 77–87.
- 23 X. Yu, A. Manthiram, *Phys. Chem. Chem. Phys.* **2015**, *17*, 2127–2136.
- 24 C. Barchasz, F. Molton, C. Duboc, J. C. Leprêtre, S. Patoux, F. Alloin, *Anal. Chem.* **2012**, *84*, 3973–3980.
- 25 G. Bieker, D. Diddens, M. Kolek, O. Borodin, M. Winter, P. Bieker, K. Jalkanen, *J. Phys. Chem. C*

- 2018**, 122, 21770–21783.
- 26 N. S. A. Manan, L. Aldous, Y. Alias, P. Murray, L. J. Yellowlees, M. C. Lagunas, C. Hardacre, *J. Phys. Chem. B* **2011**, 13873–13879.
- 27 R. P. Martin, W. H. Doub, J. L. Roberts, D. T. Sawyer, *Inorg. Chem.* **1973**, 12, 1921–1925.
- 28 B. S. Kim, S. M. Park, *J. Electrochem. Soc.*, **1993**, 140, 115–122.
- 29 J. Paris, V. Plichon, *Electrochim.* **1981**, 26, 1823–1829.
- 30 D. H. Han, B. S. Kim, S. J. Choi, Y. Jung, J. Kwak, S. M. Park, *J. Electrochem. Soc.* **2004**, 151, E283–E290.
- 31 R. Bonnaterre, G. Cauquis, *J. Chem. Soc. Chem. Commun.* **1972**, 293–294.
- 32 R. D. Rauh, F. S. Shuker, J. M. Marston, S. B. Brummer, *J. Inorg. Nucl. Chem.* **1977**, 39, 1761–1766.
- 33 P. Dubois, J. P. Lelieur and G. Lepoutre, *Inorg. Chem.*, 1988, **27**, 73–80.
- 34 R. Bonnaterre, J. Badoz-Lamblin, R. Bonnaterre, G. Cauquis, M. Delamare and G. Demange, *Electrochem. Acta*, 1974, **21**, 119–131.
- 35 T. R. Anion, *Inorganic Chem.*, 1972, **11**, 1971–1973.
- 36 Q. Zou, Y. Lu, *J. Phys. Chem. Lett.* **2016**, 7, 1518–1525.
- 37 P. Leghié, J. P. Lelieur and E. Levillain, *Electrochem. commun.*, **2002**, 4, 406–411.
- 38 A. S. Baranski, W. R. Fawcett and C. M. Gilbert, *Anal. Chem.*, 1985, **57**, 166–170.
- 39 and M. H. Taitiro Fujinaga, Tooru Kuwamoto, Satoshi Okazaki, 1980, 2851–2855.
- 40 M. Cuisinier, C. Hart, M. Balasubramanian, A. Garsuch and L. F. Nazar, *Adv. Energy Mater.*, 2015, **5**, 1–6.
- 41 G. Zhou, K. Liu, Y. Fan, M. Yuan, B. Liu, W. Liu, F. Shi, Y. Liu, W. Chen, J. Lopez, D. Zhuo, J. Zhao, Y. Tsao, X. Huang, Q. Zhang and Y. Cui, *ACS Cent. Sci.*, 2018, **4**, 260–267.
- 42 M. L. Gordin, F. Dai, S. Chen, T. Xu, J. Song, D. Tang, N. Azimi, Z. Zhang and D. Wang, *ACS Appl. Mater. Interfaces*, 2014, **6**, 8006–8010.
- 43 G. Ai, Y. Dai, Y. Ye, W. Mao, Z. Wang, H. Zhao, Y. Chen, J. Zhu, Y. Fu, V. Battaglia, J. Guo, V. Srinivasan and G. Liu, *Nano Energy*, 2015, **16**, 28–37.
- 44 S. Berdzinski, J. Horst, P. Straßburg and V. Strehmel, *ChemPhysChem*, 2013, **14**, 1899–1908.
- 45 G. J. L. Bernardes, J. P. Marston, A. S. Batsanov, J. A. K. Howard and B. G. Davis, *Chem. Commun.*, 2007, 3145–3147.

Chapter 5 Conclusion and future remark

In this thesis, the enhancement of Seebeck coefficient in thermocells by the using of the host-guest interaction between cyclodextrins and triiodide, as well as the theoretical basis were described. A method to fabricate low-cost thermocell with polysulfide redox species was then introduce, and analyzed by operando UV-vis spectroscopic study.

Chapter 2 described the enhancement of Seebeck coefficient in iodide/triiodide redox couple base thermocell from 0.8 to 1.9 mV/K by Hexakis(2,3,6-tri-*O*-methyl)- α -CD ($\text{Me}_{18}\text{-}\alpha\text{-CD}$). UV-vis spectroscopic and isothermal titration calorimetric study suggest the high binding constant of $\text{Me}_{18}\text{-}\alpha\text{-CD}$ and triiodide is the key point for the high Seebeck coefficient. Besides, the formation of pentaiodide inside $\text{Me}_{18}\text{-}\alpha\text{-CD}$ was observed, and which is the first time in solution.

Chapter 3 described the basis of host-guest supermolecular science based enhancement of Seebeck coefficient. In which, the important role of enthalpy change in host-guest association was discovered and confirmed with four kinds of cyclodextrins ($\text{M}_{12}\text{-}\alpha\text{-CD}$, $\alpha\text{-CD}$, $\beta\text{-CD}$ and $\gamma\text{-CD}$). The calculated equations between Seebeck coefficient and thermodynamic parameters can be used to evaluation the thermodynamic parameters by simply thermoelectric measurements without isothermal titration calorimetry.

Chapter 4 presented a novel method for the fabrication of low-cost thermocell by the using of polysulfide species. The polysulfide redox species in the study were prepared by the addition of sulfur into 1-butyl-1-methyl-pyrolidinium trisulfide. The Cyclic voltammetry and UV-vis spectroscopy indicate that with the increase of sulfur into thermocell, the main redox reactions shift and the sign of Seebeck coefficient changes from negative to positive.

As discussed in chapter 2, S_e is determined by the concentration difference of uncaptured I_3^- at the cold and hot sides of the thermocell. The enhancement of S_e by Me₁₈- α -CD is attributed to higher binding constant between Me₁₈- α -CD and I_3^- at the cold side (low temperature) of the thermocell (Fig. 2-7b). However, the binding constant at the hot side (> 30 °C) is considerably high, which minimizes the difference in the number of uncaptured I_3^- on both sides, and limits the enhancement of S_e . If a temperature responsive host molecule having a phase transition temperature of ca. 30 °C could be introduced to the I^-/I_3^- based thermocell, the binding constant at the hot side would be significantly decreased, and less I_3^- would be captured at the hot side, leading to a larger difference in the number of uncaptured I_3^- on both sides. As a result, S_e could be further enhanced by taking the advantage of the higher concentration difference in uncaptured I_3^- . In the future, such kind of temperature responsive host molecule will be synthesized and applied to thermocells.

Acknowledgements

The study in this thesis has been carried out under the direction of Professor Nobuo Kimizuka during October 2016 – September 2019 at the Department of Chemistry and Biochemistry, Graduate School of Engineering, Kyushu University.

First and foremost, I want to express my sincere gratitude to my advisor Prof. Nobuo Kimizuka. He accepted me as a Ph.D. student in Kimizuka laboratory and continuously supported both of my study and life. I am also thankful for the excellent example he has provided as a successful scientist and professor, and I could not have imagined having a better advisor and mentor for my Ph.D. course.

I am greatly indebted to Associate Prof. Teppei Yamada for his helpful suggestion, continuous encouragement, significant discussion and the providing of the free academic environment. I appreciate all his contributions of time, ideas and patience to make my Ph.D. experience productive and stimulating.

For this dissertation I would like to thank my committee: Prof. Yoshiko Miura, and Prof. Hisashi Shimakoshi, for their insightful comments and encouragement, but also for the hard question which incited me to widen my research from various perspectives.

I would like to express my gratitude to Associate Prof. Nobuhiro Yanai and Associate Prof. Shigenori Fujikawa for their numerous valuable advice on my Ph.D. research. My sincere thanks also go to Assistant Prof. Masa-aki Morikawa for his warm help on the operation of apparatus in the laboratory and valuable suggestion on my experiments. I am also thankful for the countless warm help from Assistant Prof. Joseph Ka Ho Hui. Especially, he taught me many tips of organic synthesis, which is very important to my Ph.D. study and future work. Besides, as an ethnic Chinese, we can talk with each other in Chinese, the joy and enthusiasm he has for his research were contagious and motivational for me. I would like to thank Technical Staffs Kazumi Matsuno, Ryo Maeda, Chihoko Fukakusa, and Azusa Suematsu, for their warm encouragements and supports.

I would like to express the deep appreciation to Mr. Ryosuke Yamamoto, Mr. Yoichi Sasaki, Mr.

Yuta Kubo, Mr. Tomoya Shimono and Mr. Toshiki Eguchi for their experimental help.

I also would like to express my gratitude to Assistant Prof. Tejwant Kang (Guru Nanak Dev University), Dr. Keita Ishiba, Dr. Taku Ogawa, Dr. Masaya Matsuki, Dr. Masanori Hosoyamada, Dr. Shota Hisamitsu, Dr. Kazuma Mase, Dr. Hisanori Nagatomi. Dr. Pankaj Bharmoria, Dr. Biplab Joarder, Dr. Arijit Mallick, Mr. Tsubasa Kashino, Mr. Hironori Kouno, Mr. Kanji Shiraishi, Mr. Keisuke Kanakogi, Ms. Mariko Kozue, Mr. Shinya Uchino, Mr. Hirotaka Ohara, Ms. Hanyu Yang, Ms. Fan Gao, Ms. Xiaopeng Zou, Mr. Yuki Nagai, Ms. Nao Hirakawa, Mr. Saiya Fujiwara, Mr. Takashi Kobayashi, Mr. Tetsuro Kobayashi, Mr. Keisuke Hayashi, Mr. Yusuke Kawashima, Ms. Rena Haruki, Ms. Mika Kinoshita, Mr. Koki Nishimura, Mr. Hirotaka Inoue, Ms. Risa Iwami, Ms. Kana Orihashi, Ms. Mone Sakata, Mr. Donggyu Kwak, Ms. Mio Koharagi, Mr. Yuichiro Seki, Mr. Naoyuki Harada, Mr. Issei Maruyama, Ms. Kanae Izumi, Mr. Junpei Kondo, Mr. Ketaro Tanaka, Mr. Ryouichi Tomomatsu, Mr. Tomoyuki Hamachi, Mr. Fumitoshi Matoba, Mr. Akio Yamauchi and Ms. Naura Fakhira Antariksa.

Last but not least, I would like to thank my family: my parents and my elder sister for all their love, encouragement, and supports throughout my doctoral course.

Yimin Liang

Department of Chemistry and Biochemistry

Graduate School of Engineering, Kyushu University

September 2019